3. ATMOSPHERE

Ralf Jaiser[1], Jürgen Graeser[1], John Bilberry[3,4], Paul Ortega[3,4], Dean Greenamyer[3], Martin Radenz[15], Christopher Cox[5], Jennifer Hutchings[17], Ludovic Bariteau[5,6], Hans-Werner Jacobi[22], Julia Schmale[27], Markus Frey[29], Gina Jozef[5], John Cassano[5], Andreas Preußer[31], Ian Brooks[32]

(not on board:) Markus Rex[1,2], Marion Maturilli[1], Alexander Schulz[1], Matthew Shupe[5,6], Jessie Creamean[7], Heath Powers[3,4], Jim Mather[3,8], David Chu[3,4], Kerri Pratt[9], Gijs de Boer[5,6], Klaus Dethloff[1], Elizabeth Hunke[4], Wieslaw Maslowski[10], Allison McComiskey[11], David Randall[7], Michael Tjernstrom[12], David Turner[6], Johannes Verlinde[13], Ronny Engelmann[14], Hannes Griesche[14], Julian Hofer[14], Dietrich Althausen[14], Holger Baars[14], Patric Seifert[15], Albert Ansmann[14], Andreas Macke[14], Mario Mech[15], Bernhard Pospichal[15], Kerstin Ebell[15], Susanne Crewell[15], Gaël Dubois[16], Luc Blarel[16], Philippe Goloub[16], Ola Persson[5,6], David Costa[5,6], Ian Brooks[18], Thomas Ayers[6], Christopher Fairall[6], Michael Gallagher[5,6], Daniel Gottas[6], Jesse Leach[6], Sara Morris[6], Jackson Osborn[5,6], Sergio Pezoa[6], Taneil Uttal[6], Don Perovich[19], Timothy Stanton[20], Roberta Pirazzini[21], Byron Blomquist[5,6], Steve Archer[23], Detlev Helmig[5], Jacques Hueber[5], Laurens Ganzeveld[24], Dean Howard[5], Kevin Posman[23], Hélène Angot[5], Sjoerd Barten[24], William Sturges[25], Lucy Carpenter[26], Ivo Beck[27], Lauriane Quéléver[28], Tuija Jokinen[28], Tiia Laurila[28], Zoe Brasseur[28], Mikko Sipilä[28], Amelie Kirchgässner[29], Thomas Lachlan-Cope[29], Xin Yang[29], Alice Jones[29], Leon Clarke[30], Gijs de Boer[5,6], Dale Lawrence[5], Brian Argrow[5], Jonathan Hamilton[5], Radiance Calmer[5], Steven Borenstein[5], Abhiram Doddi[5], Michael Rhodes[5], Ryan Neely III[32], Barbara Brooks[32], Günther Heinemann[31]

[1]DE.AWI
[2]DE.UNI-Potsdam
[3]GOV.ARM
[4]GOV.LANL
[5]EDU.CU
[6]GOV.NOAA
[7]EDU.CSU
[8]GOV.SANDIA
[9]EDU.UMICH
[10]EDU.NPS
[11]GOV.BNL
[12]SE.SU
[13]EDU.PSU
[14]DE.TROPOS
[15]DE.UNI-KOELN
[16]FR.UNIV-LILLE
[17]EDU.ORSU
[18]UK.UNI-LEEDS
[19]EDU.DARTMOUTH
[20]EDU.NPS
[21]FI.FMI
[22]FR.UGA
[23]ORG.BIGELOW
[24]NL.WUR
[25]UK.AC.UEA
[26]UK.AC.YORK
[27]CH.EPFL
[28]FI.UNI-Helsinki
[29]UK.BAS
[30]UK.AC.MMU
[31]DE.UNITRIER
[32]UK.UNI-LEEDS

Grant-No. AWI_PS122_00

A comprehensive summary of the atmospheric measurements during all 5 cruise legs can be found in Shupe et al., 2022.

The atmospheric measurements during PS122/3 continued the MOSAiC atmosphere program of the two previous legs with the addition of one UAV project and several projects, which had been run by other groups previously, were now attended by specific scientists. Table 3.1 provides an overview of the leg 3 projects.

***Tab. 3.1**: List of leg 3 Team ATMOS projects*

Subchapter	Project Focus
3.1	Characterization of the atmospheric column
3.2	DOE Atmospheric Radiation Management Mobile Facility
3.3	OCEANET – Cloud and Aerosol remote sensing
3.4	Atmospheric surface fluxes and sea ice thermo-dynamics and dynamics
3.5	Trace gas flux observations
3.6	Aerosol budget and cloud interactions
3.7	Sea salt aerosol and climate impacts
3.8	Arctic atmospheric boundary layer observations with UAVs
3.9	Wind and turbulence structure in the atmospheric boundary layer

The period between 24 February and 16 May (date when leg 3 left the floe) was characterized by very cold temperatures (down to -40°C) and strong surface inversions at the beginning. In March, stormy conditions were frequent also introducing low visibility conditions from drifting and blowing snow. April and May experienced sunnier conditions and high temperatures up to > 0°C (on 19 April) introducing surface melt.

Ice conditions were dynamic throughout, with the first major lead opening on 11 March. This caused interruption of the power line to Met-City which could be re-established in early April. Further shifts of Met-City relative to *Polarstern* required cutting the power line again so that overall Met-City was operated 30 days on line power and 42 on generators. A system of a fuel barrel hocked up to either a 5 kW (yellow AWI) or 3.5 kW (red Honda) generator allowed operating Met-City without gas flux instrumentation for several days without refuelling. There were no comparable challenges with Balloon Town, except for one power line cut in April.

Despite the dynamic ice conditions and weather that partly inhibited work outside, particularly in March, the core parameters were measured to large extent. The appendix "ATMOS_CoreParameters_Leg3 02March – 24May.xls" provides a weekly summary.

For an overview of some selected measurement statistics and operational activities, please see Figures 3.1 and 3.2.

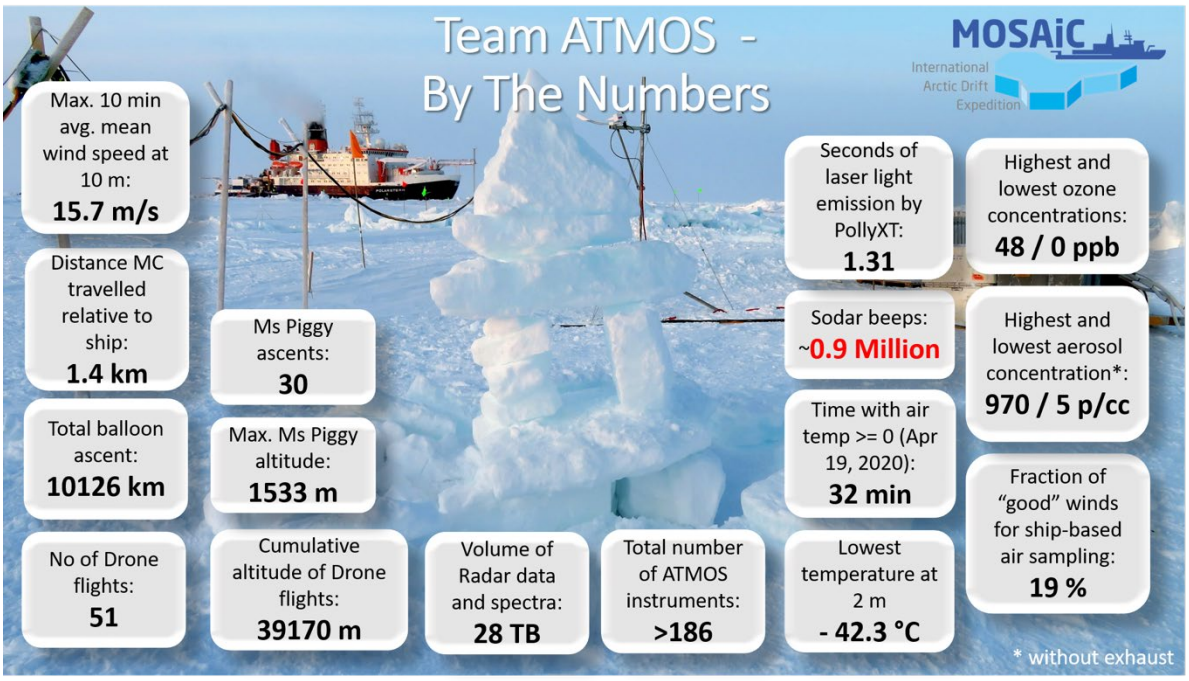

Fig. 3.1: Selected statistics from the scientific work.

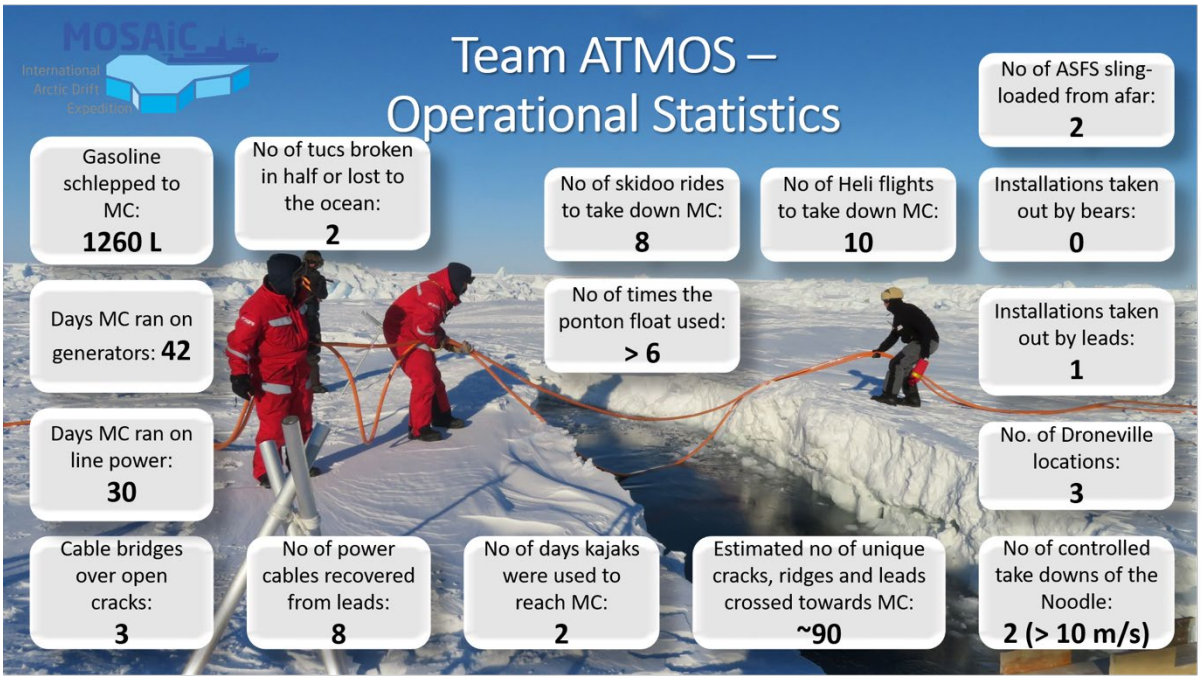

Fig. 3.2: Selected statistics from operational activities undertaken by the ATMOS team to facilitate scientific work.

References

Shupe, MD, Rex, M, Blomquist, B, Persson, POG, Schmale, J, Uttal, T, Althausen, D, Angot, H, Archer, S, Bariteau, L, Beck, I, Bilberry, J, Bucci, S, Buck, C, Boyer, M, Brasseur, Z, Brooks, IM, Calmer, R, Cassano, J, Castro, V, Chu, D, Costa, D, Cox, CJ, Creamean, J, Crewell, S, Dahlke, S, Damm, E, de Boer, G, Deckelmann, H, Dethloff, K, Dütsch, M, Ebell, K, Ehrlich, A, Ellis, J, Engelmann, R, Fong, AA, Frey, MM, Gallagher, MR, Ganzeveld, L, Gradinger, R, Graeser, J, Greenamyer, V, Griesche, H, Griffiths, S, Hamilton, J, Heinemann, G, Helmig, D, Herber, A, Heuzé, C, Hofer, J, Houchens, T, Howard, D, Inoue, J, Jacobi, H-W, Jaiser, R, Jokinen, T, Jourdan, O, Jozef, G, King, W, Kirchgaessner, A, Klingebiel, M, Krassovski, M, Krumpen, T, Lampert, A, Landing, W, Laurila, T, Lawrence, D, Lonardi, M, Loose, B, Lüpkes, C, Maahn, M, Macke, A, Maslowski, W, Marsay, C, Maturilli, M, Mech, M, Morris, S, Moser, M, Nicolaus, M, Ortega, P, Osborn, J, Pätzold, F, Perovich, DK, Petäjä, T, Pilz, C, Pirazzini, R, Posman, K, Powers, H, Pratt, KA, Preußer, A, Quéléver, L, Radenz, M, Rabe, B, Rinke, A, Sachs, T, Schulz, A, Siebert, H, Silva, T, Solomon, A, Sommerfeld, A, Spreen, G, Stephens, M, Stohl, A, Svensson, G, Uin, J, Viegas, J, Voigt, C, von der Gathen, P, Wehner, B, Welker, JM, Wendisch, M, Werner, M, Xie, ZQ, Yue, F. 2022. Overview of the MOSAiC expedition: Atmosphere. Elementa: Science of the Anthropocene 10(1). DOI: https://doi.org/10.1525/elementa.2021.00060

3.1 From the Surface to the Stratosphere: Characterization of the Atmospheric Column

Ralf Jaiser[1], Jürgen Graeser[1], [1]DE.AWI

(not on board:) Markus Rex[1,2], Marion Maturilli[1], Alexander Schulz[1] [2]DE.UNI-Potsdam

Objectives

To investigate the thermodynamic, turbulence and trace gas parameters at the ice-atmosphere interface, in the planetary boundary layer (PBL), in the free atmosphere and the lower stratosphere, several platforms like a mobile eddy covariance system and 10 m mast, a tethered and weather balloons are used.

a) Turbulent energy fluxes over sea ice and over leads

The turbulent exchange within the PBL of the atmosphere is not well understood, therefore models show a wide spread in predicting turbulent fluxes due to strong overestimation and underestimation of its magnitude. The reasons are insufficient parameterizations of the turbulent exchanges that result from a very limited amount of datasets measured during short campaigns. The SHEBA campaign (Uttal et al., 2002) that also measured over a full annual cycle in the Beaufort Sea was over 22 years ago in markedly different time and region. Especially the studies of the turbulent exchange over open leads on sea ice in the high Arctic are very rare due to a very small number of campaigns like ALEX within AIDJEX (Andreas et al., 1979), LEADEX (Ruffieux et al., 1995) and STABLE (Tetzlaff et al., 2015). However, these datasets do not cover the full spectrum of atmospheric conditions, seasons or surface characteristics. Hence, the parameterizations do not include all relevant processes or only in an insufficient way.

Due to the concept of MOSAiC, allowing observations for an entire year, it is possible to measure the turbulent exchange during a full annual cycle. We use the newest generation of *in-situ* turbulence sensors to observe nearly all relevant surface characteristics. For that purpose, mobile eddy covariance towers will be installed at the edge of open leads and close to ridges on the sea ice, in such a way that the targeted areas are directly within the footprint of the instrument. In addition, a net radiometer will measure all four radiation components over the open water during observing at open leads, contributing to the complete surface energy balance. Furthermore, pronounced changes in the surface characteristics like a change of thermal conditions (open leads, warm water) or ridges (high obstacles, strong friction) result in the development of internal boundary layers on the lee side of the targeted area. Especially for thermal internal boundary layers (over open leads) both, the height and the temporal evolution were very seldom observed so far, resulting in a small number of data points and a wide spread (see e.g. Andreas et al., 1999). Therefore, a 10 m mast with an optical fibre cable (Distributed Temperature Sensor, DTS system) measuring the air temperature every 60 cm (25 cm sampling length) and 5-10 s will be installed next to the mobile eddy covariance system for observing the temporal evolution of the thermal internal boundary layer.

b) Characterization of the planetary boundary layer over sea ice

The PBL is the lowermost atmospheric layer, connecting the surface and the free atmosphere. In the Arctic, and especially during polar night and under high pressure influence, the Arctic PBL is typically a stable and persistent feature. In the case of stable conditions, exchange with the surface is strongly inhibited, and marked temperature inversions of the order of several Kelvin are common features. In case of neutral conditions, both synoptic and radiative forcing can quickly change turbulence characteristics. The turbulent fluxes of momentum, energy and chemical compounds, as well as surface-based temperature inversions in the Arctic PBL are known to be crucial players in Arctic Warming and sea ice retreat, but are generally poorly resolved in state of the art climate models (Boé et al., 2009, Pavelsky et al., 2012, Holtslag et al. 2013,). This is in parts due to insufficient parameterizations of sub-grid scale processes (Pithan et al., 2014) that have been developed on the basis of only a few dedicated campaigns, such as, for instance, AIDJEX (Andreas et al., 1979), LEADEX (Ruffieux et al., 1995), SHEBA (Uttal et al., 2002) or STABLE (Tetzlaff et al., 2015). Other than during these campaigns, the extraordinary opportunity during MOSAiC is to measure characteristics of the Arctic PBL over sea ice during the course of a whole year, including a variety of different surface characteristics. Monitoring the thermal structure of the PBL is enabled by a state of the art *in-situ* sensor for capturing high frequency temperature fluctuations along a fibre cable (DTS), with 25 cm physical resolution and 10 seconds sampling interval. Using a tethered balloon (TB) as a carrier platform for the DTS, vertical time series of the thermodynamic structure of

the PBL will be retrieved, and the potential impact of nearby open leads (open water), ridges (high obstacles) or changing large-scale synoptic forcing will be investigated. This is the first time ever the DTS technology is combined with a TB for such investigations over the central Arctic sea ice.

A suite of additional sensors from other partners and institutes will be occasionally deployed with the TB throughout the course of the year, giving additional insights into the dynamical, thermodynamical and chemical characteristics of the PBL onsite the TB launch platform. These include, e.g. an optical particle sonde, an aerosol particle filter package, an ozone profiler, and a turbulence sensor package. The combined measurements assure the close link to other projects and foster the joint analysis of other atmospheric topics.

c) Characterization of the free troposphere and lower stratosphere

An extensive balloon program will operate from board *Polarstern*, reaching from upgraded weather balloons to sophisticated research sondes. The profiles obtained by radiosondes launched four times daily will directly support the on-site weather forecast during the expedition, while they further contribute to numerical weather forecast as observational input for data assimilation. Additional Arctic radiosondes are known to positively impact the performance of forecast systems (Yamazaki et al., 2015; Inoue et al., 2015) even in regions far from the Arctic (Sato et al., 2016; 2018). The atmospheric thermodynamic structure over sea ice was recorded by radiosondes during earlier campaigns like e.g. SHEBA (Uttal et al., 2002) or N-ICE2015 (Kayser et al., 2017) for other regions of the Arctic. Now, the atmospheric structure, moisture content, stability, Atmospheric boundary layer (ABL) height, tropopause height and other features in the vertically resolved atmospheric column will be monitored in the Central Arctic for a complete annual cycle. Events of heat and moisture transport into the Arctic by intrusions or atmospheric rivers (Woods and Caballero, 2016; Nash et al., 2018) will be identified, and their impact on the local atmospheric structure analysed. The combination with projects that focus on the observation of clouds and radiation will allow to focus on the transitions between radiatively clear and cloudy states (Stramler et al., 2011; Graham et al., 2017) and how these transitions impact the vertical stability and coupling within the atmospheric column. The radiosonde profiles retrieved during MOSAiC will be set into context with similar measurements at pan-Arctic land based stations (e.g. Ny-Alesund, Utqiagvik/Barrow, and other IASOA stations) for studies of the advective connection between the inner and outer Arctic, and the role of the Arctic dome in these exchange processes.

Weekly ozone sonde profiles will characterize the ozone distribution in the tropo- and the stratosphere throughout the year. In winter and spring, they will be part of a potential pan-Arctic ozone sonde campaign (Match) with coordinated soundings at all Arctic ozone sonde stations (e.g. von der Gathen et al., 1995; Rex et al., 1997, 2004; Manney et al., 2011). The aim is to determine the ozone loss inside the polar vortex. We expect new Arctic record ozone losses due to record low temperature regimes in single winters within the future 10 to 20 years (e.g. Rex et al., 2006).

Water vapor is a chemically, physically, and radiatively active trace gas, and its distribution in the stratosphere determines significant climatic implications. The water vapor distribution in the Arctic stratosphere bares evidence for dynamical aspects on different scales, including the large scale descending motion inside the polar vortex as well as filamentary structures at the vortex edge linked to Rossby wave activity (Maturilli et al., 2006). In the presence of very low temperatures, the sedimentation of polar stratospheric cloud (PSC) ice particles can lead to dehydration events (Maturilli and Dörnbrack, 2006; Khaykin et al., 2013). With our monthly balloon-borne cryogenic frost-point hygrometer (CFH) measurements during MOSAiC we contribute to the assessment of the water vapour distribution in the Arctic stratosphere. The dual soundings with the Compact Optical Backscatter and AerosoL Detector (COBALD) during polar night will allow to identify PSC layers related to dehydration.

Work at sea

a) On-board Polarstern: Weather Balloons

During the whole Leg 3 weather balloons were started form the Helicopter Deck on-board *Polarstern* an hour before the synoptical times 00UTC, 06UTC, 12UTC and 18UTC. This standard procedure allows that the data up to 100 hPa can be transmitted in real time to the weather forecast centres via the GTS to be incorporated in the current weather forecast. Therefore, our measurements improve the forecast of weather at our own position, which is vital in data sparse Polar Regions. Additionally, we had one TOP (Targeted Observation Periode) starting 14th of April until the 21st with seven launches daily, which had been requested by the YOPP (Year Of Polar Prediction) coordination office. This means we launched additional radiosondes for the 09UTC, 15UTC and 21UTC synoptical times, but left out the 03UTC time step for operational reasons. We probed an unusual air mass transformation event when an exceptionally warm air mass from the south reached our position. Furthermore, the frequency of sondes was increased to 8 per day when approaching the ice edge. This will be an important set of data, since it closes the gap of measurements in the marginal ice zone. Originally, this should have been covered by dropsondes during the aircraft campaign that had to be cancelled.

In the beginning of Leg 3 the stratosphere was still very cold with a very stable stratospheric polar vortex. If temperatures are too low, balloons blast too early before they reach their target pressure of 10 hPa (around 30 km altitude). Therefore, balloons were bathed in a mixture of kerosene and oil before launch to soften the material. This procedure was continued until around April 17th, when the stratosphere became warm enough to reach high altitudes without bathing the balloons.

Several storm events hit *Polarstern* during Leg 3 with very unfavourable wind directions. This led to the unfortunate fact that 10 radiosonde launches failed, although at least two launches are tried every time. Balloons popped when leaving the balloon filling hall because they hit sharp edges or they hit ship superstructures right after release with sensors failing afterwards.

Standard radiosondes are further equipped with add-on sensors on a regular basis (19 sondes in total, cf. Table 3.1.1). We performed ozone sondes on weekly basis as well as a monthly launch of a CFH (Cryogenic Frost-point Hygrometer) sensor. These instruments measure profiles of ozone concentration and stratospheric water vapour, respectively. During late winter and early spring, we further increased the frequency of ozone sondes. This effort is coordinated through the Match Campaign, where same air parcels are probed with multiple sondes at different times. These larger packages with add-on sensors can only launched under relatively calm conditions, leading to a more irregular schedule. Usually, we use larger 1500 g balloons because of the heavier weight of the setup. Nevertheless, we successfully probed the stratospheric ozone layer with standard 600 g balloons during less suitable wind conditions, where the large balloons would have been failed to launch more likely.

Tab. 3.1.1: *Weather balloon ascends with add-on sensors.*

DShip Device Operation	Synoptic Date	Add-On Sensors
PS122/3_30-12	2020-03-02 12UTC	Ozone (Match)
PS122/3_30-60	2020-03-06 18UTC	Ozone (Match)
PS122/3_31-34	2020-03-11 00UTC	Ozone (Match)
PS122/3_32-17	2020-03-17 18UTC	Ozone
PS122/3_32-31	2020-03-18 12UTC	Ozone (Match)
PS122/3_33-12	2020-03-23 18UTC	Ozone (Match)
PS122/3_33-63	2020-03-26 18UTC	Ozone (Match)
PS122/3_34-7	2020-03-30 06UTC	Ozone (Match), CFH
PS122/3_34-54	2020-04-03 18UTC	Ozone (Match)
PS122/3_34-72	2020-04-04 18UTC	Ozone (Match)
PS122/3_35-31	2020-04-07 18UTC	Ozone
PS122/3_35-85	2020-04-10 18UTC	Ozone

PS122/3_36-28	2020-04-14 12UTC	Ozone (Match)
PS122/3_36-96	2020-04-17 12UTC	Ozone
PS122/3_37-62	2020-04-23 18UTC	Ozone, CFH
PS122/3_38-71	2020-05-01 12UTC	Ozone
PS122/3_39-44	2020-05-06 18UTC	Ozone
PS122/3_40-43	2020-05-16 18UTC	Ozone, CFH
PS122/3_41-40	2020-05-22 12UTC	Ozone
PS122/3_42-41	2020-05-12 12UTC	Ozone

b) On the ice: Tethered Balloon

Tethered Balloon Operations have been performed from a dedicated launch site called Balloon Town. It was inside the central observatory close to Ocean City about 400m away from the ship. It had been set up during Leg 1 and was decommissioned at the end of Leg 3.

The Tethered Balloon with the call sign “Miss Piggy” has a size of 9m^3 and is filled with helium. It is operated by a winch and can carry about 5 kg of payload on its line. Operations can be performed for wind speeds below 7 m/s at close to the surface and below 10 m/s at the altitude of operation. We reached a record operational altitude of 1533 m at April 12th. Several instruments can be operated with the tethered balloon.

A standard tether sonde is mandatory during operation. It is needed to monitor the altitude of the balloon and to check wind speed at operational height that should not exceed 10 m/s. Furthermore, it measures humidity, which is helpful to find and avoid moist areas either of particular research interest or because of the risk of icing.

Furthermore, we operate a turbulence probe provided by TROPOS. Its sensors measure pressure, wind and temperature in high frequency allowing to estimate turbulent mixing and turbulent energy transfers in the atmosphere. Additional sensor packages were provided by BAS in terms of an aerosol particle counter (cf. Section 3.7) and aerosol sampler, and by NOAA in terms of an ozone sonde (cf. Section 3.5).

The tethered balloon was operated in two modes: We performed ascends, kept the balloon at operational altitude for some time before we brought it back to the ground (continuous measurement). This is particularly suitable for the aerosol sampler to filter enough air over time for a reasonable analysis in the laboratory. Alternatively, we performed ascends directly followed by descends (profile measurements). Here the focus lies on the vertical distribution of properties and their temporal evolution, since these profiles can be repeated consecutively.

During Leg 3 we operated the balloon on 20 days and performed 30 ascends. These are more operations than for the combined time of leg 1 and leg 2, and despite the many storms that occurred during our time on the floe. All 4 packages were deployed most of the time. A large benefit was the presence of the additional instrumentation from other groups on-board Polarstern. An aerosol layer was visible in the TROPOS Lidar on April 30th. We readily started operation to probe it. In general, the operations had to be coordinated with the helicopter team and drone flights, were no remarkable incidents happened.

At the end of Leg 3, Balloon Town had to be decommissioned, since we were leaving the floe. Initially, the plan was to remove the small tent because of the lack of a replacement as well as all valuable inventory like electronics, winches and the balloon. The following leg was supposed to return and restart operations with minimal efforts, while at the same time the risk of a major loss was supposed to be minimized. Just days before departure a major breakup of the ice floe happened and a lead appeared just some 10 meters behind Balloon Town. It was decided to remove all installations, which was performed in a one day operation on May 15.

c) On the ice: Mobile Eddy Covariance System

The Mobile Eddy Covariance System (MEC) contains several atmospheric measurement devices mounted on a sledge. It was installed during leg 2 and measures high frequency changes of wind, temperature and humidity together with slow reference measurements to estimate turbulent fluxes between 1 and 3 meters above ground depending on the setup. We upgraded the setup for measurements of net radiation during Leg 3. Thus, it is possible to gain information about the surface energy budget in a mobile setup. This is suitable for measurements downwind of leads or ridges. A complementary 10 m mast with the DTS glass fibre allows to determine the thermal structure with 10 s time and 60 cm length resolution.

At the beginning of leg 3 the system was taken over from leg 2 in Met City close to the Met Tower for comparison measurements. The experiment was successfully stopped on the 5th of March. On the 11th of March, a lead appeared close to the logistics area with favourable wind directions and the MEC was placed close to it. Operation was stopped here on March 15th since the lead closed, ridging had started and wind direction were not favourable anymore. On April 11th, a ridge experiment was performed in the logistics area. Actually, the chosen appropriate ridge was at the lead of the former lead experiment. We took measurements in distances between 2 m and 42 m from that ridge to characterize the downwind evolution of turbulent fluxes. The MEC was kept there measuring until the 14th of April. On April 15th it was moved to a position behind Balloon Town together with an ASFS station form NOAA that was placed at the L-Sites before. This setup allows an intercomparison between both instruments. Measurements stopped on May 9th and the MEC was disassembled to be brought back on board for our departure.

Issues with the software in relation to the Eddy Covariance System and the DTS glass fibre may led to corrupted data. Operational procedures were refined during our work to circumvent these issues.

Preliminary (expected) results

Data from radiosondes delivers insights into the synoptic background state of the atmosphere. This is essential for all other measurements during MOSAiC not only in the atmosphere. During Leg 3 we observed warming conditions related to the return of sunlight (Figure 3.1.1). Some further events show an anomalous warming signal, often related to high wind speeds (Figure 3.1.2) and thus storms. These events lead to strong vertical mixing. Therefore especially strong inversions and corresponding amplified cooling at the surface, is not observed. These typical features of the wintertime Arctic disappeared in the course of Leg 3. Furthermore, storms lead to advection of warm air masses from the south. In particular during the TOP between 14th of April until the 21st, we observed unprecedented warm temperatures at the surface around the melting point, but also higher layers were affected as expected for an event related to warm air advection from the south. Such warm temperatures did not reoccur until mid of May. Based on this data, we expect the beginning of summer season at the end of our leg.

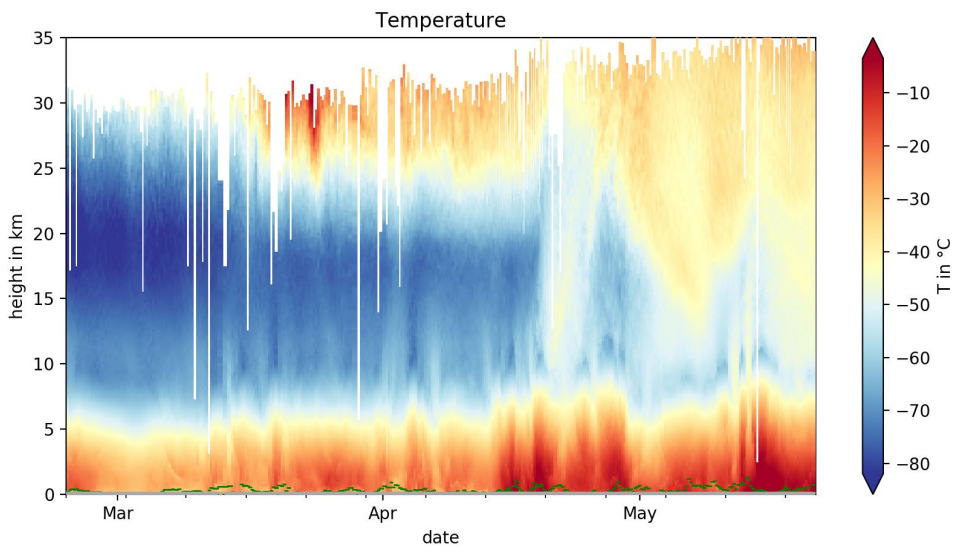

Fig. 3.1.1: *Temperature in °C from radiosonde data during leg 3. Green line estimates boundary layer height from Richardson Number.*

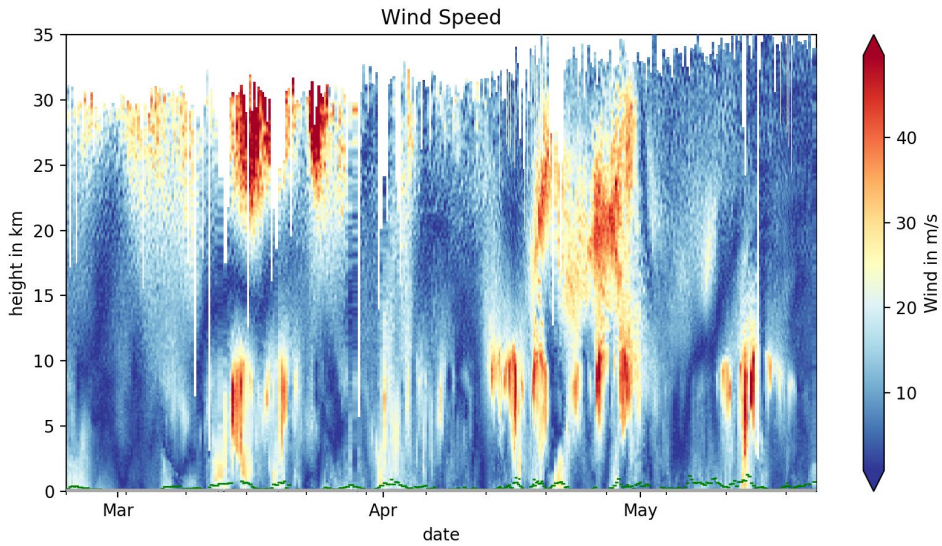

Fig. 3.1.2: *Wind speed in m/s from radiosonde data during leg 3. Green line estimates boundary layer height from Richardson Number.*

Tropospheric wind speeds have been higher than in previous MOSAiC legs, which is related to several storms that hit the floe (16 days with wind speeds above 34 kt, DWD). Green lines in Figure 3.1.1 and 3.1.2 indicate the height of the boundary layer estimated on the Richardson Number. An increase in boundary layer heights also indicates an increased mixing, which is mostly related to the many storms, but also to the warming air column.

In the stratosphere, we observed a very stable stratospheric polar vortex in the lower stratosphere. This is not obvious from the wind data in Figure 3.1.2, since our position was mostly inside the vortex, where wind speeds are low. The final warming did not happen until mid of April. After the breakdown of the vortex, we see some signals of interaction between Stratosphere and Troposphere in terms of wind and temperature anomalies in 10 to 20 km altitudes. But in general, the stratosphere became warm in May, which is also a sign of the beginning of the summer season.

The stability of the stratospheric polar vortex is of further interest regarding the stratospheric ozone concentration. In a stable vortex, cold temperatures prevail into the sunlit season. Under cold and sunlit conditions, heterogeneous chemistry can lead to the activation of halocarbons that lead to ozone depletion. Corresponding condition have been observed until mid of April (Figure 3.1.1). Our ozone observations (Figure 3.1.3) clearly show the reduction of stratospheric ozone starting around mid of March, when large fractions of the polar vortex become sunlit. A minimum in ozone concentration is visible around 18 km and values of total ozone column fall below 200 DU. Ozone concentrations become closer to normal values with more than 250 DU in mid of April, when the polar vortex broke down with a warming stratosphere and increased ozone transports from lower latitudes.

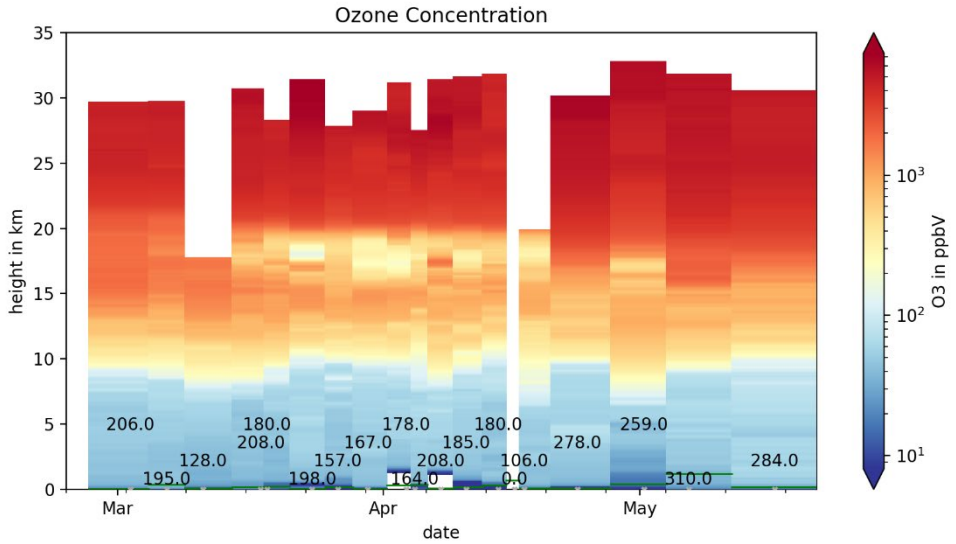

Fig. 3.1.3: *Ozone concentration in ppbV from ozone sonde data during leg 3. Numbers indicate estimated Dobson Units from that data. Green line estimates boundary layer height from Richardson Number.*

From the ozone sonde data, we further observe strong ozone depletion at the surface, which is also related to heterogeneous chemistry. Ice surface, cold conditions, a stable boundary layer and the presence of halogenated compounds then lead to ozone depletion events. Very low ozone values close to the surface are displayed in Figure 3.1.3 in particular between the beginning and mid of April. White shadings indicated that absolutely no ozone was measured by the sonde. Further details regarding this topic are discussed in section 3.5 as well.

Data from the eddy covariance system, DTS glass fibre and our tethered balloon payloads need further processing to be meaningful. First results on the ozone sonde on the tethered balloon are discussed in section 3.5. Nevertheless, the operations were very successful during this MOSAiC leg with more tethered balloon ascends than in all legs before combined.

Data management

All data are handled, documented, archived and published following the MOSAiC data policy (see APPENDIX). All radiosonde data have been transmitted to the GTS in near real-time to assure their availability for numerical weather forecast. All sounding data (radiosonde, ozone sonde, CFH, COBALD) and according auxiliary measurements are stored in the MCS. Upon the end of leg 2, the preliminary sounding data will be processed at the GRUAN Lead Centre in Lindenberg, Germany. The final sounding data will be stored at the PANGAEA data repository (World Data Center PANGAEA Data Publisher for Earth & Environmental Science; http://www.pangaea.de/).

The DTS light backscatter profiles (incl. preliminary temperature profiles) were also stored in the MCS after each measurement period. The final data processing of the DTS temperature profiles will be conducted at the Alfred Wegener Institute in Potsdam, Germany (contact: Alexander Schulz, alexander.schulz@awi.de). Final data products will be stored at the PANGAEA data repository (World Data Center PANGAEA Data Publisher for Earth & Environmental Science (www.pangaea.de)).

References

Andreas EL, Paulson CA, William RM, Lindsay RW, Businger JA. 1979. The turbulent heat flux from arctic leads. Boundary-Layer Meteorol. 17, 57–91

Boé J, Hall A, Qu X (2009) Current GCMs' Unrealistic Negative Feedback in the Arctic. Journal of Climate, 22, 4682-4695

Graham R, Rinke A, Cohen L, Hudson SR, Walden VP, Granskog MA, Dorn W, Kayser M, and Maturilli M (2017) A comparison of the two Arctic atmospheric winter states observed during N-ICE2015 and SHEBA, J. Geophys. Res. Atmos., 122, 5716–5737

Holtslag AAM, Svensson G, Baas P, Basu S, Beare B, Beljaars ACM, Bosveld FC, Cuxart J, Lindvall J, Steeneveld GJ, Tjernström M, Van De Wiel BJH (2013) Stable Atmospheric Boundary Layers and Diurnal Cycles: Challenges for Weather and Climate Models. BAMS, 1691-1706

Inoue J, Yamazaki A, Ono J, Dethloff K, Maturilli M, Neuber R, Edwards P, and Yamaguchi H (2015) Additional Arctic observations improve weather and sea-ice forecasts for the Northern Sea Route, Science Reports, 5, 16868

Kayser M, Maturilli M, Graham RM, Hudson SR, Rinke A, Cohen L, Kim J-H, Park S-J, Moon W, Granskog, M (2017). Vertical thermodynamic structure of the troposphere during the Norwegian young sea ICE expedition (N-ICE2015). Journal of Geophysical Research: Atmospheres 122.20, 10855–10872.

Khaykin SM, Engel I, Vömel H, Formanyuk IM, Kivi R, Korshunov LI, Krämer M, Lykov AD, Meier S, Naebert T, Pitts MC, Santee ML, Spelten N, Wienhold FG, Yushkov VA, and Peter T (2013), Arctic stratospheric dehydration – Part 1: Unprecedented observation of vertical redistribution of water, Atmos. Chem. Phys., 13, 11503-11517

Maturilli M, and Dörnbrack A (2006) Polar stratospheric ice cloud above Spitsbergen, J. Geophys. Res., 111, D18210

Maturilli M, Fierli F, Yushkov V, Lukyanov A, Khaykin S, and Hauchecorne A (2006) Stratospheric Water vapour in the vicinity of the Arctic polar vortex. Annales Geophysicae, 24, 1511-1521

Manney GL, Santee ML, Rex M, Livesey NJ, Pitts MC, Veefkind P, Nash ER, Wohltmann I, Lehmann R, Froidevaux L, Poole LR, Schoeberl MR, Haffner DP, Davies J, Dorokhov V, Gernandt H, Johnson B, Kivi R, Kyrö E, Larsen N, Levelt PF, Makshtas A, McElroy CT, Nakajima H, Parrondo MC, Tarasick DW, von der Gathen P, Walker KA, and Zinoviev NS (2011) Unprecedented Arctic ozone loss in 2011, Nature, 478 (7370), pp. 469-475

Nash D, Waliser D, Guan B, Ye H, and Ralph F (2018) The role of atmospheric rivers in extratropical and polar hydroclimate, J. Geophys. Res. Atmos., 123, 6804–6821

Pavelsky TM, Boé J, Hall A, Fetzer, EJ (2011) Atmospheric inversion strength over polar oceans in winter regulated by sea ice. Climate Dynamics, 36, 945-955

Pithan F, Medeiros B, Mauritsen T (2014) Mixed-phase clouds cause climate model biases in Arctic wintertime temperature inversions. Climate Dynamics, 43, 289-303

Rex M, Harris NRP, von der Gathen P, Lehmann R, Braathen GO, Reimer E, Beck A, Chipperfield MR, Alfier R, Allaart M, O'Connor F, Dier H, Dorokhov V, Fast H, Gil M, Kyrö E, Litynska Z, Mikkelsen IS, Molyneux MG, Nakane H, Notholt J, Rummukainen M, Viatte P, and Wenger J (1997) Prolonged stratospheric ozone loss in the 1995/96 Arctic winter, Nature, 389 , pp. 835-838

Rex M, Salawitch RJ, von der Gathen P, Harris NRP, Chipperfield M, and Naujokat B (2004) Arctic ozone loss and climate change, Geophys. Res. Lett., 31, L04116

Rex, M, Salawitch RJ, Deckelmann H, von der Gathen P, Harris NRP, Chipperfield MP, Naujokat B, Reimer E, Allaart M, Andersen SB, Bevilacqua R, Braathen GO, Claude H, Davies J, De Backer H, Dier H, Dorokov V, Fast H, Gerding M, Hoppel K, Johnson B, Kyrö E, Litynska Z, Moore D, Nagai T, Parrondo MC, Risley D, Skrivankova P, Stübi R, Trepte C, Viatte P, and Zerefos C (2006) Arctic winter 2005: Implications for stratospheric ozone loss and climate change , Geophysical Research Letters, 33, L23808

Ruffieux D, Persson, POG, Fairall CW, Wolfe DE. 1995. Ice pack and lead surface energy budgets during LEADEX 1992. J. Geophys. Res. 100, 4593–4612

Sato K, Inoue J, Yamazaki A, Kim J-H, Maturilli M, Dethloff K, Hudson SR, and Granskog MA (2016) Improved forecasts of winter weather extremes over midlatitudes with extra Arctic observations, J. Geophys. Res. Oceans, 121

Sato K, Inoue J, Yamazaki A, Kim J-H, Makshtas A, Kustov V, Maturilli M, and Dethloff K (2018) Impact on predictability of tropical and mid-latitude cyclones by extra Arctic observations, Science Reports, 8, 12104

Stramler K, Genio ADD, and Rossow WB (2011) Synoptically driven Arctic winter states, Journal of Climate, 24(6), 1747–1762

Tetzlaff A, Lüpkes C, and Hartmann J (2015) Aircraft-based observations of atmospheric boundary-layer modification over Arctic leads, Quarterly Journal of the Royal Meteorological Society

Uttal, T, and Coauthors (2002): Surface heat budget of the Arctic Ocean. Bull. Amer. Meteor. Soc., 83, 255–275

von der Gathen P, Rex M, Harris NRP, Lucic D, Knudsen BM, Braathen GO, Backer HD, Fabian R, Fast H, Gil M, Kyrö E, Mikkelsen IS, Rummukainen M, Stähelin J, and Varotsos C (1995) Observational evidence for chemical ozone depletion over the Arctic in winter 1991-92, Nature, 375, pp. 131-134

Woods C, and Caballero R (2016) The role of moist intrusions in winter Arctic warming and sea ice decline, Journal of Climate, 29(12), 4473–4485

Yamazaki A, Inoue J, Dethloff K, Maturilli M, and König-Langlo G (2015) Impact of radiosonde observations on forecasting summertime Arctic cyclone formation, J. Geophys. Res. Atmos., 12

3.2 DOE Atmospheric Radiation Measurement Program's Mobile Facility

John Bilberry[3,4], Paul Ortega[3,4], Dean Greenamyer[3]

(not on board:) Matthew Shupe[1,2], Jessie Creamean[6], Heath Powers[3,4], Jim Mather[3,5], David Chu[3,4], Kerri Pratt[7], Gijs de Boer[1,2], Klaus Dethloff[8], Elizabeth Hunke[4], Wieslaw Maslowski[9], Allison McComiskey[10], David Randall[6], Michael Tjernstrom[12], David Turner[2], Johannes Verlinde[12]

[1]EDU.CU
[2]GOV.NOAA
[3]GOV.ARM
[4]GOV.LANL
[5]GOV.SANDIA
[6]EDU.CSU
[7]EDU.UMICH
[8]DE.AWI

[9]EDU.NPS
[10]GOV.BNL
[11]SE.SU
[12]EDU.PSU

Objectives

To understand the changing Arctic sea ice at a fundamental level requires a detailed accounting of energy flow through the sea ice system. While it is clear that atmospheric energy fluxes are critically important for the sea ice energy budget, many processes controlling these fluxes, and their interactions, are poorly understood and represented in numerical models. This project aims to observe specific processes that control the flow of energy through the Arctic atmospheric system and thereby to address pressing science questions under four broad topics.

(a) Surface Energy Budget: What is the annual evolution of the surface energy budget over young sea ice? What are the key process interactions determining the surface energy budget and specifically variability in surface radiation?

(b) Clouds and Precipitation: What factors determine Arctic cloud phase partitioning? What role do clouds and precipitation play in determining low-level atmospheric structure? How does surface inhomogeneity influence the spatial structure of cloud-precipitation systems?

(c) Aerosols: How do aerosol physical, chemical, and optical properties over sea ice vary seasonally? What sources and transport patterns are responsible for variability in Arctic aerosol? What are the radiative and cloud-nucleating properties of Arctic aerosol?

(d) Boundary Layer Structure: What are the properties and effects of stably stratified turbulence in the Arctic boundary layer? What are the effects of a thinned ice cover on boundary layer stability and heat fluxes? How do surface- and cloud-driven dynamics impact the boundary layer structure?

Work at sea

To provide the diverse and detailed atmospheric measurements needed to address the primary scientific objectives of the project, the US Department of Energy's Atmospheric Radiation Measurement (ARM) Program (www.arm.gov) has deployed its second ARM Mobile Facility (AMF-2) onboard and nearby *Polarstern* during MOSAiC. This extensive suite of instruments is operated in a collection of six laboratory sea-containers installed on the bow of *Polarstern*, one laboratory container installed on the *Polarstern* P-deck, as well as various instruments installed at Met City out on the sea ice of the Central Observatory. ARM has also provided funding support for one half of the meteorological radiosonde program led by AWI during MOSAiC, as well as personnel support for launching some of these soundings. The AMF-2 facility can be described via five instrument collections, which are captured in Table 3.2.1.

***Tab. 3.2.1**. All instruments installed and operated by the DOE ARM program, including the measurement objectives, installation location, and start date for observations.*

Instrument	Measurement Objectives	Installation Location	Start of Observations
Meteorology and Winds			
Radiosonde Program (support for ½ of equipment)	Profiles of temperature and humidity	Helideck	20 Sept
Present Weather Detector (PWD)	Visibility	(1) P-deck port side; (2) Met City	17 Oct

Beam-steerable radar wind profiler (BSRWP)	Wind profiles	KAZR lab (C3)	5 Oct
Doppler lidar (DL)	Wind profiles, turbulence	Top OPS lab (C4)	7 Oct
Cloud Properties and Processes			
2-channel microwave radiometer (MWR2C)	Liquid water path and precipitable water vapor	Lower P-deck port side	16 Oct
3-channel microwave radiometer (MWR3C)	Liquid water path and precipitable water vapor	Lower P-deck port side	8 Oct
Ka-Band ARM Zenith Radar (KAZR)	Cloud occurrence and properties	KAZR lab (C3)	5 Oct
Marine W-Band ARM Cloud Radar (MWACR)	Cloud occurrence and properties	Top of OPS lab (C4)	16 Oct
High Spectral Resolution Lidar (HSRL)	Cloud & aerosol properties	OPS lab (C4)	10 Oct
Micropulse Lidar (MPL)	Cloud & aerosol properties	OPS lab (C4)	5 Oct
Ceilometer (CEIL)	Cloud base height	Lower P-deck port side	8 Oct
Total Sky Imager (TSI)	Hemispheric sky views	P-deck	23 Mar
Precipitation			
Ka-Band Scanning ARM Cloud Radar (Ka-SACR)	Cloud and precipitation spatial distribution	P-deck, starboard side	5 Oct
Parsivel2 Laser Disdrometer (LDIS)	Fall velocity and precipitation rate of precipitation	(1)P-deck port side; (2)Met City double Altar shield	(1) 30 Oct, (2) 14 Nov
Pluvio2 Weighing Bucket Rain Gauge (WBRG)	Precipitation mass	Met City in double Altar shield	30 Oct
Siphon Rain Gauge (SRG)	Precipitation mass	P-deck port side	30 Oct
Radiation			
Marine Atmospheric Emitted Radiance Interferometer (MAERI)	Spectral infrared radiation, both downwelling and upwelling	Lower P-deck port side, view to port side ice	9 Oct
Cimel Sunphotometer (CSPHOT)	Atmospheric transmission & scattering during daylight	P-deck	Not yet installed
Fast Rotating Shadowband Radiometer (FRSR)	Direct and diffuse components of downward solar flux	P-deck	14 Oct
Ground Radiometer System (GNDRAD) – PIR, PSP	Upwelling shortwave and longwave radiation	Met City “swingset”	14 Oct
Ground Infrared Thermometer (IRT)	Ground temperature with wide field-of-view	Met City “swingset”	30 Oct
Multifilter Radiometer 3-meter (MRF3M)	Reflected radiative flux in narrow bands	Met City “swingset”	14 Oct
Ice Radiometer System (ICERAD) – PIR, PSP, SPN1	Downwelling shortwave and longwave radiation,	Met City	14 Oct

	with shortwave direct and diffuse		
Shipboard Radiometer System (SHIPRAD) – PIR, PSP, SPN1	Downwelling shortwave and longwave radiation, with shortwave direct and diffuse	(1) P-deck port side; (2) P-deck starboard side	(1) 7 Oct; (2) 7 Oct
Sky Infrared Thermometer (IRT)	Sky temperature with narrow field-of-view	Met City "swingset"	14 Oct
Aerosols and Gases			
Automated Weather Station (AOSMET)	Pressure, temperature, relative humidity, winds	AOS inlet on AOS lab (C5)	9 Oct
Trace Gas Monitors	Concentrations: carbon monoxide, nitrous oxide, water vapor	AOS lab (C5)	9 Oct
Ozone Monitor	Concentration of ozone	AOS lab (C5)	9 Oct
Aerosol Chemical Speciation Monitor (ACSM)	Bulk chemical composition	AOS lab (C5)	8 Nov
Condensation Particle Counter (CPC)	Total particle concentration for sizes >10nm	AOS lab (C5)	8 Oct
Ultrafine Condensation Particle Counter (UCPC)	Total particle concentration for sizes >3nm	AOS lab (C5)	8 Oct
Cloud Condensation Nuclei Counter (CCN)	Concentration of cloud condensation nuclei	AOS lab (C5)	8 Nov
Scanning Mobility Particle Sizer (SMPS)	Aerosol size distribution	AOS lab (C5)	9 Oct
Ultra-High Sensitivity Aerosol Spectrometer (UHSAS)	Aerosol size distribution	AOS lab (C5)	7 Oct
Humidified Tandem Differential Mobility Analyzer (HTDMA)	Aerosol size distribution exposed to different moisture levels	AOS lab (C5)	28 Sept
Single Particle Soot Photometer (SP2)	Soot mass of aerosol particles	AOS lab (C5)	15 Oct
Particle Soot Absorption Photometer (PSAP)	Bulk aerosol absorption	AOS lab (C5)	8 Oct
Nephelometer (NEPH)	Total aerosol scattering at 450, 550, and 700 nm wavelengths	AOS lab (C5)	8 Oct

In addition to the core AMF-2 instruments, ARM has agreed via a proposal process to host and operate instrumentation for two collaborating scientists, Drs. Jessie Creamean and Kerri Pratt. These guest instruments complement the core ARM measurements by the addition of ice nucleus filters, drum samplers, and impactors, all sampling off of the Aerosol Observing System's inlet.

The ARM facility was supported on MOSAiC Leg 3 by 3 on-site technicians (Bilberry, Ortega, Greenamyer). The Total Sky Imager (TSI) was installed on the P-deck in mid-March after the transition from Polar night to Polar day.

Operations during Leg 3 were generally robust, with the following issues.

- The X-band Scanning ARM Cloud Radar (X-SACR) system never operated robustly in spite of many attempts to replace, fix, or modify different components; thus, the only scanning radar system available is the Ka-band component of the SACR.
- The AOS system samples air through an inlet and has a special design to minimize sampling of ship's exhaust; this includes monitoring parameters like carbon monoxide to trigger a back flow through the stack during periods of pollution. Thus, for certain periods, typically determined by wind direction, aerosol sampling was not possible.
- The Humidified Tandem Differential Mobility Analyzer (HTDMA) had a problem with the drain system during Leg2, waiting spares will come for Leg4.
- The 3-channel microwave radiometer (MWR3C) had a problem with the elevation motor for most of leg 3. The elevation motor failed permanently and the MWR3C was taken out of service in late April.
- The Parsivel2 Laser Disdrometer (LDIS) at Met City was uninstalled after a large lead opened up right next to it on March 11. The instrument itself was rescued and taken back to the ship. A few days later, an ice ridging event consumed the Alter shield and control box for the LDIS. Spares are expected to arrive on leg 4 in order to redeploy the LDIS once Met City is re-established.
- Met City was run on generator power for much of leg 3. Due to ice dynamics and ice movement, it was impossible to maintain a power line from the ship to Met city. Additionally, the data connection to Met City was uninstalled on March 11 due to a lead opening up. Data was collected manually on a regular basis for the remainder of leg 3.
- During the March and April period. ARM's equipment at Met City had temporary outages occasionally as all equipment at Met City was operated on generators during this period when the power line from the ship was disconnected.
- Due to the departure of the Polarstern from the ice floe, ARM instrumentation at Met city was taken down and packed away on May 8, 2020. The Met city instrument set will have to be reinstalled once a new Met City is re-established during leg 4.
- Due to the departure of the Polarstern from the ice floe, the ARM data system was partially shut down for the voyage on May 14. The data system will resume operation during leg 4 once a new drift position has been established. As a result of the data system shutdown, only a partial set of instruments will be run during the transit period. Instruments left running on the ship during the transit period continue to record data independently of the data system.
- The Marine Atmospheric Emitted Radiance Interferometer (MAERI) had troubles during the March storm period. Snow had found its way into one of the blackbodies used for calibration. The MAERI was out of service for a couple of weeks in April, in order to clean and dry the black bodies. Snow was likely able to get inside the MAERI due to the failure of the rain sensor functionality in the extreme low temperatures and high winds of March.
- Due to software issues the Fast Rotating Shadow band Radiometer (FRSR) was not operational for the entire leg 3. It is unclear whether this will be corrected on leg 4 or not.
- The Sea State Camera, which is used for the purposes of data validation for the MAERI was taken out of service near the end of April due to a part failure. A replacement part is expected to arrive on leg 4.
- Other short-term issues with ARM instrumentation include temporary interruptions to operations of the MWR2C, MAERI, BSRWP, CO_N2O, MWACR, KAZR, ACSM, HSRL. Otherwise, all systems operated rather robustly for the duration of Leg 3.

- From April 27 to April 28, all of Met City was turned off for the purposes of a clean air day for aerosol measurements that had been proposed. Met City was down for about 18 hours.

Preliminary (expected) results

Primary results from the AMF-2 deployment at MOSAiC will be an extensive collection of high-quality data sets from the AMF-2 instrumentation that are as continuous as possible for the full year. These data sets will be quality assured by a large team of instrument mentors and facility managers that will not participate in the field at MOSAiC. Based on these data sets, a suite of value-added products will also be derived to provide information on geophysical parameters related to the atmospheric state, clouds, aerosols, vertical atmospheric structure, and others. These data sets are intended to support a great deal of process-based research in support of advancing knowledge, assessing models, and developing improved models for representing climate processes.

Data management

All data produced by the ARM Program during MOSAiC Leg 3 has been automatically ingested and stored on ARM's onboard "site data system," which performs many operational tasks involved with data management, initial data ingesting and formatting, data quality checks, and the production of quicklook plots of the data. Quicklooks are available via a web page to other scientists onboard Polarstern (https://192.168.3.33:8443) and to the general public (https://dq-amfc2.amf.arm.gov). With nearly 36 TB of data produced during Leg 3, it has been agreed that this data will not initially be uploaded to the MOSAiC Central Server, however, MOSAiC scientists can get access to the raw data through a free account on ARM's site data system (192.168.3.33:22) by obtaining credentials from the ARM data manager (see ARM technicians onsite). After MOSAiC Leg 1, and all subsequent legs, the full set of collected data are physically transported to the ARM data management facility and promptly ingested into a full set of processed data files that will then be publicly available via the ARM Data Archive (www.archive.arm.gov). Raw data will be available within a couple of weeks of its arrival at the data management facility. Based on this raw data, a suite of value-added products will also be developed in the following months, with these products also being served at the ARM Archive. Appropriate meta-data sharing and cross-linking will occur via the MOSAiC Central Storage and with PANGAEA (World Data Center PANGAEA Data Publisher for Earth & Environmental Science (www.pangaea.de)) according to the protocol agreed upon between these two archives.

References

None

3.3 TROPOS – OCEANET: Remote Sensing of the annual Cycle of Aerosol, Cloud, and corresponding Radiation Closure Studies in the Central Arctic

Martin Radenz[1]

(not on board:) Ronny Engelmann[1], Hannes Griesche[1], Julian Hofer[1], Dietrich Althausen[1], Holger Baars[1], Patric Seifert[1], Albert Ansmann[1], Andreas Macke[1], Mario Mech[2], Bernhard Pospichal[2], Kerstin Ebell[2], Susanne Crewell[2], Gaël Dubois[3], Luc Blarel[3], Philippe Goloub[3]

[1]DE.TROPOS
[2]DE.UNI-KOELN
[3]FR.UNIV-LILLE

Objectives

Measurements of the atmospheric state in the Arctic are extremely rare and of great interest for climate research in this unique and changing environment. The mobile facility OCEANET is an ongoing observational initiative of TROPOS for aerosol and cloud profiling as well as radiation budget measurements in maritime environments onboard research vessels since 2007 (Kanitz et al., 2013, Bohlmann et al., 2018). One of the key focusses for TROPOS lies on heterogeneous ice formation processes in different areas of the world (e.g., Kanitz et al, 2011) and their radiative impact. During MOSAiC PS122/2 the OCEANET state-of-the-art en-route measurements were implemented on Polarstern in order to establish a full Arctic annual aerosol, cloud, and radiation data record.

The following research question are addressed within this project:

- How do aerosol- and cloud properties influence the annual cycle of short-wave and long-wave radiation under different meteorological conditions in the Arctic?
- How often does ice formation in warm (T > –10 °C) stratus clouds occur and what are possible freezing mechanisms under clean Arctic conditions?
- Can we observe different ice-formation rates in the presence of local and long-range transported ice nucleating particles?
- Will Arctic clouds increase or suppress the currently observed Arctic warming?

An additional focus is on ESA's Aeolus wind mission. OCEANET data will also support the CAL/VAL activities of this lidar satellite within the EVAA project. Since it is a polar-orbiting satellite, a large number of overpasses in the close vicinity of *Polarstern* occurred during PS122/3.

Work at sea

The OCEANET container of TROPOS was already installed on the bow of *Polarstern* at the container location C8 during MOSAiC Leg 1 (see Figure 3.3.1).

Since then continuous measurements with the

- the multi-wavelength Raman depolarization lidar Polly^{XT} (Engelmann et al., 2016),
- the microwave radiometers HATPRO (TROPOS) and LHUMPRO (UCologne),
- the ULille CIMEL sun/sky/lunar photometer (Yin et al., 2019),
- two disdrometers: OTT Parsivel² and 2DVD,
- a total-sky imager,
- a pyranometer and a pyrgeometer,
- a basic DWD weather station (T,p,r.h.)

were performed. A solar- and near-infrared irradiance spectrometer (CORAS/SRAPP) was added during leg 3 with the return of daylight.

***Fig. 3.3.1**: Location of the Oceanet container at the bow of Polarstern*

All instruments had to be monitored for proper operation and several maintenance and calibration tasks were performed to ensure high data quality. The microwave radiometers operated continuously, only the radome blower of LHUMPRO is broken since Leg 2. HATPRO was calibrated with liquid nitrogen during the handover leg 2/3 (Feb 28) and before the floe was left (May 2). The lidar Polly^{XT} also operated continuously. Gaps were only caused by laser maintenance (May 19) as well as crane and helicopter operations above the OCEANET container.

The robot of the CIMEL photometer, which should point the photometer towards the moon/sun, had occasional malfunctions. Likely, this was amplified by the extremely low temperatures in the beginning of March. Despite all the efforts taken to fix these problems, with the remote support of the engineers from the University of Lille, no completely reliable performance of the robot could be archived. Data quality has to be assessed on shore.

The Ott Parsivel2 laser disdrometer was destroyed by a crane operation on March 21. This caused a gap in the observations until April 8, when it was replaced by a similar instrument borrowed from the ARM facility (which was recovered from the ice as its wind shielding was destroyed). The 2DVD operated continuously, apart from minor maintenance tasks.

The pyranometer and pyrgeometer continued to measure on the bow-crane. This location is less affected by shading from the ships superstructure than the container roof.

In addition to the technical setup and maintenance of the OCEANET instrumentation an automatic profile retrieval algorithm for Polly^{XT} (dubbed Picasso) was used to make profiles of optical properties available in near realtime. This automatic dataset will be re-analysed later according to PollyNET standards (Baars et al., 2016).

One of the main goals of this project is to link the aerosol information to cloud structure and radiative effects. For this purpose, we could make use of the preliminary data from the ARM KAZR cloud radar, the regular radiosoundings on board, and from the OCEANET lidar and microwave radiometer data and implement the Cloudnet algorithms (Illingworth et al., 2007). In this way, synergistic products, like classification masks and microphysical retrievals, could already be derived shortly after the measurements. All quicklooks were made available within Polarstern's internal network.

Preliminary (expected) results

With the return of daylight, leg 3 marked the transition from winter conditions to springtime and early summer. With warmer airmasses, the amount of water vapor in the atmosphere continuously increased. The integrated water vapor (IWV) retrieved from brightness temperatures of the microwave radiometer observations shows this transition with high temporal resolution (Figure 3.3.2). Peaks were caused by pronounced warm air intrusions from the south, for example mid of March and mid of May with values up to 19 kg m^{-2}.

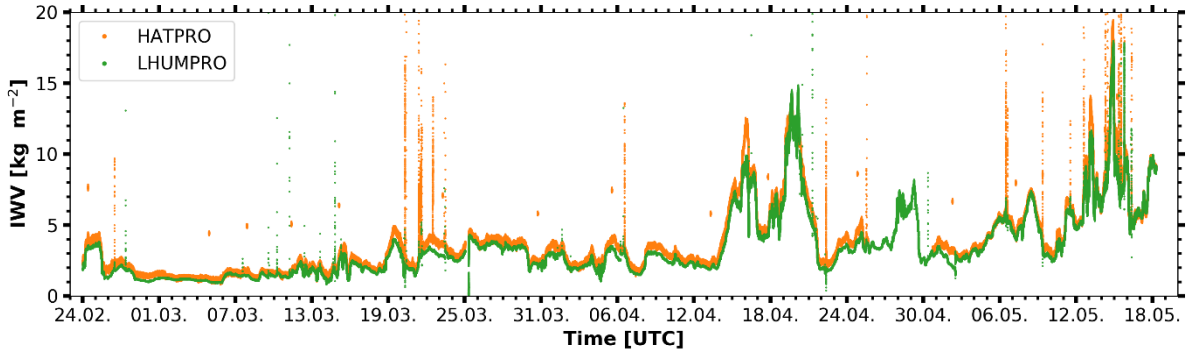

***Fig. 3.3.2**: Timeseries of integrated water vapor (IWV) during PS122/3. Retrieval is preliminary without comprehensive quality control.*

In early March the Raman lidar Polly^{XT} continued to observe aerosol layers up to the stratosphere, as during the previous legs. Single layers were present up to 15km height. Further in-depth analysis of the optical properties is required, but from first analysis hints to highly absorbing pollution aerosols from the long-ongoing Arctic fires in 2019 or mid-latitude continental sources. During the leg 3 enhanced aerosol backscatter was observed in the boundary layer with increasing frequency. These layers likely consisted of arctic haze and particles of marine origin. Figure 3.3.3 shows an example with pronounced aerosol layers up to 1400 m. The water vapor profiles (407nm channel; Guangyao et al., 2018) are of sufficient quality during the twilight season, but suffer from a low signal-to-noise ratio afterwards.

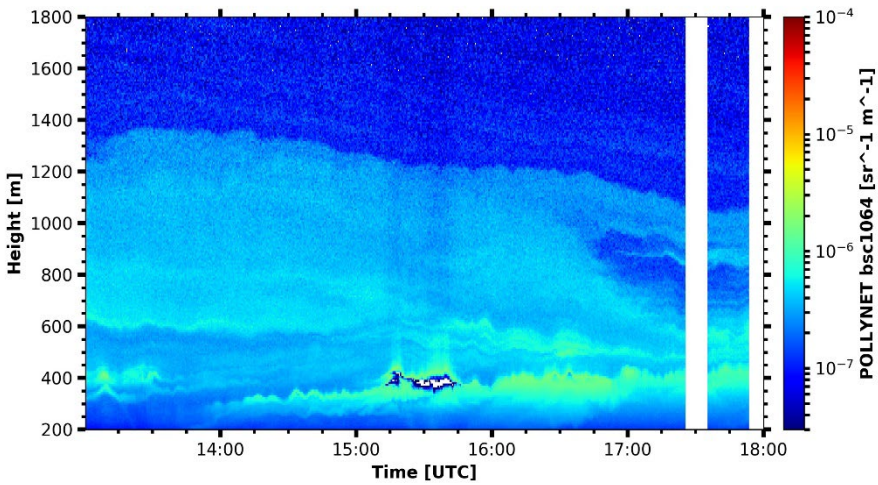

***Fig. 3.3.3**: Time-height cross section of backscatter at 1064nm observed with PollyXT on the 7 April 2020.*

The frequency of liquid layers increased with warming temperatures. Stratiform mixed-phase clouds were regularly observed in the boundary layer. An example is depicted in Figure 3.3.4 with cloud tops between 500 and 1500m (cloud top temperature around -10°C) and liquid layer base decreasing from 1000m to 400m. Ice particles were generated in the liquid layer during the whole period and sedimented out as a virga. Liquid water paths between 200 and 600 g m^{-2} indicate an optically thick cloud, which strongly modulates surface energy budget.

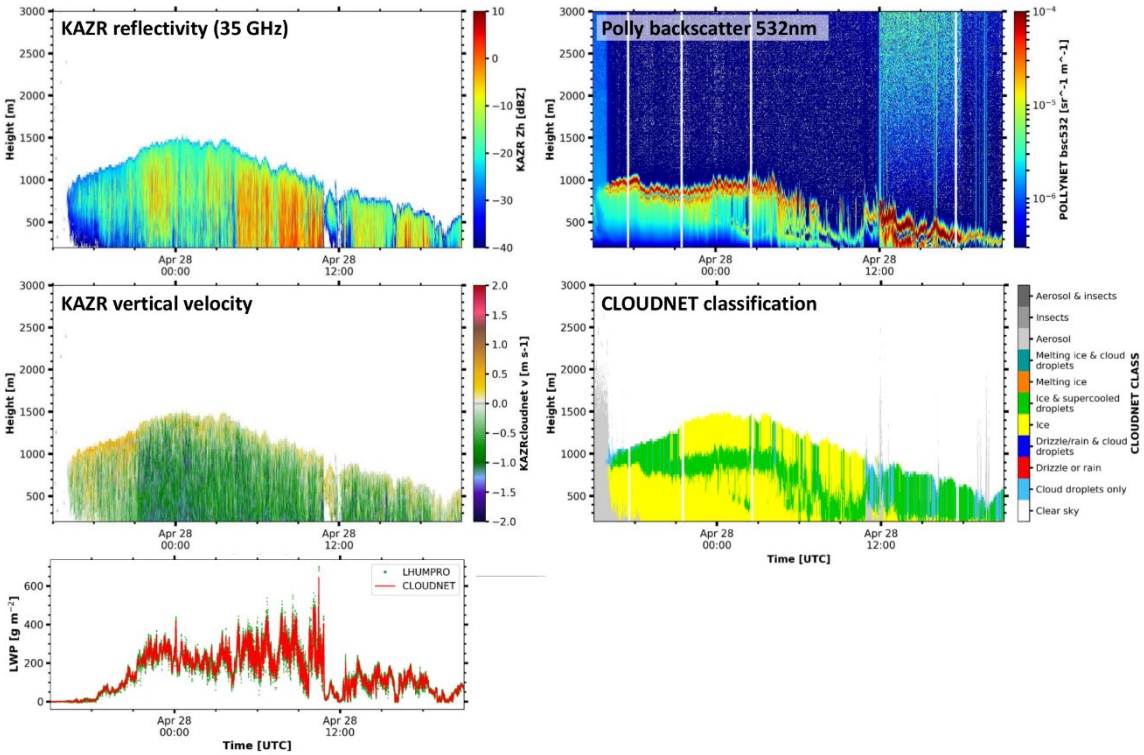

***Fig. 3.3.4**: Example of a stratiform mixed phase cloud observed on the 28 April 2020. Preliminary data without comprehensive quality control.*

Data management

All data are handled, documented, archived and published following the MOSAiC data policy (see APPENDIX). The raw data from the OCEANET platform are stored in the MCS following the MOSAiC data policy. The Polly^{XT} lidar data and quicklooks will be processed and made available through PollyNET (http://polly.tropos.de). Data will be stored at the PANGAEA data repository (World Data Center PANGAEA Data Publisher for Earth & Environmental Science www.pangaea.de.

References

Baars, H. et al. (2016) An overview of the first decade of PollyNET: an emerging network of automated Raman-polarization lidars for continuous aerosol profiling, Atmos. Chem. Phys., 16, 5111–5137.

Bohlmann, S. et al. (2018) Ship-borne aerosol profiling with lidar over the Atlantic Ocean: from pure marine conditions to complex dust–smoke mixtures, Atmos. Chem. Phys., 18, 9661–9679.

Engelmann, R. et al. (2016) The automated multiwavelength Raman polarization and water-vapor lidar PollyXT: the neXT generation, Atmos. Meas. Tech., 9, 1767–1784.

Guangyao D. et al. (2018) Calibration of Raman lidar water vapor profiles by means of AERONET photometer observations and GDAS meteorological data, Atmos. Meas. Tech., 11, 2735-2748.

Illingworth, A.J. et al. (2007) CloudNet: Continuous evaluations of cloud profiles in seven operational models using ground-based observations, Bull. Amer. Meteor. Soc., 88, 883-898.

Kanitz, T. et al. (2013) North-south cross sections of the vertical aerosol distribution over the Atlantic Ocean from multiwavelength Raman/polarization lidar during Polarstern cruises, J. Geophys. Res. Atmos., 118, 2643-2655.

Kanitz, T. et al. (2011) Contrasting the impact of aerosols at northern and southern midlatitudes on heterogeneous ice formation, Geophys. Res. Lett., 38, L17802.

Yin, Z. et al. (2019) Aerosol measurements with shipborne sun-sky-lunar photometer and collocated multiwavelength Raman polarization lidar over the Atlantic Ocean, Atmos. Meas. Tech., in press.

3.4. Atmospheric Surface Fluxes for understanding Sea-Ice Thermodynamics and Dynamics

Christopher Cox[2], Jennifer Hutchings[4]

(not on board:) Matthew Shupe[1,2], Ola Persson[1,2], David Costa[1,2], Ian Brooks[3], Thomas Ayers[2], Christopher Fairall[2], Michael Gallagher[1,2], Daniel Gottas[2], Jesse Leach[2], Sara Morris[2], Jackson Osborn[1,2], Sergio Pezoa[2], Taneil Uttal[2], Don Perovich[5], Timothy Stanton[6], Roberta Pirazzini[7]

[1]EDU.CU
[2]US.NOAA
[3]UK.ULeeds
[4]EDU.ORSU
[5]EDU.DARTMOUTH
[6]EDU.NPS
[7]FI.FMI

Objectives

This project collects observations pertaining to the vertical and lateral exchanges of energy through the sea ice, principally at the atmosphere-ice (snow) interface. Both thermodynamic (radiative, sensible and latent turbulent heat, and conductive fluxes) and dynamic (course/speed/bearing, momentum fluxes and properties of surface roughness) variables are observed. The objectives include increased understanding of the temporal evolution of the sea ice through the annual cycle, evaluation of the local physical processes responsible for the exchanges of energy through the ice, and identification of the drivers, both local and remote, that modulate the processes in play. This project contributes the atmosphere-ice energetic exchanges and is coupled with collaborative projects focusing on energy transfer through the snow and ice column and the upper ocean as well as the lateral dynamic stress and strain forces on the ice. Examples of inquiry related to project objectives are as follows:

- What are the relative contributions of thermodynamic and dynamic drivers of energy transfer across the atmospheric-ice-ocean system?
- What are the biases in thermodynamic and dynamic processes as a function of forecast time in numerical weather prediction models?

Anticipated outcomes from this work include improvements to sea ice forecast models from scales of hours to decades. This project is funded by the US National Science Foundation and the US National Oceanic and Atmospheric Administration.

Work at sea

Work during PS122.3 focused on maintaining this project's observational network that was installed during PS122.1 in the Central Observatory (CO) and MOSAiC Leg 1A at the Distributed Network L-sites. These installations included the 11 m tower at Met City and the Atmospheric Surface Flux Stations (ASFS) at each of the three L-sites. We also provided support for collaborative projects at Met City and on Polarstern.

Met City. As noted in in PS122.1 and PS122.2 cruise reports, ice dynamics in mid-November moved Met City relative to the CO and thus modified the intended sampling directions. During PS122.2 only small changes in the relative distance and bearing between Met City and Polarstern occurred and the situation at Met City at the beginning of PS122.3 was consistent with the PS122.2 report. This situation changed early in PS122.3 when the shear zone that first appeared in PS122.1 became active again, in particular during two prolonged periods of approximately three weeks that were separated by a three-week period when dynamics were more localized and less impactful on Met City installations. The first dynamic period at Met City was between March 11 and March 31 and the second was between April 19 and May 10 (Figure 3.4.1). These events had significant impacts on access to the station and it is estimated that approximately 90 unique cracks, leads and ridges were traversed, many numerous times, by personnel to access the site (J. Schmale, personal communication). Significant efforts were

made by Team ATMOS to keep Met City in place and running so as to maintain continuity of the time series and to keep the OCEAN-ICE-ATMOS collaboration there coupled as long as possible. PS122.3 was successful in this endeavour throughout March, April and leading up to Polarstern's planned departure date of May 15. However, on May 10 ice conditions and logistical complications with the Leg 3-4 transfer forced a complete decommission of Met City.

The first dynamic period was characterized by a relatively small number of long, repeatedly-active cracks where energy was highly concentrated. For example, ridges in the immediate vicinity of Met City reached 3-4 m and the width of the lead in the sampling sector reached approximately 500 m before closing again. The surface roughness of the area increased in all directions, but in particular on the CO and Polarstern sides of the tower. These ice dynamics began on March 11 with a 10 m wide crack forming between the 23 m mast and the 11 m tower. This forced a disconnect of the power and data lines between Met City and the ship as well as disconnection of the power and data lines that ran between Met City and the 23 m mast and an instrument hosted at the Met Hut and run by the ECO Team, the "Fish Cam". Met City was placed on generator power per SOP designed during PS122.1. Movement continued over the next several days including the formation of a second lead on the other side of the 11 m tower that made a peninsula from the ice surrounding Met City and separated a "Rocket Trap" (M. Frey) snow sampler from the site. This initiated further responsive actions: on March 12 the Picarro (Blomquist) was removed because its power requirements exceed the rating of the generators and on the 13th the disdrometer (ARM) was removed after damage to its snow fence by ridging. The Rocket Trap was lost. On March 14 a fuel drum was installed and used as an auxiliary gas tank for the generator, without which continuous operations at Met City could not be supported (see Table 1 for uptimes at the tower). Ridging at this time put the ARM installations in imminent danger and on March 17 the ARM equipment was retreated back towards the Met Hut. The sodar and lidar (Brooks) were also taken down because of cracks forming nearby. The 23 m mast was taken down because ridging from the original lead had approached to within 1-3 m of two anchor lines. These actions created disturbance of the snow in the vicinity of the ARM equipment but not in the 11 m tower area. The ARM albedo rack was repositioned to a safer area with undisturbed snow. Moving the albedo rack was in fact beneficial as repositioning this structure was already under consideration after the appearance of ridge nearby during PS122.1 was expected to cause undesirable shadowing in the FOV. The timing of the move was also fortuitous for the shortwave measurements because it occurred near in time to sunrise, thus avoiding a discontinuity in the solar record. However, note that a discontinuity may be present in the upwelling longwave radiation depending on the similarity of the ice profile in the FOV between the two locations. A second radiation station (FMI) was in a stable area and was not moved. The re-siting and local snow disturbance is not expected to have had negative impacts on the other measurements. The sodar was reinstalled nearby on March 22 but technical problems prevented it from being fully functional until April 2. The lidar was reinstalled near Ocean City on April 4 where the ice was more secure and power was more stable. Refer to Images 1-4 for examples of the modified layout of instrumentation at Met City.

During the first three weeks of April ice conditions were comparably stable with mostly localized areas of action that was more a hindrance to travel than to utilities and with little threat to installations at Met City. The power line was reconnected and a radioLAN was installed in place of the fibre optic data cable. On April 19, opening of the ice again in several places beneath the Met City power line with leads between 2 and 15 m forced a disconnect of the power and a return to generator use. Shortly thereafter it was decided that the technical requirements of the VISSS instrument could not be supported at Met City and VISSS was taken down on April 26 and installed on the P-Deck of Polarstern where it began collecting data again on April 30. This April period of ice strain was characterized by warmth and widespread opening of the ice with relatively little or weak ridging and weak ice growth rates. Later during the first week of May more intense ridging over the same widespread area began in earnest with continued warmth and little refreezing. Access to Met City became very difficult. Opening and closing ice conditions varied frequently, in particular following a shearing event

early on May 3 that moved Met City approximately ½ km back in front of the Polarstern bow into the most concentrated area of the shear zone. These considerations were factored in when planning for the partial take down of Met City in preparation for Polarstern's departure to the ice edge for the Leg 3-4 transfer, scheduled for May 15. Packing of the ARM equipment began May 8. Plans had been made to make the 11 m tower autonomous on generator power during the time Polarstern was away. However, with the significant deterioration of the ice conditions at Met City, including the opening of a crack on the far side of Met City taking it inside the shear zone; formation of small (< 5 cm) cracks between the installations after this; a reduction of the diameter of the Met City "island" from more than 160 m at the end of April to < 75 m; and noticeable motion of the floe during visits, it was concluded on May 9 that Met City would not survive to the return of Polarstern in June and the site would be decommissioned immediately. The decommission, already begun with the removal of the ARM equipment, was carried out on May 10-11 ahead of a Bft 10 storm forecasted for May 13. All above-ice equipment was removed, including batteries, gasoline, generators, instrumentation and structures. The plywood Met Hut and a metal computer rack inside were left behind along with wooden power poles and all of the buoys (SIMB3, DOT, AOFB, spar, mapper, SVP). On May 12, ice movement during the approach of the storm largely destroyed the Met City site. After the departure of the storm the ice began closing and ridging commenced once again. Reconnaissance on May 14 located SIMB3, DOT, AOFB, mapper and SVP though none were on stable ice. Plans were made for an attempted recovery of the AOFB, DOT and mapper using the ship's cranes after repositioning of the ship the following day. However, further working of the shear zone on the evening of the 14th was observed. On May 15 a second visit confirmed substantially more deterioration of the site and failed to locate any of the buoys except for the SVP marker. Met City was abandoned in place to be re-evaluated in PS122.4.

Tab. 3.4.1. *Uptimes for measurements at the 11 m tower during PS122.3.*

Period	Date	Tower uptime
1st stable period	2/24-3/11	98%
1st dynamic period (no drum)	3/12-3/14	34%
1st dynamic period (fuel drum)	3/15-3/31	91% (86%*)
2nd stable period	4/1-4/18	89%
2nd dynamic period	4/19-5/10	96%
Overall	2/24-5/10	93% (92%*)

* some additional data loss from "slow" data streams associated with power problems

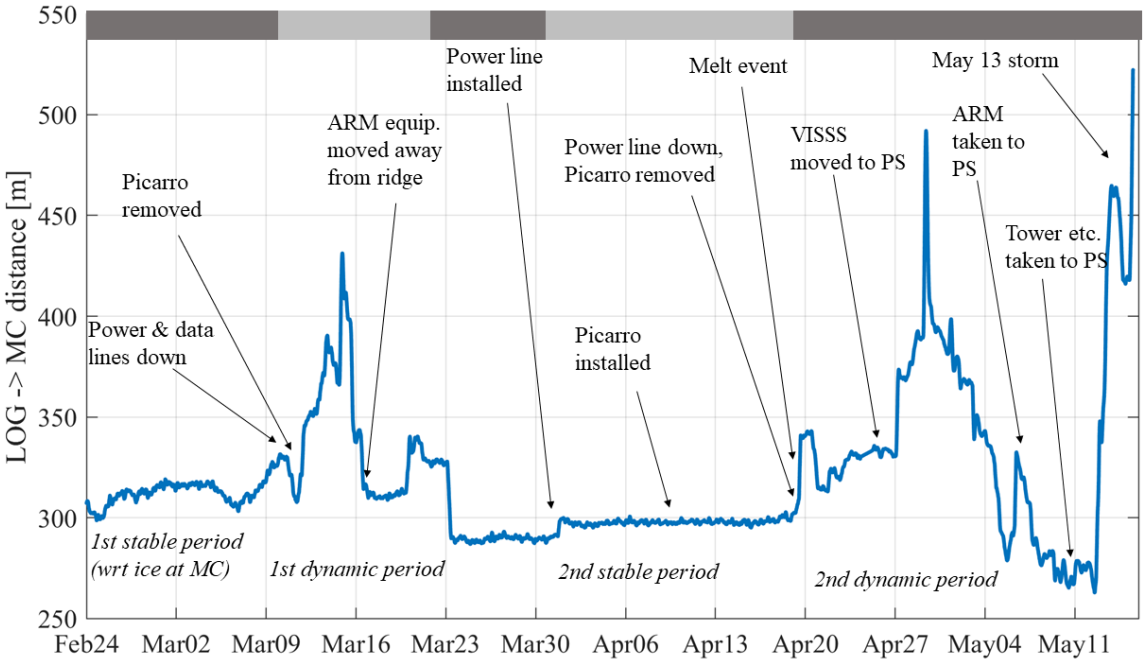

Fig. 3.4.1. *Distance between the Logistics Area (LOG) and Met City (MC) during PS122.3 (calculations provided by M. Radenz) with notable logistics events related to work at Met City highlighted. The dark grey bars on the top are periods that may be broadly characterized by opening ice conditions and the light grey bars are closing ice conditions.*

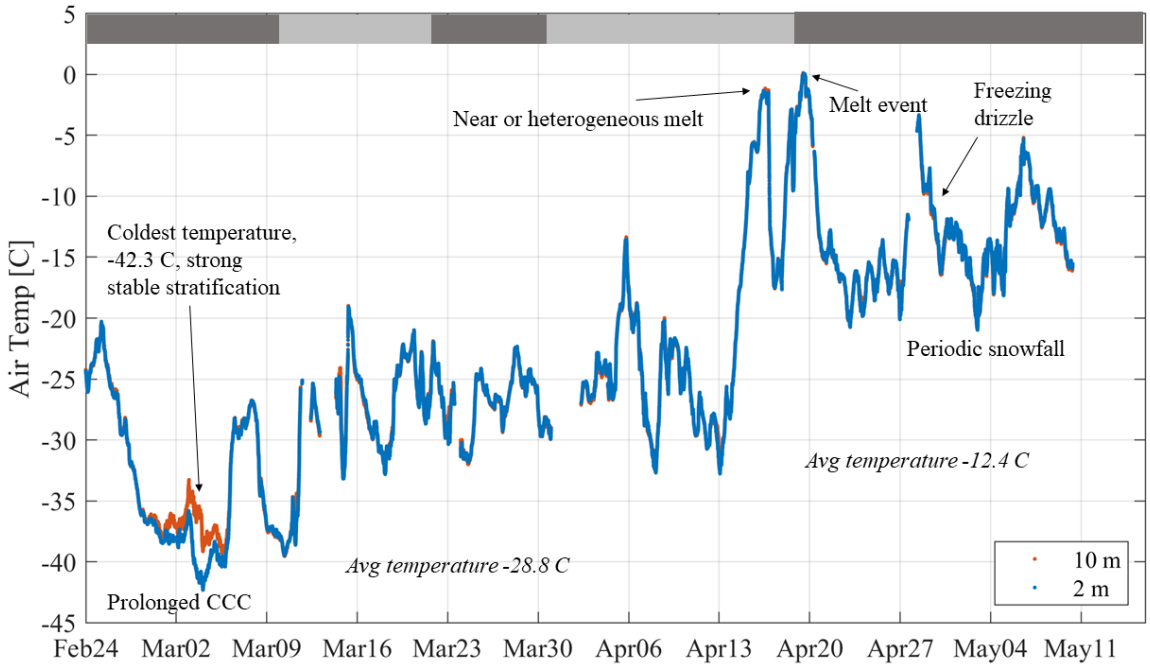

Fig. 3.4.2. *Air temperatures measured at 10 m (red) and 2 m (blue) from the 11 m tower at Met City. Several notable weather-related events are highlighted. Gray bars are as in Fig.3.4.1.*

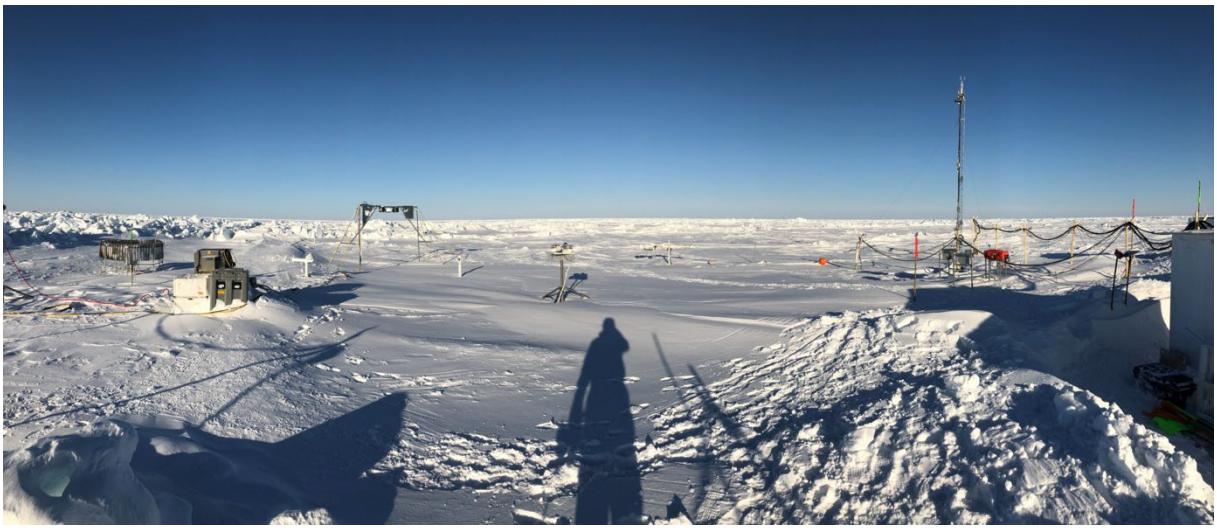

Fig. 3.4.3. *Photo of Met City facing northeast on April 17.*

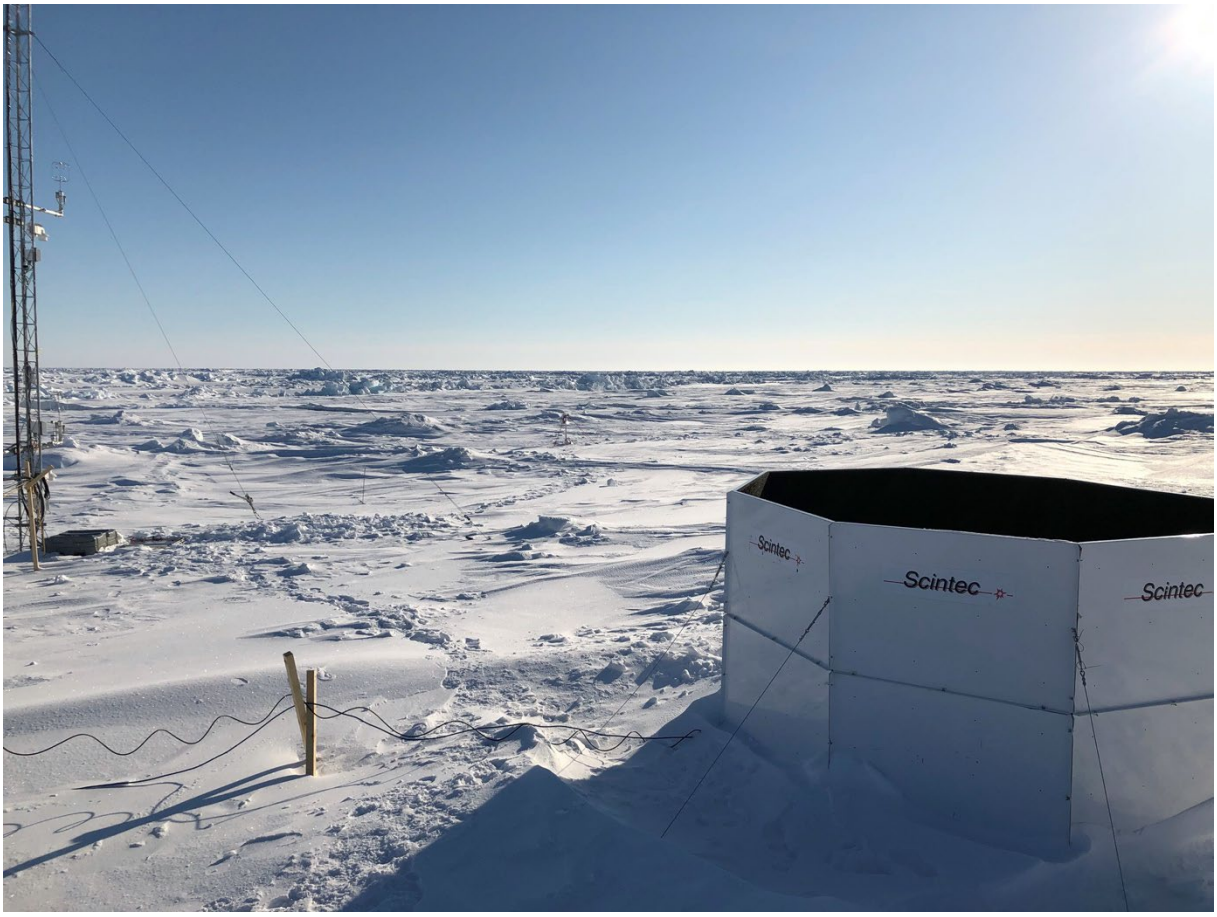

Fig. 3.4.4. *Position of the new sodar location between the tower and Met Hut, 11 m tower visible in the background. Photo taken near the Met Hut looking east towards the sampling sector on April 25.*

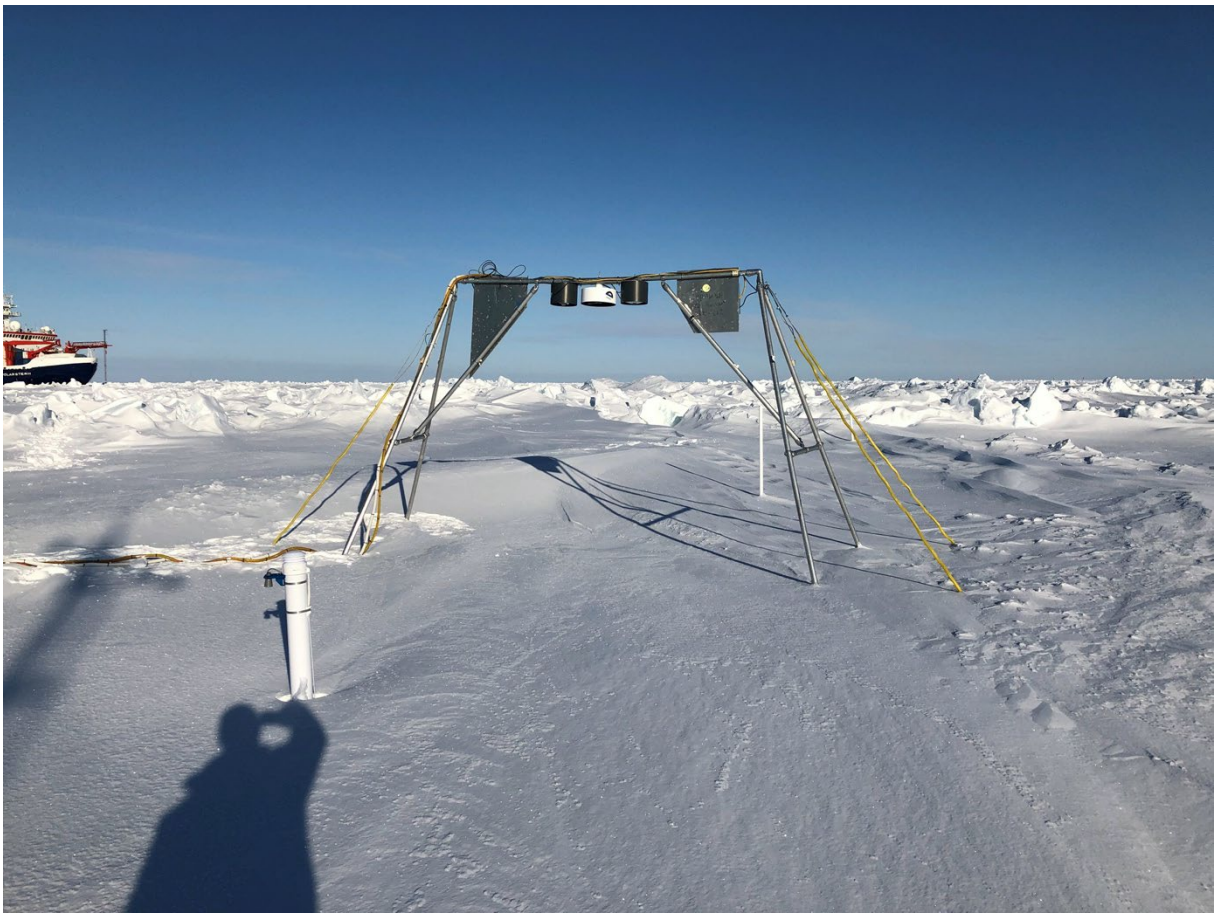

Fig. 3.4.5. *ARM albedo rack on April 25.*

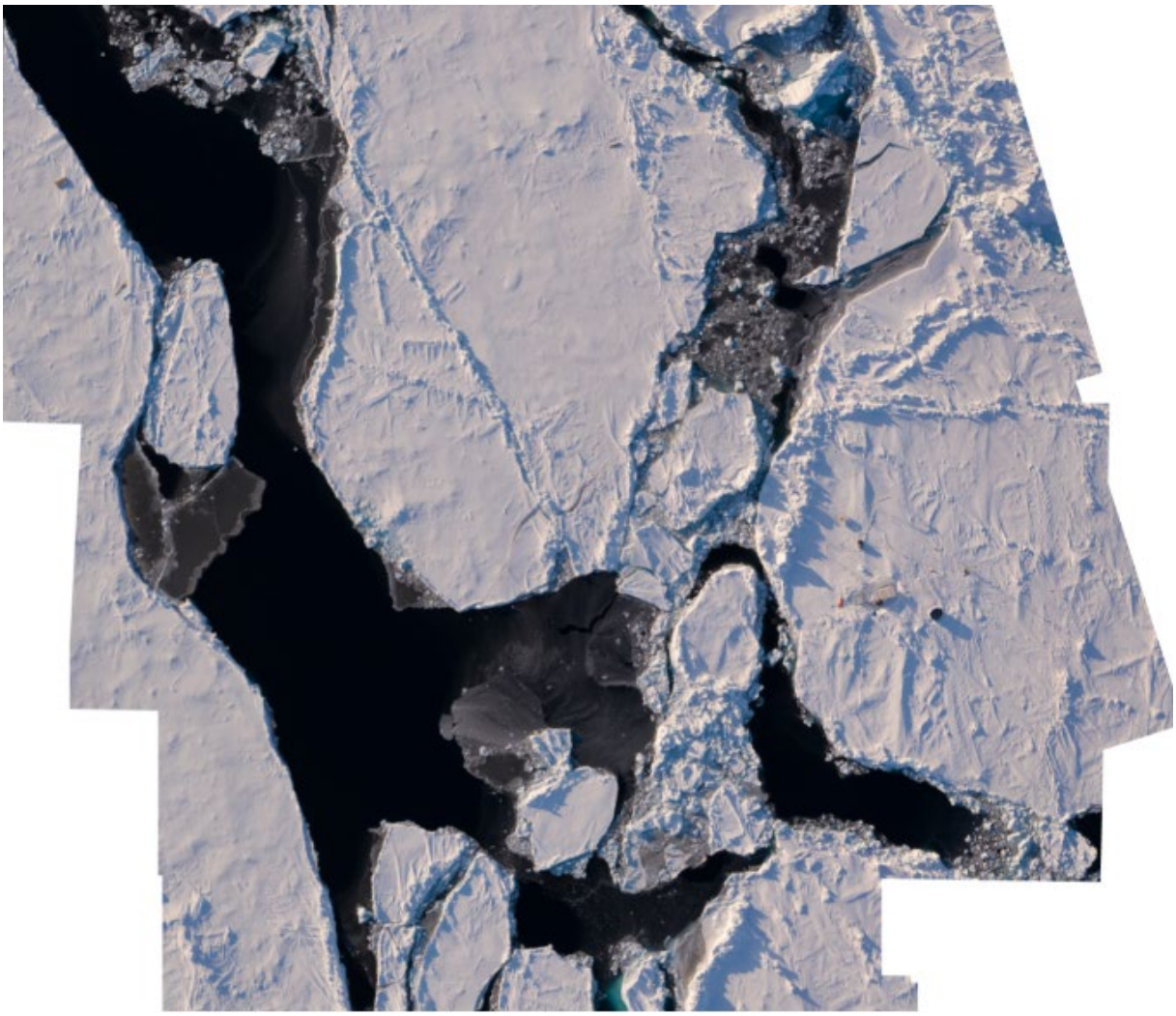

Fig. 3.4.6. *Photo taken from a drone by M. Ernst (UFA) on April 29. The Met City installations to the right in the photo below center. The top of the photo is roughly north. Polarstern is out of the frame in the direction of the upper left, the CO to the left (also out of frame) and the sampling sector to the right.*

Distributed Network. This project deployed ASFS at each of the three L-sites in October. In February (during PS122.2), a ridging event severely damaged the ASFS at L3. It was moved to stable ice and abandoned in place until sunrise when PS122.3 would be able to airlift the system back to Polarstern. This operation was completed on March 26 and repairs commenced, which returned the station to working condition. The PS122.2 team also reported loss of communications with ASFS at both L1 and L2 in the last week of February just prior to the handover. Conditions were not suitable for flying, but snow machines were used to access L2 on March 4 where the system was found to have suffered a deep freeze and was revived. The L2 station continued to suffer from freezes in the exhaust line and/or within the fuel cell generator, which was exchanged two more times in March with degradation in efficiency observed after each restart, building upon similar reductions in efficiency compounding since PS122.1. At this time the power production fell below the minimum requirements and the L2 station was no longer viable in autonomy. Because a resupply of needed parts originally expected for the first week of April was cancelled, the station was recovered for use at the CO. For the same reasons it was not possible to return the second working ASFS back to L3. L1 was visited on March 18 and was found to have been destroyed by a ridge and a return for recovery of the system was carried out on March 21. However, the ASFS was largely inaccessible after a subsequent ridging event crushed it beneath several meters of ice; only 10-20% was recovered. A third attempt at recovery was carried out on May 5 by team members collecting samples at L2, but no further material was able to be retrieved from the ASFS. Unfortunately, the L-site ASFS experiment was been tabled for most of PS122.3 and awaits

resupply in PS122.4. However, for PS122.3 the two surviving ASFS were converted into units that could be connected to line power and became valuable observers within the CO beginning the second week of April, described next.

BGC1 and Balloon Town. The 23 m mast, two ASFS and the lidar were taken to the middle of the CO where the ice was sufficiently stable and line power was available. The mast and one ASFS was installed in the southern (i.e., Ocean City) edge BGC1 near an old ridge. The ice thickness ranged from 1.7 to ~4 m. The ASFS was positioned so as to have a similar sampling FOV for the sonic as at Met City but note that the nearby FOV (i.e., BGC1 and Snow 2) had more level ice than the sampling sector at Met City. Both the 23 m mast and ASFS were installed on April 14 and a SIMBA buoy was installed next to the ASFS on April 16. The lidar was set up near Ocean City. On April 15 the second ASFS was installed 30 m south of the Balloon Town tent alongside the AWI mobile eddy covariance sled. This collaboration was carried out with the expectations of warm, moist southerly air masses forecasted for later in the week and the sleds were positioned accordingly. The ASFS at Balloon Town was removed on May 2 and outfitted with a repaired fuel cell generator that made it autonomous once again. It was then swapped with the ASFS in the BGC1 position and run autonomously (i.e., off of line power) there beginning May 7. The other ASFS was returned to Polarstern for secure storage during the Leg 3-4 transition. The autonomous BGC1 ASFS was left in place to collect data and transfer it via satellite when Polarstern departed the floe on May 16. As of this writing (May 31), 1 min averages of collected data continue to be received every half hour from the ASFS at BGC1.

Orientation. The ice dynamics in the vicinity of Polarstern and Met City during PS122.3 pose a complicated problem for restructuring the relative wind directions and baselines for heading at the tower and the mast. This problem is particularly challenging because both of these positions were also moving relative to the main floe so it is insufficient to use Polarstern as a baseline for PS122.3. A baseline will be retroactively established by using GPS receivers installed at various locations in the CO, and GNSS receivers on the 11 m tower. After the 23m mast was moved to BGC1, it was deployed with a GNSS receiver as well. At Met City there are several buoys and the Met Hut AIS that can be used to make baselines with the tower GPS. The AIS provides the most frequent data, so we intend to use this time series of position together with the mast GNSS to estimate floe rotation and heading changes. The 23 m tower was redeployed on the central floe where the majority of the MOSAiC CO infrastructure was placed. There is an AIS placed at Ocean City that remained on the same piece of ice as the tower. We will build a similar baseline to calculate floe rotation with this AIS and the 23m tower GNSS. Two GNSS/INS stations were placed at Balloon Town and in the logistics area during the time the tower was recording relative positions with centimetre accuracy. These can be used to build an accurate compass for the tower, to investigate the accuracy of the AIS/GNSS compass, and determine the error on the heading estimate for Met City tower.

Preliminary (expected) results

Previous cruise reports outlined the physical thermodynamic process understanding that will be a focal point of the research. The key processes of interest during PS122.3 involve the transition from longwave-dominated to an all-wave net radiation budget with the arrival of the sun, temporal evolution of surface albedo, the effect of turbulent heat and momentum transfer with changing surface roughness, the latent heat loss from leads, the causes and consequences of surface melt, and the timing and drivers of the switch from a net negative (wintertime) to net positive (summertime) surface energy budget.

Despite significant losses at the L-sites and challenging logistical conditions at the CO, a rich record of data pertaining to the surface energy budget over sea ice during late winter into the summer transition was collected during PS122.3, and a number of exciting events and features of this seasonal shift were successfully captured.

Local net accumulation of snow beneath the 2 m boom at the 11 m tower was near zero for the duration of PS122.3 with the most notable feature in the time series (not shown) being a loss of approximately 3 cm on April 15/16. This corresponded to a southerly warm air advection

event that represented a distinct transition from winter-like to summer-like conditions at the CO, which is visible in the air temperature record (Figure 3.4.2). From February 24 to April 14 the mean 2 m air temperature at the CO was -28.8 C and after April 14 it was -12.4 C. The early period included the lowest 2 m air temperature recorded during the MOSAiC winter, -42.3 C on March 4, which occurred near the end of a prolonged (5 day) period of clear and cold conditions having a persistent temperature inversion with a gradient up to 6 C between 2 and 10 m height. Stable stratification of the boundary layer was otherwise both weaker (< 3 C) and less persistent (hours rather than days) for the remainder of PS122.3.

The first warm air intrusion event that marked the spring transition was associated with an increase in temperature from -33 C to -1 C between April 13 and 16. It was accompanied briefly by mixed phase clouds with thermodynamic temperatures warmer than the surface (but still below freezing), resulting in longwave-driven positive net radiative forcing on the snow pack. While the measurements do not indicate that surface melting occurred during this initial warming event, surface skin temperatures did reach ~ -1 C and, qualitatively, the character of the surface snow changed, including liquid content within the snow (S. Arndt, personal communication) and the appearance of widespread areas of icy glaze noticeable on April 17 and suggestive of heterogeneous refreezing. Because of high cloud liquid water paths and below freezing temperatures aloft (based on analysis of quicklooks provided by M. Radenz, OCEANET/TROPOS), the lack of radiometric evidence of melt, and below-freezing snow temperatures recorded in the Dark Site by the ICE Team on April 16 (S. Arndt, personal communication), the apparent occurrence of melt, even if heterogeneous, is difficult to explain. Analysis of this event should also consider scoured areas exemplified by an aged snow surface that are reported to have been saline by the ICE Team (though the salt content was generally low) or whether occurrences of freezing drizzle may have played a role in wetting the snowpack.

Shortly following the first advection event was a second that did warm the surface to 0 C and melt was thus observed radiometrically for 45-90 minutes on April 19 from measurements made at three locations around camp; the Met City tower, ASFS30 (Balloon Town) and ASFS50 (BGC1). On this same day, 32 minutes of above-freezing air temperatures were also observed at the tower in association with a slightly positive temperature gradient along the tower, indicating downward turbulent transfer of warm air from above. Changes in the albedo associated with both transitions between diffuse- and direct-dominated global radiation and changes in the properties of the snow surface before and after the warming events are observable in the second half of April (Figure 3.4.7). The ICE Team also reported weak growth rates of both new and old sea ice during this time, which was consistent with limited preliminary analyses of the surface energy budget that indicate the second half of April to be characterised by the following: (1) positive net radiation on cloudy days supported by near-neutral net longwave combined with weak shortwave forcing and (2) on clear days positive net radiation during mid-day (shortwave absorption possibly enhanced as a result of the melt) followed by negative net radiation during the half of the day when the sun was lower in the sky, resulting in near neutral radiative absorption in the daily mean. While compensatory fluxes from turbulent processes has not been reviewed, the net all-wave radiation was found to be a close match to the near-surface conductive fluxes measured in the snow pack during this time.

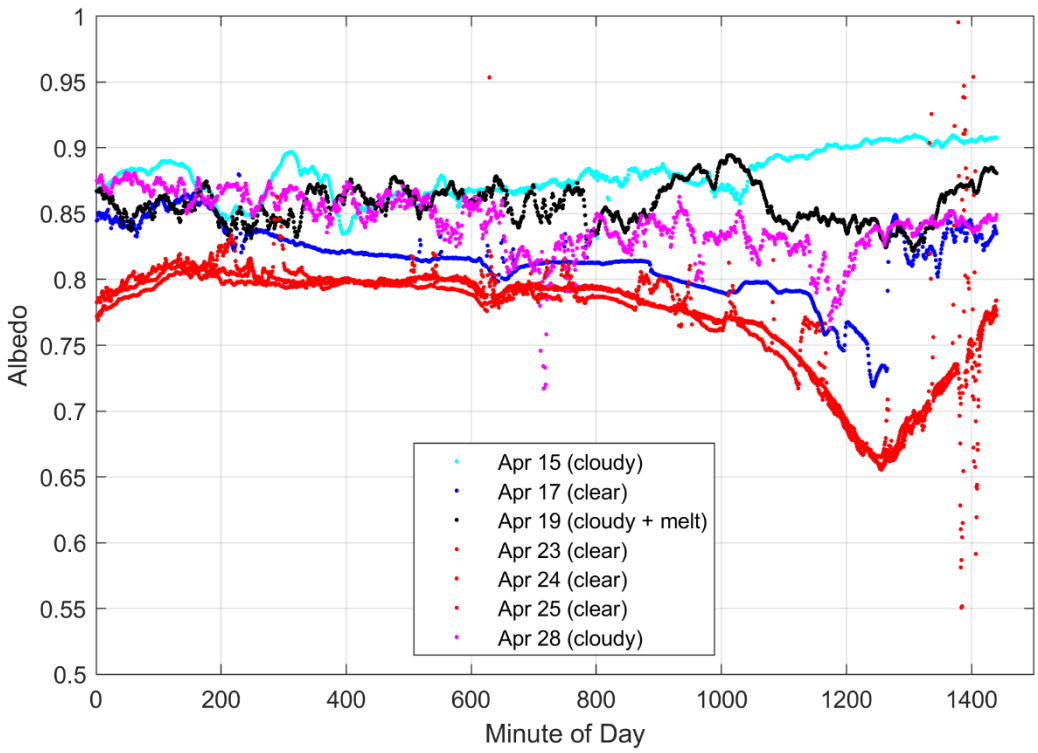

Fig. 3.4.7. *One minute average albedo on seven different days in the second half of April from ASFS50 in BGC1. Large decreases in albedo around 1300 min on clear days are an artefact from the shadow of the ASFS structure. Diffuse-dominated conditions have albedo at or slightly above 0.85 while clear days have lower albedo. The occurrence of melt on the 19th and appearance of ice below the downward facing pyranometer lowered the albedo during clear skies by ~2% from a comparison of clear sky albedo before the melt on the 17th (blue) and after on the 23rd-25th (reds).*

A number of storms were measured throughout PS122.3; the air pressure (2 m) fell below 990 hPa during six unique synoptic events between February 24 and May 10 with the maximum wind velocity at 10 m exceeding 16 m/s during five separate events. Unfortunately, a significant fraction of the relative wind directions at Met City, in particular during the first half of the leg, originated from the direction of the CO (Figure 3.4.8). However, significant areas of open water, occasionally producing steam fog (e.g., March 14, March 23) were observed and some cases of leads opening and closing and/or refreezing nearby and upwind of the tower over the course of hours were observed (e.g., April 2). Observing capabilities for these events were improved in early PS122.3 when the open-path gas (h2o, co2) analyser at the 11 m tower was retrofitted with a heater for ice mitigation. The heater increased the uptime for this instrument from ~30% in PS122.1-2 to ~95% after installation on March 8.

Preliminarily, the onset of the summer melt at the CO (wrt the surface) was observed by the ASFS beginning on May 25. From May 25 to 28, 70 consecutive hours of above-freezing near-surface air temperatures were recorded with only a brief (< 2 hour) interruption early on the 26th; other signs of melt including surface skin temperatures of 0 C and decreases in albedo were also observed. The melt was brought on by warm, humid air masses advected from the south by a low between Greenland and Svalbard. From the 28th through the time of this writing on the 31st air temperatures remained close to freezing with intermittent periods of melting observed.

Other notable weather events during PS122.3 include freezing drizzle on April 28; a Beaufort 10 storm on May 13 and 14 (observed from the ASFS at BGC1 but after the tower was decommissioned); the first significant springtime fog event on May 16 (observed from ASFS); rapid cooling, high winds and snow on April 20 following the second warm air intrusion; a

significant blowing snow event on April 21, and several days with low wind and snowfall beginning April 30.

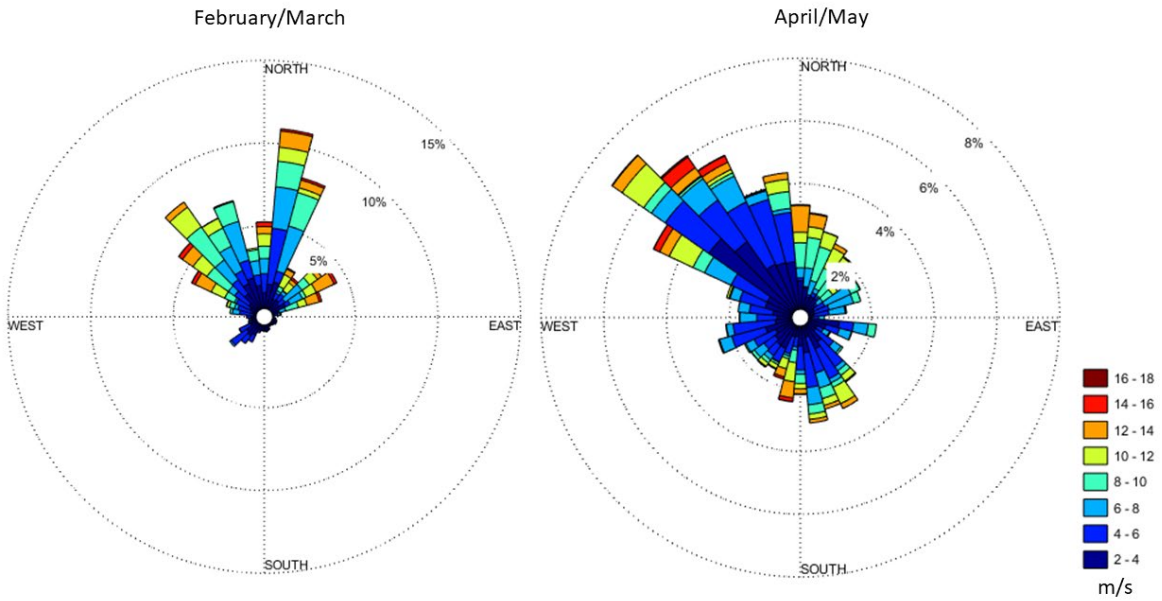

Fig. 3.4.8. *Wind rose based on 1 min avg wind data from 10 m height on the Met City tower in PS122.3 from February 24 through March 31 (left) and April 1 to May 10 (right). Met City was east of the CO and generally south/southeast of Polarstern.*

Data management

Data will be stored at the Arctic Data Centre following the agreement between ADC and the MOSAiC Project lead. DOIs will be communicated to PANGAEA for later access via the future MOSAiC Data Portal.

References

None

3.5. Trace Gas Flux Group

Ludovic Bariteau[1,2], Hans-Werner Jacobi[3]

(not on board:) Byron Blomquist[1,2], Steve Archer[4], Detlev Helmig[1], Jacques Hueber[1], Laurens Ganzeveld[5], Christopher Fairall[2], Dean Howard[1], Kevin Posman[4], Helene Angot[1], Sjoerd Barten[5], William Sturges[6], Lucy Carpenter[7]

[1]US.CU
[2]US.NOAA
[3]FR.UGA
[4]US.BLOS
[5]NL.WUR
[6]UK.UEast Anglia
[7]UK.UYork

Objectives

The principal scientific objectives of the MOSAiC trace gas flux group concerne the air-sea exchange of climate-active trace gases and the transport, reactivity, surface exchange, and chemical atmospheric budgets of a range of organic compounds (VOCs and CFCs) and elemental mercury. The measurements initiated on leg 1 of MOSAiC including continuous eddy correlation (EC) flux measurements; continuous concentration measurements of trace gases including VOCs, CFCs, nitrogen oxides (NO/NO_2) and Hg^0; and dynamic chamber flux measurements over undisturbed snow and ice were pursued.

Since tropospheric atmospheric chemistry in the spring over the Arctic Ocean is characterized by the depletion of ozone, additional measurements were performed to determine profiles of ozone concentration in the lower atmospheric layers before, during, and after periods with low ozone. Such profiles were obtained with the help of the tethered balloon system (chapter 3.1) and will be used to analyse dynamical and chemical processes related to the destruction of tropospheric ozone.

The observational records will feed into modelling activities with a number of objectives: the development of a physical gas transfer parameterization suitable for the sea ice environment, 1D modelling of the atmospheric surface exchange, vertical transport and reactivity of these gases, and 3D modelling to assess the significance of the air-sea transfer in the Central Arctic for regional and global atmospheric trace gas budgets.

Work at sea

Table 3.5.1 provides a list of the measurement systems deployed since leg 1 with their location, sampling frequency, and SensorWeb short name, which were operational on leg 3. Details for these systems can be found in the report for leg 1. Beside the DMS mass spectrometer not running due to a faulty power supply, all instruments installed during leg 1 were operating as expected.

Concentrations and Fluxes: Figure 3.5.1 shows the number of hours of operation per day for each measurement systems deployed during leg 3 as well as periods when the wind was in the favourable sector for flux measurements at the bow tower. About 63 % of the data meet the criteria for good wind conditions defined as wind directions within +/- 130° relative to the ship's heading and wind speeds above 1 m s^{-1}.

As with previous legs, the LI-COR 7500DS did not operate reliably during frost conditions, but improved with increasing solar radiation levels, when the optical elements were mostly free from obstructions. The slow ozone system, the GC/MS, and the Picarro installed on the ship ran continuously when wind conditions were adequate. The fast ozone and NOx systems as well as the mercury analyser were operating most of the time and required some maintenance and trouble shooting.

Tab. 3.5.1: *Measurement Systems Deployed for Leg 3*

Measurement System	Sampling Location	Sample Rate	SensorWeb 'Short Name'
Picarro G2311-f CRDS	ship bow tower	10 Hz continuous	crds_ghg_ship_bow
Chemiluminescent Ozone	ship bow tower	10 Hz continuous	ozone_fast_ship_bow
Metek uSonic-3 Anemometer	ship bow tower	10 Hz continuous	sonic_anemometer_3D_ship_bow
Licor 7500DS	ship bow tower	10 Hz continuous	licor_7500ds_ship_bow
RM Young 86004 Sonic Anemometer	ship bow tower	1 Hz continuous	sonic_anemometer_2D_ship_bow
Michell S8000 hygrometer	ship bow tower	~1 per minute	t_rh_ship_bow
Chemiluminescent NO/NO2	ship bow crane	10 per minute	nox_ship_bow
TEI model 49C ozone analyzer	ship bow crane	1 per minute	ozone_slow_ship_bow
Tekran 2537B mercury analyzer	ship bow crane	1 per 5-15 minute	hg_ship_bow
Agilent GC Mass Spectrometer	ship bow crane	~15-18 per day	gcms_ship_bow
Picarro G2311-f CRDS	Met City 10 m tower	10 Hz continuous	crds_ghg_ice_station_tower
TEI model 49C ozone analyzer	Met City 10 m tower	1 per minute	ozone_ice_station_tower
CO2/CH4 Flux Chamber	various	1-2 per deployment	co2_ch4_chamber_portable
Electrochemical cell for ozone on tethered balloon	Balloon Town	1 Hz	ozone_profiler

The Picarro and the ozone detector at Met City did not run from 11 March to 9 April. During that period, the ship's power to Met City got disconnected due to active leads and ridges and it was supplied only by power from local generators with limited capacity. Once ship's power was re-established, the both instruments were redeployed on 9 April, but Met City was disconnected again on 19 April due to the formation of new leads. On 20 April the Picarro instrument was finally recovered and is since then stored on the ship. The ozone detector continued running on local generator power until the dismantling of most of the instrumentation at Met City on 9 May.

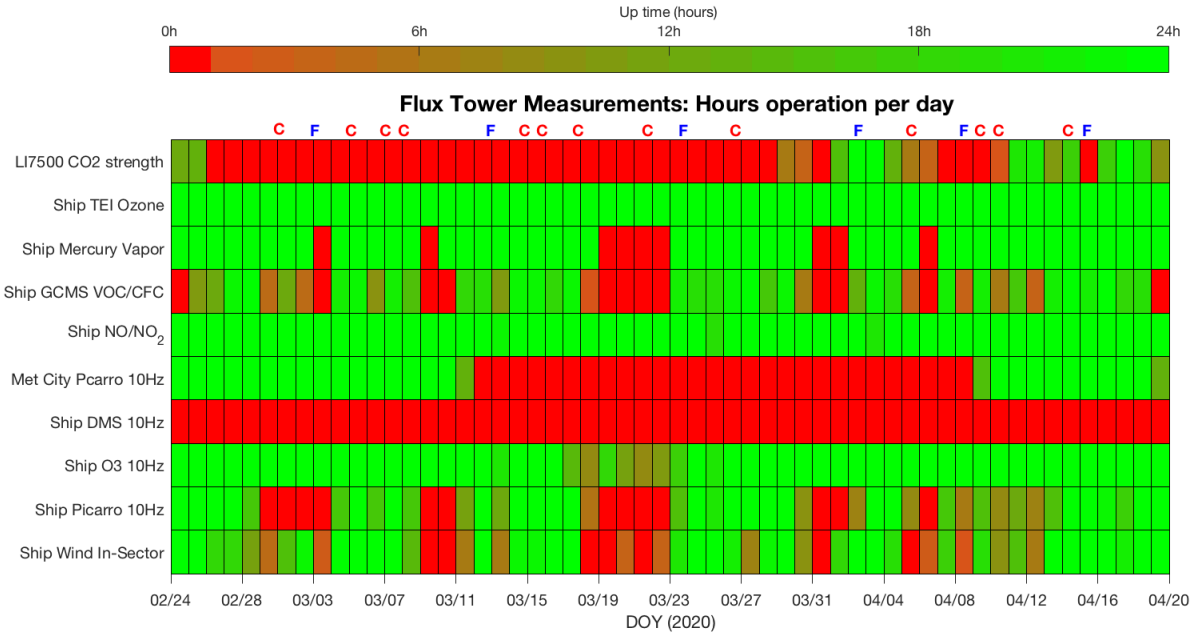

Fig. 3.5.1*: Preliminary analysis of the hours of operation of the flux systems on the ship and at Met City and the trace gas analyzers for the period up to 20 April. The last line indicates periods with wind directions from the 'clean' sector as defined by +/- 130° relative to the ship's heading. Green indicates continuous operation, while red indicate no measurements. At the top, air samples collected with Flasks (F) and deployments of the dynamic CO2/CH4 flux chamber (C) are indicated.*

Whole Air Flask Samples: In addition to the *in-situ* trace gas measurements described above, we collected weekly whole air samples in glass flasks for greenhouse gas analysis by the NOAA Global Monitoring Division as initiated on leg 1. Similarly, we continued the sampling for halogenated compounds using the stainless steel flasks provided by the University of East Anglia (UEA), which began on leg 2. All samples were taken on the platform of the bow crane during favourable wind conditions on 4, 14, 24 March, 3, 9, 16, 24 April, 4, 10, and 20 May. The NOAA/GMD samples will be shipped to the NOAA facility in Boulder, Colorado at the end of the cruise leg, while the other samples will be shipped to UEA at the end of the MOSAiC campaign for analysis.

CO_2 / CH_4 Flux Chamber Measurements: The dynamic flux chamber system for CO2 and CH4 was deployed 13 times at a variety of locations as listed in Table 3.5.2. Different surface types were investigated with an emphasis on fresh or refrozen leads since ice dynamics had rendered many original sampling site locations inaccessible for extended periods. For most of the deployment, surface temperatures inside and outside the chamber as well as snow depth and ice thickness were measured. Systematic blank measurements were also performed by putting the chamber on a Teflon sheet and burying the chamber slightly with snow. To facilitate a collaborative analysis of the results either sampling sites of the ICE, ECO and BGC teams were visited or the deployments were followed up by snow and ice sampling for later analysis for CH_4 and/or dissolved inorganic carbon (DIC) by the ECO and BGC teams. Finally, on 6 and 11 April measurements were done in parallel with the D. Nomura steady state flux chamber for direct comparison.

Tab. 3.5.2: *Deployment of the CO2/CH4 Flux Chamber.*

Date	Location	SH (cm)	Ice thick. (cm)	Lat (°N)	Lon (°E)
1 March	MetCity	-	> 20	88.22	31.40
5 March	Snow 2	12	> 20	88.10	30.51
7 March	Refrozen lead, behind runway	3	12	88.07	26.72
8 March	Dark site, FYI (snow and ice)	19	> 20	88.0	25.00
	Dark site, FYI (after removal of the snow)	0	> 20		
15 March	Refrozen lead between PS and MetCity	2	15	87.06	15.09
16 March	Refrozen, very active lead between PS and MetCity with patches of open water	-	11	86.90	12.84
18 March	New wide lead at the bow of PS passing MetCity	0	17	86.71	12.12
22 March	Dark site, FYI	-	> 20	86.23	15.68
27 March	Snow 2	-	> 20	85.83	13.38
6 April	Lead stern	5	31	84.53	14.35
10 April	Lead stern	3	12	84.38	14.62
11 April	Lead stern	1	57	84.32	14.74
15 April	Dark site, FYI	10	> 20	84.33	13.88

Tethered Balloon Measurements: A standard electrochemical ozone sonde was deployed with the tethered balloon on 20 days between 5 March and 6 May (Chapter 3.1). In all cases, the sonde was launched together with the AWI meteorological and the BAS aerosol package. Flight patterns included ascents to highest possible altitudes followed by observations for one to two hours at selected altitudes before descent or multiple ascents and descents during single launches. Launches were only possible on days with wind speeds below 8 m s^{-1} at the surface. The highest altitude reached with the balloon was above 1550 m.

Preliminary (expected) results

Trace Gas Concentrations: A preliminary analysis of the data for the period from 24 February to 20 April was performed. To put the results into context, the meteorological conditions are also briefly summarized (Figure 3.5.2.). During the analysed period wind speeds reached values up to 20 m s^{-1} during some storm events. Wind directions were predominantly from the North – Northwest sector bringing cold and dry Arctic air masses to the observational sites. However, between 13 and 20 April, easterly and southerly winds advected warmer and more humid air masses. Air temperatures at or slightly above 0 °C were observed on 19 April. Water temperatures were about -1.8 °C during most of the time, while warmer Atlantic water masses were encountered in April. The sun rose above the horizon for the first time around 12 March and was above the horizon 24 hours a day after 18 March.

Preliminary data for CO_2, CH_4, H_2O, and ozone concentrations are presented in Figure 3.5.3. CO_2, CH_4, and H_2O obtained on the bow tower and at Met City show very good agreement. Since the operation of the Met City flux system is not subject to an automatic wind sector control, these measurements are important to fill gaps in shipborne observations when the wind is out of the clean air sector. Observed spikes in the CO_2 time series highlight periods with wind directions bringing exhaust plumes from Kaptian Dranitsyn or Polarstern to Met City. This indicates that data obtained during the period with the Kapitan Dranitsyn parked next to Polarstern need to undergo careful screening for the potential impact of the ships' exhaust.

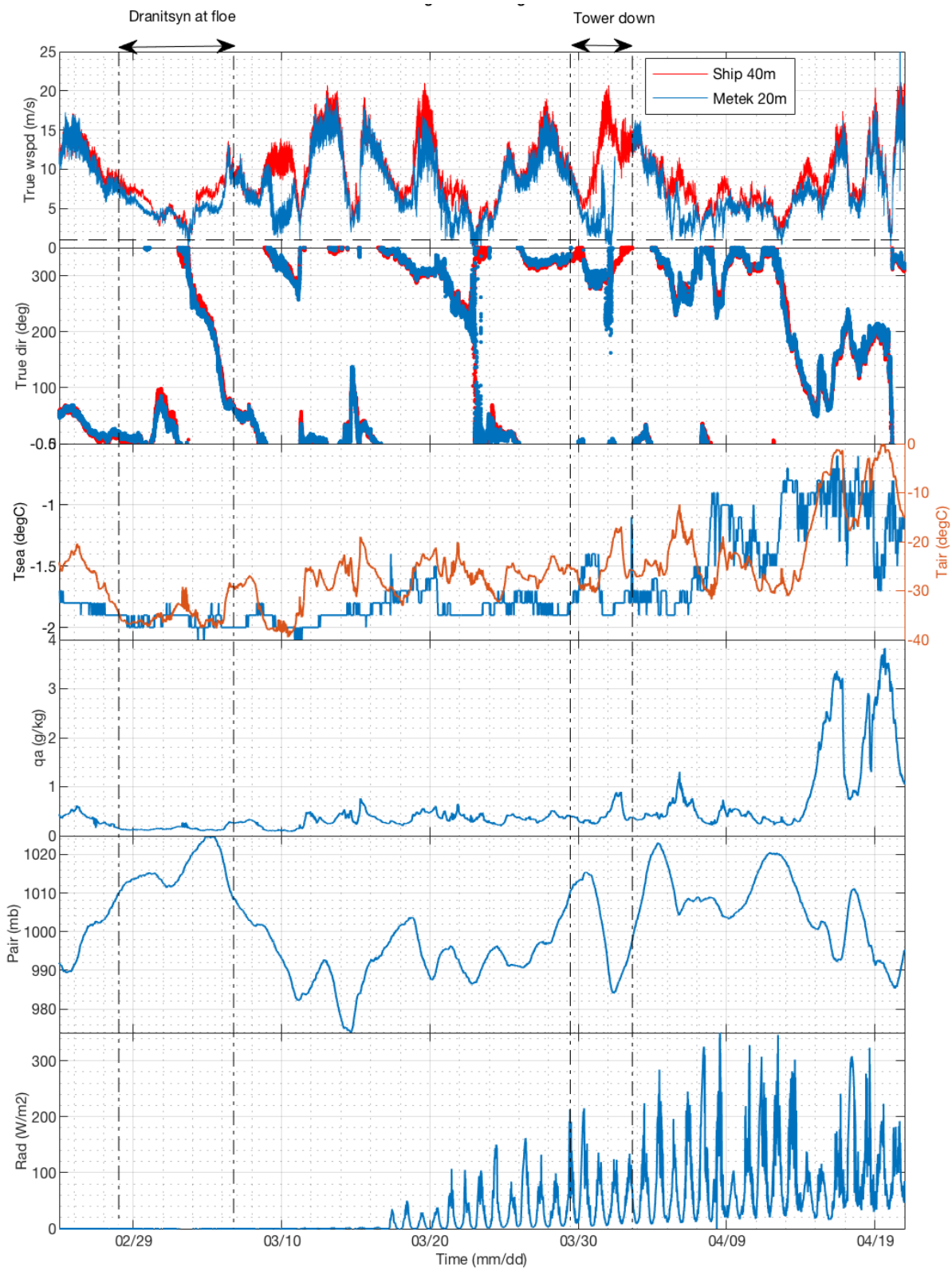

***Fig. 3.5.2**: Preliminary meteorological data from 24 February to 20 April. Panel 1: True wind speed from the bow tower (blue) and DSHIP (red). Panel 2: True wind direction from the bow tower (blue) and DSHIP (red). Panel 3: Sea water temperature at 5 m depth (blue) and air temperature at 29 m (red). Panel 4: Specific humidity. Panel 5: Pressure at sea level. Panel 6: Global radiation. All data in panels 3 to 6 from DSHIP.*

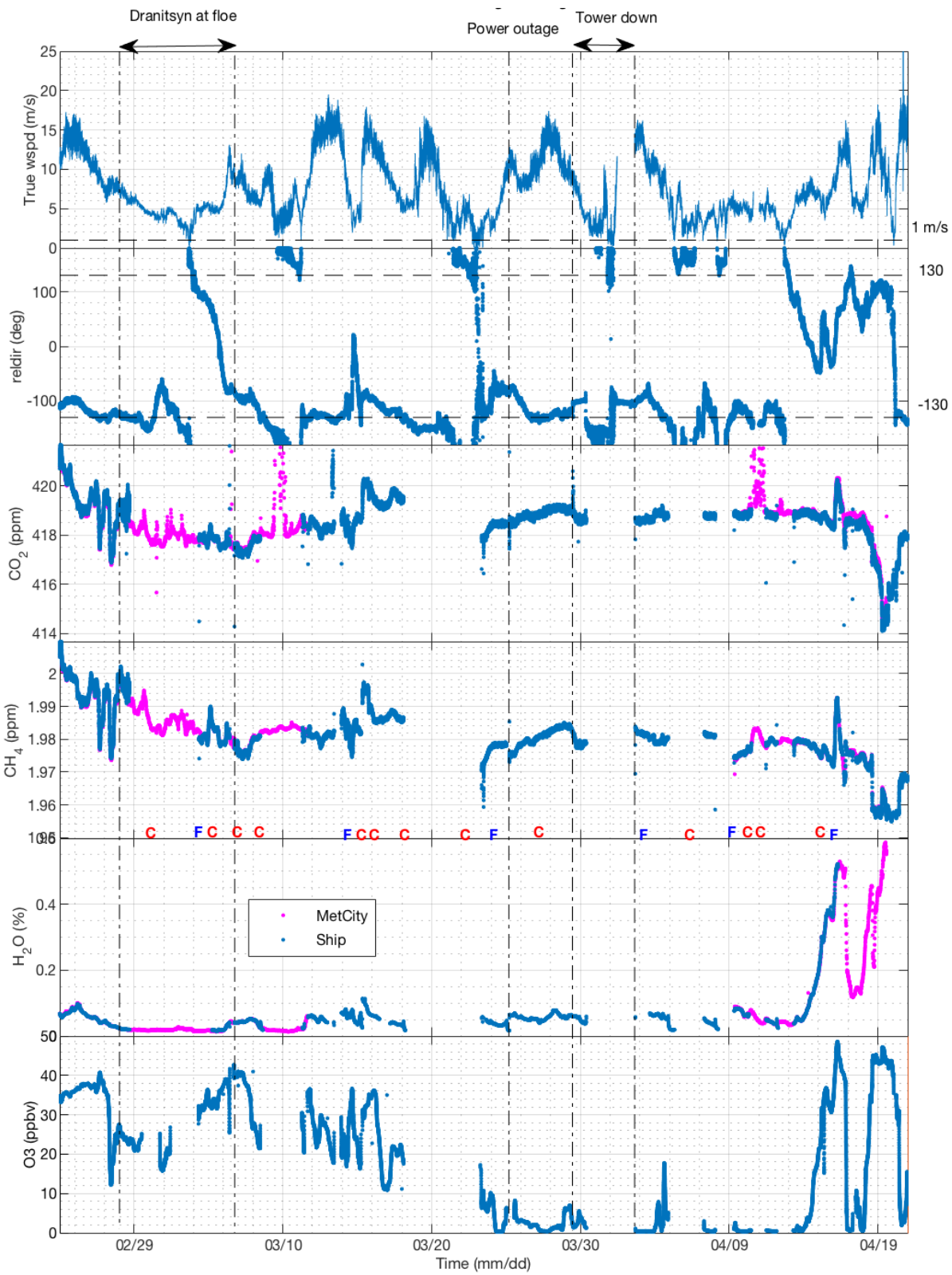

Fig. 3.5.3*: Preliminary data for trace gas concentration from 24 February to 20 April. Panel 1: True wind speed. Panel 2: Relative wind direction (0° = ship's heading, negative values = portside). Panel 3: CO_2 observed at the bow tower (blue) and at Met City (magenta). Panel 4: CH_4 observed at the bow tower (blue) and at Met City (magenta). Panel 5: Water vapor observed at the bow tower (blue) and at Met City (magenta). Panel 6: Ozone observed at the bow tower. Air samples collected with flasks (F) or the deployment of the CO2/CH4 dynamic flux chamber (C) are indicated in Panel 4.*

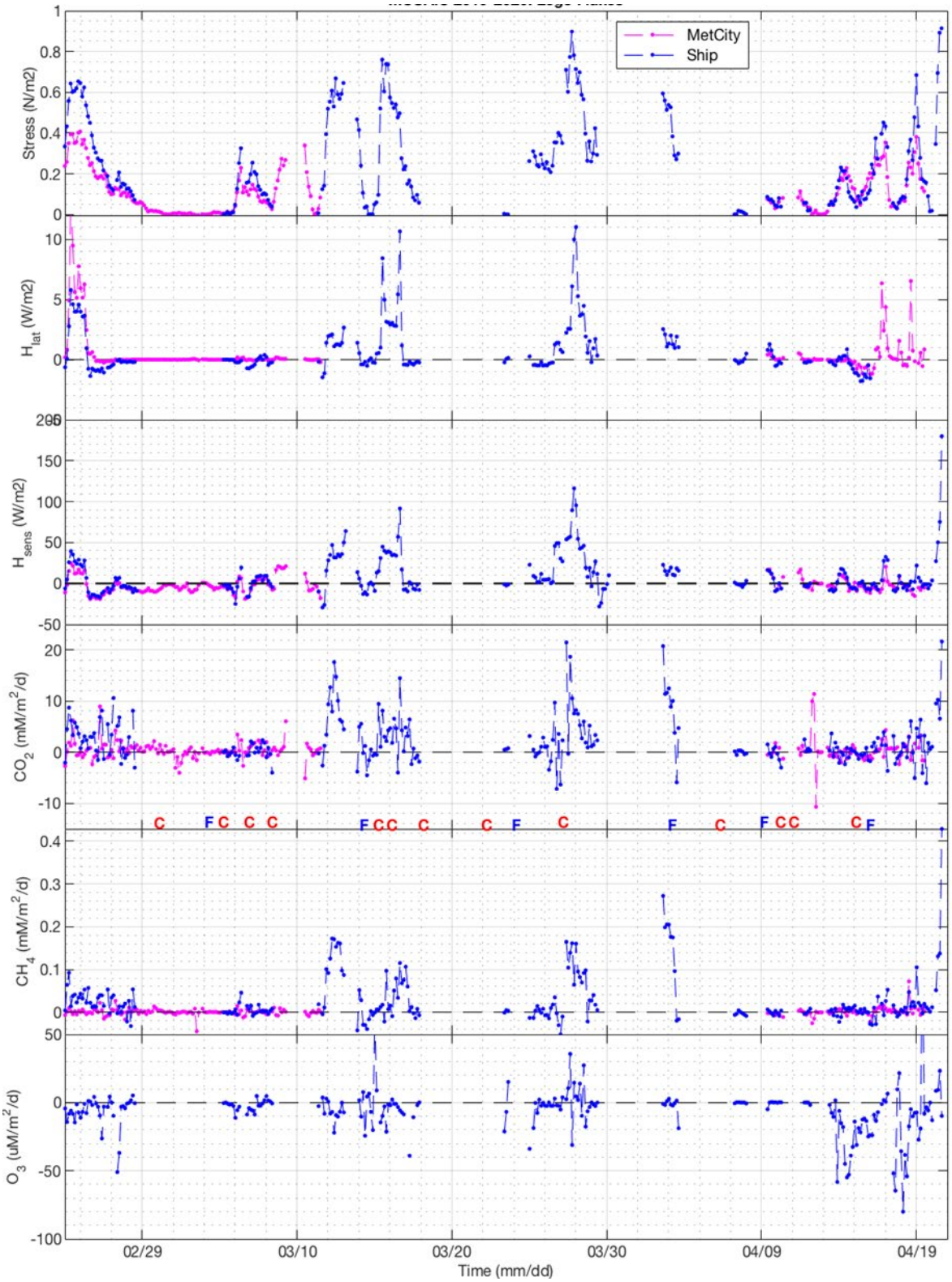

***Fig. 3.5.4**: Preliminary data for calculated fluxes for the period from 24 February to 20 April. Panel 1: Stress. Panel 2: Latent heat. Panel 3: Sensible heat. Panel 4: CO_2. Panel 5: CH_4. Panel 6: Ozone. Fluxes calculated with measurements at the bow tower (blue) and at Met City (magenta) are shown. Air samples collected with flasks (F) or the deployment of the CO2/CH4 dynamic flux chamber (C) are indicated in Panel 4.*

Although we encountered low ozone concentrations earlier (e.g. on 21 March it dropped the first time to zero), the ozone regime changed completely around 23 March. Since then until mid-April ozone dropped each day at least for a couple of hours to zero. During this period only short-term increases with values remaining mostly below 10 ppb were encountered and reaching values around 15 ppb only twice. On 14 April ozone started increasing and reached very high concentrations around 48 ppb on 16 April before slightly decreasing again. The high concentrations were related to warm air masses transported from the South with air temperatures well above -5 °C and relative humidity between 80 and 90 % due to a low located to the south of the ship's position. However, on the following days arctic air masses quickly led to decreasing ozone concentrations. Since we had during this period extended episodes with winds from the non-clean sector, our systems were regularly operating in back-flush mode. Fortunately, the data gaps can be filled by data from other groups like the ARM or the EPFL team. However, a further analysis will require a careful screening of such data to remove the potential impact of the exhaust from the ship.

Eddy-Covariance Fluxes: For the period from 24 February to 20 April preliminary 10-min fluxes were computed for the ship location and at Met City during favourable wind conditions. For the ship-borne measurements, we used the clean sector criteria, while Met City data during periods with wind directions from the ship were excluded. These criteria require further refinement taking into account for example flow distortion effects. A preliminary inlet attenuation correction was also applied, which will be further refined during the analysis. The temperature, humidity, and wind direction data from the ship was used whenever necessary, since bulk data from the Met City 10-m tower was not yet available.

3-hour averages of calculated fluxes are shown in Figure 3.5.4 illustrating the results from the bow tower and the Met City tower for stress, latent and sensible heat flux, as well as for CO_2, CH_4, and ozone. Positive values indicate upward fluxes, while negative values correspond to downward fluxes. Despite the different location and height, the fluxes are overall in reasonable agreement. The time series demonstrate that we were able to capture within our footprints the effect of the different surface properties on the observed fluxes. For example, important lead events occurred during the period from 12 to 16 March as well as on 27 March when a large lead was present at the ship's bow (Figure 3.5.5). During these periods, significant amounts of latent and sensible heat as well as CO_2 and CH_4 were released to the atmosphere.

As expected, ozone fluxes were in general very small. Further processing of the data is needed especially for the above described periods with low ozone concentrations. Nevertheless, important deposition of ozone occurred apparently after the advection of easterly and southerly air masses on 14 and 18 April, when large negative fluxes were calculated.

Fig. 3.5.5*: Lead under the ship's bow mast on 27 March.*

CO_2 / CH_4 Flux Chamber Measurements: The chamber directly affects the surface temperature inside the chamber. At low temperatures, the surface temperature inside the chamber increased by around 2 K during the deployment of 1.5 h compared to the undisturbed surface.

This is probably due to the cut-off of the outgoing longwave radiation by the chamber. As a result, water vapor in the chamber air was always higher compared to ambient air. This effect requires further assessment and needs to be accounted for in the final flux computation. The values presented here are not corrected for this effect.

Significant CO_2 fluxes were first observed on 15 March on a newly formed lead between the ship and Met City on a soft ice surface covered with drifted snow. A positive CO_2 flux of about 0.5 mM m^{-2} d^{-1} was determined with the flux chamber, while the flux observed with the eddy-correlation technique for the same time was about 8 mM m^{-2} d^{-1}. The CH_4 flux during the same deployment was very small with a value of -0.5 µM m^{-2} d^{-1}.

The measurements in parallel with the D. Nomura steady state flux chamber were done on a refrozen lead at the stern of the ship with a slushy layer (6 April) and with some frost flowers on top of a slush layer (11 April). On these surfaces the largest CO_2 fluxes were observed. For example, for the deployment on 11 April an upward CO2 flux on the order of +1.5 mM m^{-2} d^{-1} was derived (Figures 3.5.6).

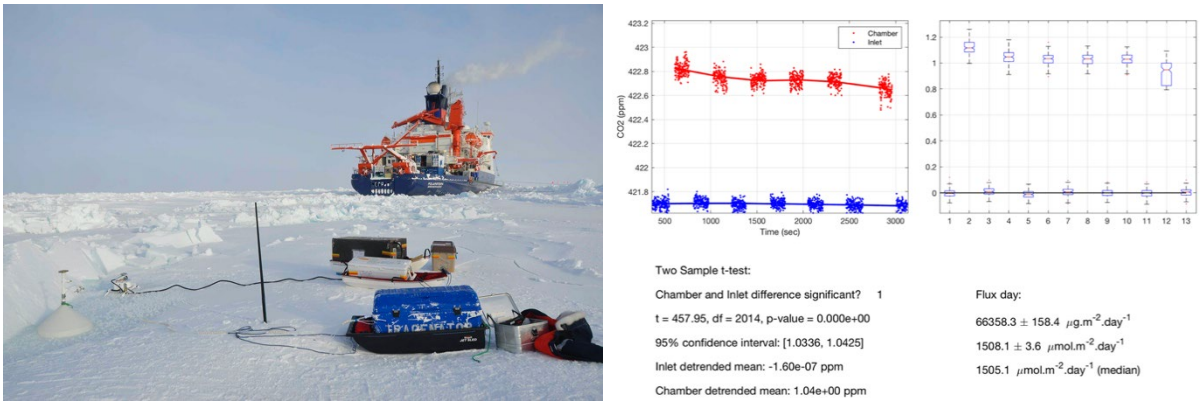

Fig. 3.5.6*: Left: Flux chamber measurements on the stern lead on 11 April. The CO2/CH4 dynamic flux chamber is in the foreground with the funnel and the blue box housing the instrumentation, while the chamber and boxes in the background belong to the static chamber by D. Nomura. Right: Loess fit applied to CO_2 concentrations measured in the inlet (blue) and chamber air (red) accounting for concentration trends (left) and detrended CO_2 concentrations with respect to the inlet air (right).*

Ozone Profiles: Ozone profiles were studied to determine the extent and the structure of layers with low ozone concentrations. The most important ozone-free layer observed with the tethered balloon extended from the ground to more than the maximum altitude of the balloon launch of more than 950 m altitude. This large extent of an ozone-free layer was confirmed by the regular ozone sondes launched on 03 and 07 April, which recorded ozone-free air up to altitudes of more than 1250 and 1150 m, respectively. Further interesting features in the ozone profiles concern persistent minima in ozone concentrations not only at the surface, but also at elevated layers as demonstrated in Figure 3.5.7, which shows the ozone profile observed on 24 March. Ozone was absent at the surface, but increased above 120 to 150 m altitude up to around 20 ppb. A second layer aloft with very low ozone concentrations at altitudes between 320 and 420 m was encountered before concentrations increase to background values of around 40 ppb at higher altitudes. A similar layered structure with overall higher ozone concentrations was recorded with the regular ozone sonde on the day before (Figure 3.5.7). Such a secondary layer with reduced ozone can be caused by either chemical processes taking place at this layer or the lifting of a layer with previously reduced ozone concentrations from the surface. In the following days, the secondary minimum in ozone in the layer aloft disappeared probably due to downward mixing of tropospheric air with background ozone concentrations (Figure 3.5.7).

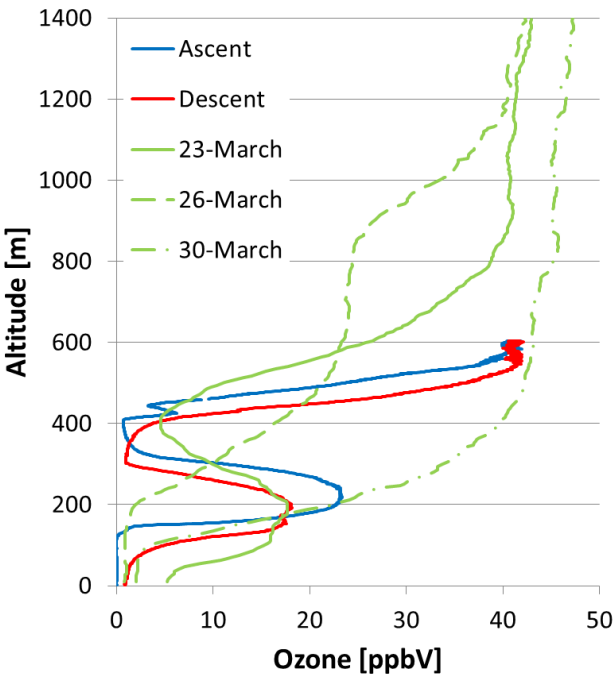

***Fig. 3.5.7**: Ozone profiles measured on 24 March during the ascent to an altitude of 600 m (blue) and the subsequent descent (red). Also shown are ozone profiles obtained with standard ozone sondes on 23, 26, and 30 March (see chapter 3.1).*

Data management

All data are handled, documented, archived and published following the MOSAiC data policy (see APPENDIX). Raw data from all these systems recorded until 21 May has been archived in the MOSAIC Central Storage (MCS) as detailed in the MOSAIC project data management plan. Data will be stored at the Arctic Data Centre following the agreement between ADC and the MOSAiC Project lead. DOIs will be communicated to PANGAEA for later access via the future MOSAiC Data Portal.

References

None

3.6. Measurement-Based Understanding of the Aerosol Budget in the Arctic and its Climate Effects - MBRACE

Julia Schmale[1], [1]CH.EPFL

(not on board:) Ivo Beck[1], Lauriane Quéléver[2], T. Jokinen[2], T. Laurila[2], Z. Brasseur[2], Mikko Sipilä[2] [2]FI.INAR

Objectives

Low-level clouds have an important effect on the surface energy budget in the Arctic[1-3]. Their lifecycles, warming and cooling effects over the central Arctic Ocean remain unclear, and models fail to correctly simulate them[4]. This shortcoming is partly due to insufficient information on cloud phase (liquid and/or ice crystals)[5]. Particularly liquid droplets modulate cloud radiative properties responsible for warming[6]. Droplets form on cloud condensation nuclei (CCN), a subset of aerosol particles. Aerosol particle concentrations over the central Arctic Ocean can be extremely low such that cloud properties are strongly influenced by CCN availability, and in extreme cases cloud formation is even inhibited[6]. Information on aerosol is scarce for all seasons in the high Arctic, but in particular for the cold and dark period when clouds have a pronounced warming effect[1]. To date, only information from land-based stations further south provide proxy information on central Arctic Ocean aerosols in winter.

Our guiding research questions are as follows:

- What are the contributions of natural versus anthropogenic sources to central Arctic Ocean CCN concentrations and how do they vary throughout the seasons (e.g. full sea ice cover in winter vs marginal ice zone in summer)?
- How important is growth of newly formed particles for the CCN budget?
- Which key natural processes are likely to change the CCN budget and control cloud properties with global warming (e.g., diminishing sea ice)?
- How strongly are liquid cloud radiative properties controlled by availability of CCN throughout the seasons?
- What are natural sources of aerosol in general and CCN in particular during polar night?

With our dataset, we will shed light on the contribution of anthropogenic emissions, which are not greenhouse gases, to Arctic warming through cloud formation, characterize for the first time aerosol-cloud interactions during Arctic winter, and help evaluate and improve models for better predictions of Arctic climate change and its far-reaching consequences.

Work at sea

We run the real-time, *in-situ* instrumentation in laboratory containers on C-Deck (position C10, EPFL-PSI container, and C9, BAS container) with state-of-the-art aerosol instrumentation (see Table 3.6.1), including high-resolution mass spectrometers, to study new particle formation (NPF), their growth, the chemical composition of the particles, and activation of particles to cloud droplets, amongst other. We operate the instrumentation behind a total inlet (GAW standard[7]) that captures particles and droplets, and an interstitial inlet, which captures only particles that are unable to form cloud droplets. New particle formation and growth are measured from a specifically designed NPF inlet. The mass spectrometer in the C9 container measures from a simple stainless steel inlet mounted through the roof (API-ToF inlet). See Figure 3.6.1 for an overview of inlets.

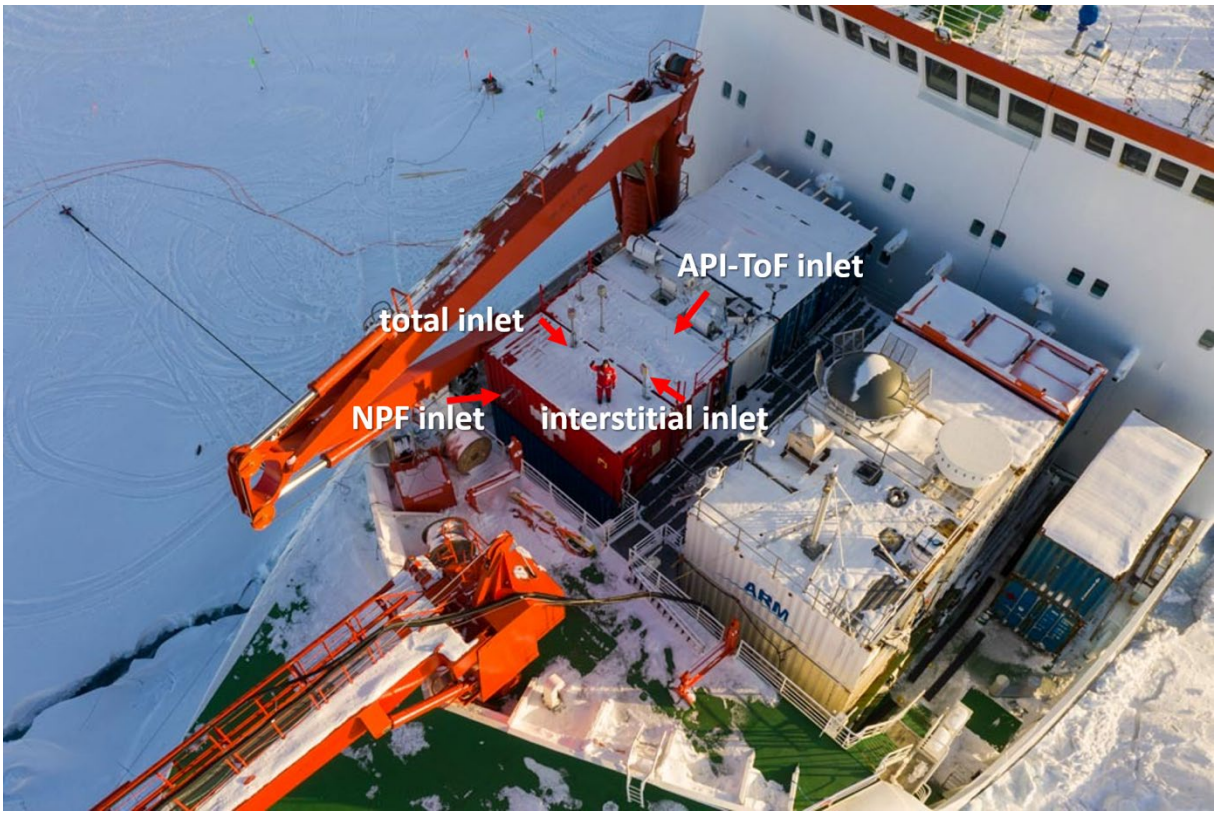

***Fig. 3.6.1**: Inlets on the EPFL-PSI and BAS containers.*

Real-time measurements are carried out by one person during each leg. The main tasks of the operator include: Guarantee high quality performance of the complex instrumentation, capturing natural and anthropogenic events that influence aerosol characteristics, and taking (or have taken by the ICE team) snow samples after fresh snowfall for subsequent on-shore laboratory analyses.

With a few exceptions, all instruments operated for the whole period. An overview of all instruments and their working periods is shown in Table 3.6.1. Smaller data gaps usually lasted less than one day and are not listed.

In addition, a number of mobile particle counters and filter samplers were deployed on the ice-pack in the ROV Hut, Balloon Town and at Met-City for a limited period of time.

***Tab. 3.6.1:** Instrumentation and operating periods*

ID	Instrument	Location - Inlet	Application	Samplig period
CPC 3776	Condensation particle counter	C10 – Total	Aerosol concentration of the total particle population > 3 nm	24.02. – 22.05.2020
CPC 3025	Condensation particle counter	C10 - Interstitial	Aerosol concentration of the interstitial particle population > 2.5 nm	24.02. – 22.05.2020
SMPS	Scanning mobility particle counter	C10 – Interstitial & Total	Size spectrum of aerosol population between 14.0746 - 685.39 nm (period 1), and 10.366 – 486.97 nm (period 2)	1: 24.02.2020 – 12.03.2020 2: 12.03.2020 - 22.05.2020
PSM A11-1 & A11-2	Particle size magnifier	C10 - NPF	Size distribution of the smallest aerosol particles from 1.5 to 3 nm	PSM A11 (scanning): 24.02. – 22.05.2020

			Two identical instruments are run in parallel for scanning and stepping mode	PSM A12 (stepping): 24.02. – 07.04.2020
NAIS	Neutral cluster and air ion spectrometer	C10 – NPF	Size distribution of both neutral and naturally charged ions and particles population for electrical mobility equivalent diameter ranging from 2 to 40 nm	24.02. – 22.05.2020
APS	Aerodynamic particle spectrometer	C10 - Total	Size distribution of the large aerosol population for aerodynamic diameters ranging from 0.5 to 20 µm	24.02. – 22.05.2020
CCNC	Cloud condensation nuclei counter	C10 – Interstitial & Total	CCN concentration at supersaturations of 0.15, 0.2, 0.3, 0.5, 1.0 %	24.02. – 11.05.2020
WIBS	Wideband Integrated Bioaerosol sensor	C10 - Total	Measurement of fluorescently active aerosol for biological speciation between 0.8 and 20 µm	24.02. – 22.05.2020
Aethalometer	Aethalometer	C10 – Interstitial & Total	Measurement of equivalent black carbon	24.02. – 22.05.2020
AMS	Aerosol mass spectrometer	C10 – Interstitial & Total	Size-resolved chemical composition of submicron aerosol particles (e.g. sulfate, nitrate, organic, ammonium, chloride, …)	29.02. – 20.05.2020
CI-APi-TOF	Nitrate-based chemical ionization atmospheric pressure interface time of flight mass spectrometer	C10 - NPF	Measurement of the chemical composition of gas-phase compound and highly oxidized molecules, precursors of aerosols (e.g. Sulfuric acid, iodic acid, …)	24.02. – 22.05.2020
APi-TOF	atmospheric pressure interface time of flight mass spectrometer	C9 – roof inlet	Measurement of the chemical composition of gas-phase naturally charged ions, precursors of aerosols (e.g. Sulfuric acid, ammonia clusters, …)	24.02. – 25.03.2020, 04.04. - 22.05.2020
O3	Ozone monitor	C10 - Interstitial	Ozone concentration	24.02. – 22.05.2020
SO2	SO2 monitor	C10 - Interstitial	Sulfur dioxide concentration	24.02. – 22.05.2020
SO2	SO2 monitor	C10 - Total	Sulfur dioxide concentration	02.03. – 22.05.2020
Picarro	Picarro Analyzer	C10 - Interstitial	Gas-phase concentration of Methane, Carbon monoxide, Carbon dioxide, water vapor	24.02. – 22.05.2020
RH / T 1 & 2	Temperature probe and hygrometer	C10 – Interstitial & Total	Relative Humidity and temperature sensor for both Interstitial and Total inlet	24.02. – 22.05.2020
V1	Valve switch	C10 – Interstitial & Total	Hourly bases inlet sample switch for AMS, CCNC, Aethalometer, SMPS	24.02. – 22.05.2020, intermittently not used

CPC 3022	Condensation Particle counter	C10 - Interstitial	Aerosol concentration of the total particle population > 7 nm	10.04. – 22.05.2020
CPC 3022	Condensation Particle counter	ROV Hut, C-10 interstitital	Aerosol concentration of the total particle population > 7 nm	ROV Hut: 05.04. – 20.04.2020, 22.04. – 10.05.2020 C-10 Interstitial: 11.05. – 13.05.2020
LOAC	Optical particle counter	Met-City, Balloon Town, C-10 total	Coarse mode aerosol detector	Met-City: 16.04. – 22.04.2020, Balloon Town: 24.04.2020 – 13.05.2020, C-10: 14.05. – 22.05.202
C3PO	Optical particle counter and aerosol filter sampler	Various places across the central observatory	Coarse aerosol size distribution, filter sampling for ice nucleating particle concentrations	23.03. – 13.05.2020 (see DShip Extraction)

***Tab. 3.6.2**: C3PO DShip Action Log*

Station - Device Operation	Date/ Time (Start)	Latitude (deg) (Start)	Longitude (deg) (Start)	Comment (Start)
PS122/3_33-7	23.03.2020 11:34	86.211408	15.810918	Deployed at lead 400 m from bow of vessel. Lead frozen over and covered with frost flowers and thick brine layer.
PS122/3_33-81	28.03.2020 13:47	85.574595	13.229647	Deployed at Met City
PS122/3_34-16	31.03.2020 06:50	85.32558	13.753212	Deployed at Met City
PS122/3_34-49	02.04.2020 13:50	84.932428	14.877112	Met City
PS122/3_34-50	03.04.2020 14:50	84.776739	13.321534	only OPC, 3 snow samples labeled with 03.04.2020 Met City open Lead, because there is an open lead
PS122/3_34-63	04.04.2020 14:40	84.64698	12.93467	Met-City, together with OPC
PS122/3_35-1	06.04.2020 07:27	84.542178	14.171671	BB8 and OPC2
PS122/3_35-50	08.04.2020 07:43	84.482959	14.62886	Met City
PS122/3_35-88	10.04.2020 12:40	84.377102	14.62132	Snow samples 10.04.2020 Met-City 1 snow in crack 10.04.2020 Met-City 3 blown snow
PS122/3_36-6	12.04.2020 11:47	84.291471	14.746283	OPC and TRAPS
PS122/3_36-16	14.04.2020 08:22	84.331342	14.806397	
PS122/3_36-58	16.04.2020 08:22	84.316839	13.131692	
PS122/3_36-117	18.04.2020 08:22	84.455396	13.821432	
PS122/3_37-1	20.04.2020 08:30	84.56703	14.617241	Droneville, Stormy, just first filter spot

PS122/3_37-55	22.04.2020 12:22	84.118602	15.947415	OPC2 and BB8
PS122/3_37-111	24.04.2020 11:20	84.054361	15.90658	BB8 and OPC-2
PS122/3_37-121	26.04.2020 13:40	83.922258	15.506554	OPC 2 and BB8
PS122/3_38-30	28.04.2020 12:00	84.036283	16.510422	BB8 and OPC 2, BB8 did not commumicate via bluetooth so only measurements in one spot, rest could be used as blank
PS122/3_38-68	30.04.2020 15:00	83.926884	17.52028	BB8 and OPC 2
PS122/3_38-89	02.05.2020 13:40	83.900395	17.569746	BB8 and OPC2, plus 2 snow samples
PS122/3_39-60	04.05.2020 13:40	83.909875	18.354323	BB8 and OPC2
PS122/3_39-59	06.05.2020 11:23	83.919876	17.68977	BB8 and OPC 2
PS122/3_39-97	08.05.2020 14:40	83.844801	15.032657	only BB8, forming of a ridge and crack in sampling spot.
PS122/3_40-6	12.05.2020 08:50	83.420362	12.82195	BB8 and OPC 2, got caught in a ridging event when the floe broke to pieces, all retrieved

Expected and preliminary results

We collected a continuous dataset during Leg 3. It includes data of very clean atmospheric conditions as well as data of contaminated air. Contamination was mainly caused by the ship's exhaust due to the predominant wind direction from north-east, sometimes also by the use of the Pistenbully and skidoos. About 20 % of the time, the wind direction was favourable (-70 to 70 degree from the bow). Figure 3.6.2 shows the cumulative probability of the particle number concentration between 24 February and 20 May measured behind the total inlet by a condensation particle counter. Clean conditions are represented by values < 200 particles / cm3. The fraction of not pollution influenced measurements is about 20 %, consistent with the wind direction. Specific tracers from the chemical measurements as well as coarse mode aerosol can partly be used for analysis also during exhaust-influenced periods. The highest (clean) number concentration was recorded on 13 May with 1413 p/cc (10 seconds average), the second highest on 16 April with 1075 p/cc during a warm air mass intrusion. The lowest number was recorded on 16 May just before departure of the floe with 1.45 p/cc due to fog scavenging the particles.

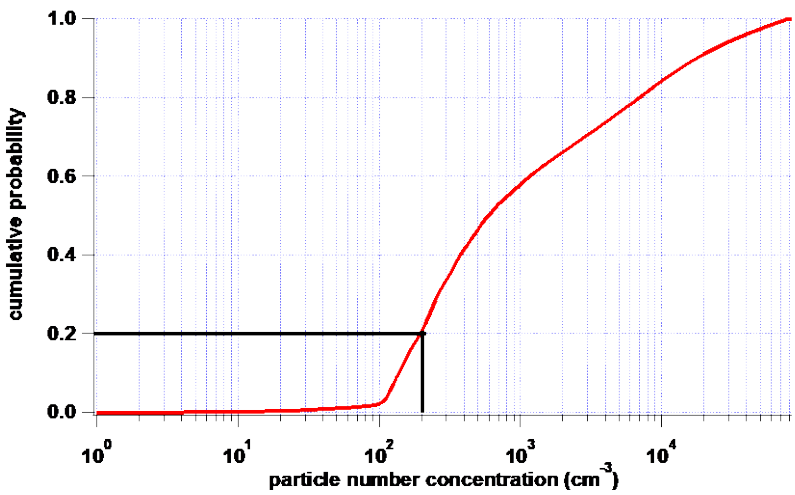

Fig. 3.6.2: Cumulative probability of the particle number concentration.

Generally, March was characterized by high wind speeds and a number of storms, while winds were calmer in April and May. For aerosol production, storms are important as they volatilize snowflakes and sea spray in case of open leads. Figure 3.6.3 show the coarse mode aerosol number concentration and the true wind speed. While in April the correlation between number concentration and wind speed is obvious, it is less evident later during the leg. This is likely due to the wetter snow which is more difficult to lift into the air.

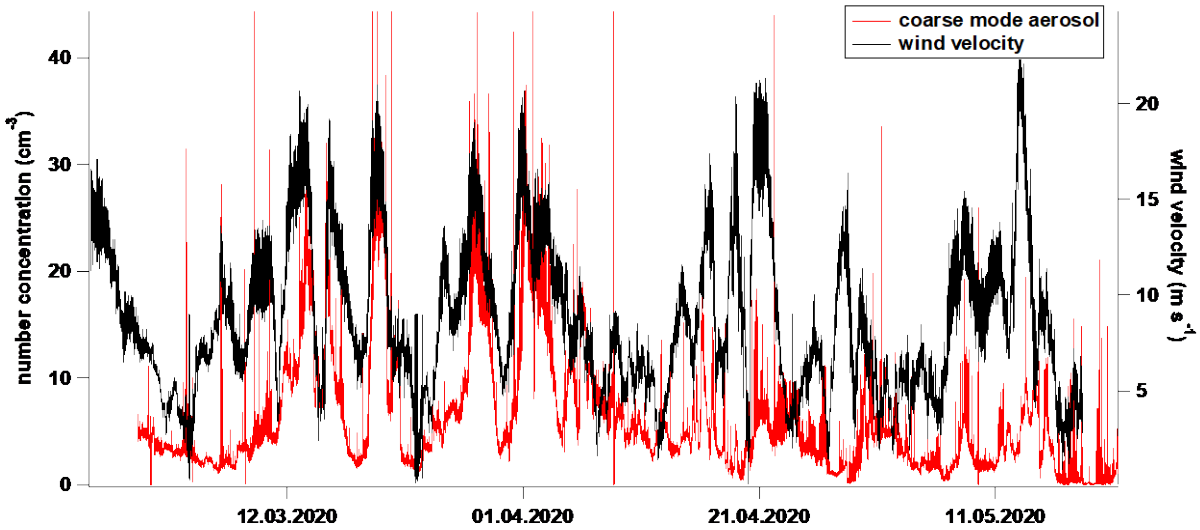

Fig. 3.6.3: *Coarse mode aerosol number concentration derived from the APS and ship-based wind velocity.*

The size distribution of particles mostly featured a pronounced accumulation mode with a mode diameter between 150 and 200 nm. Only on rare occasions Aitken mode or even nucleation mode particles were observed. Those were generally associated with southerly air masses (see Figure 3.6.4).

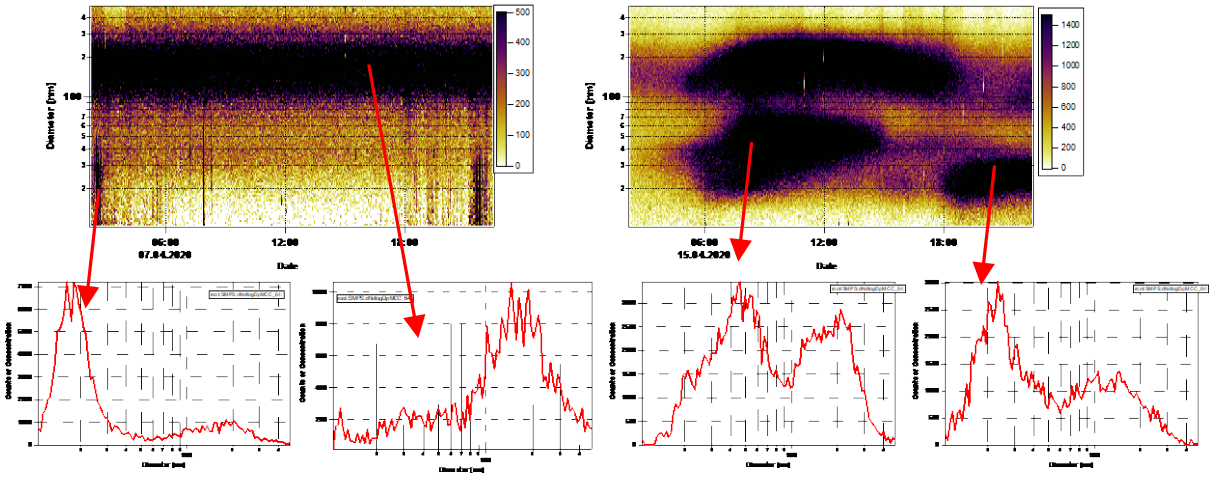

Fig. 3.6.4: *Comparison of microphysical aerosol properties of northerly air masses (7 April) and southerly air masses (15 April).*

In terms of atmospheric chemistry observations, the composition of the aerosol population was dominated by particulate sulfate and organics, which need to be further analised for their specific composition. Several warm air mass intrusions from the South brought variable organic aerosol composition, including traces of methanesulfonic acid. Northerly air masses

were characterized by the presence of particulate and gas phase halogenated compounds such as bromine and iodic acid. Figure 3.6.5 provides an example of the different particulate chemical compositions by air mass.

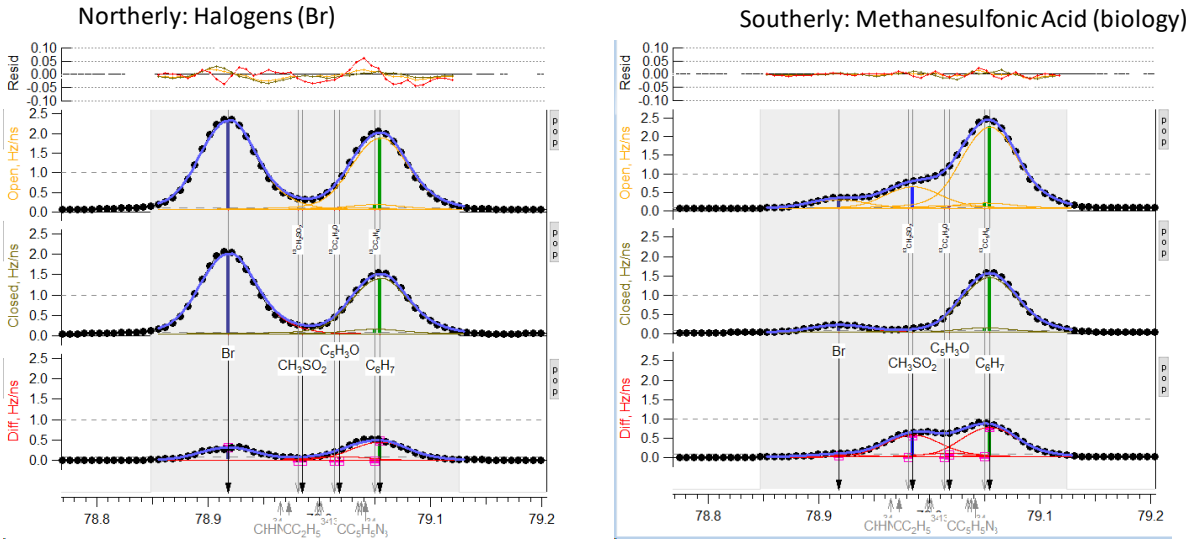

Fig. 3.6.5: *Characteristic trace species of northerly air mass aerosol (7 April, left, Br-) and southerly air mass aerosol (15 April, right, CH3SO2).*

Fog conditions only occurred towards the very end of the leg, hence *in-situ* observations of particle activation in fog could only be studied to a minor extent. More occasions are typically expected for the summer season, hence legs 4 and 5.

Data Management

All data are handled, documented, archived and published following the MOSAiC data policy (see APPENDIX). All instruments are registered in DShip as continuously recording instruments. All raw data are stored on the MCS. Raw data analyses will happen at the institutions involved and intermediate data products will be stored on the servers of the University of Helsinki and École Polytechnique Fédérale the Lausanne. Final data will be stored at the PANGAEA data repository (World Data Center PANGAEA Data Publisher for Earth & Environmental Science www.pangaea.de). All data are handled, documented, archived and published following the MOSAiC data policy.

References

Lubin, D. & Vogelmann, A. M. A climatologically significant aerosol longwave indirect effect in the Arctic. Nature 439, 453, doi:10.1038/nature04449 (2006).

Shupe, M. D. & Intrieri, J. M. Cloud Radiative Forcing of the Arctic Surface: The Influence of Cloud Properties, Surface Albedo, and Solar Zenith Angle. Journal of Climate 17, 616-628, doi:10.1175/1520-0442(2004)017<0616:crfota>2.0.co;2 (2004).

Curry, J. A. & Ebert, E. E. Annual Cycle of Radiation Fluxes over the Arctic Ocean: Sensitivity to Cloud Optical Properties. Journal of Climate 5, 1267-1280, doi:10.1175/1520-0442(1992)005<1267:acorfo>2.0.co;2 (1992).

Tjernstrom, M., Sedlar, J. & Shupe, M. How well do regional climate models reproduce radiation and clouds in the Arctic? An evaluation of ARCMIP simulations. J. App. Met. Clim. 47, 2405-2422, doi:10.1175/2008JAMC1845.1 (2008).

Morrison, H. et al. Resilience of persistent Arctic mixed-phase clouds. Nature Geosci 5, 11-17 (2012).

Mauritsen, T. et al. An Arctic CCN-limited cloud-aerosol regime. Atmos. Chem. Phys. 11, 165-173, doi:10.5194/acp-11-165-2011 (2011).

Schmale, J. et al. Overview of the Antarctic Circumnavigation Expedition: Study of Preindustrial-like Aerosols and Their Climate Effects (ACE-SPACE). Bull. Amer. Meteorol. Soc. 100, 2260-2283, doi:10.1175/BAMS-D-18-0187.1 (2019).

3.7 Sea Salt Aerosol above Arctic Sea Ice – Sources, Processes and Climate Impacts (SSAASI-CLIM)

M. Frey[1], [1]UK.BAS
(not on board:) A. Kirchgässner[1], T. Lachlan-Cope[1], X. Yang[1], A. E. Jones[1], L. Clarke[2] [2]UK.MMU

Grant-No. NE/S00257X/1

Objectives

Sea salt aerosol (SSA) influences regional climate directly through scattering of radiation or indirectly via its role as a cloud-forming particle. While it is well known that SSA can be cloud condensation nuclei (CCN) forming cloud droplets, it has been shown only recently that SSA can be also a source of ice nucleating particles (INP) forming ice crystals (DeMott et al., 2016), depending on its chemical composition and surface shape. Aerosol processes and interactions with clouds are very complex (Browse et al., 2014) and Arctic clouds are poorly represented in climate models, which is partly due to a lack of understanding of source and nucleating capability of natural aerosol in the high Arctic. Aerosol models for example do currently not capture aerosol maxima in the Arctic winter/spring observed at high latitudes (e.g. Huang et al., 2017). A recent Antarctic sea ice cruise provided first direct evidence of a source of SSA from salty blowing snow (BSn) above sea ice (Frey et al., 2019), which had been hypothesized previously (Yang et al., 2008): during storms salty snow gets lofted into the air and then undergoes sublimation to generate SSA. Additional but minor SSA sea ice sources are frost flowers and open leads. Taking into account the blowing snow source of SSA improves model

predictions significantly (Yang et al., 2019; Huang et al., 2017). However, the impact on radiation and clouds of SSA from this new sea ice source is not known. And a quantitative understanding of natural aerosol processes and climate interactions is needed to provide a baseline against which to assess anthropogenic pollution reaching the Arctic and evaluate the success of mitigation measures (e.g. AMAP 2015).

This project seeks to determine the SSA source strength, fate and potential impact on Arctic climate associated with blowing snow above sea ice and other sea ice sources. A particular focus is on quantifying the contribution of ice nucleating particles (INP) from sources related to Arctic snow and sea ice. Participation in the year-long Multidisciplinary drifting Observatory for the Study of Arctic Climate (MOSAiC) provides the unique opportunity to observe key aerosol processes and properties in the central Arctic ocean throughout all seasons of the year.

The first objective is to quantify SSA variability above sea ice and relative contributions from local sources (blowing snow, frost flowers and open leads) throughout the year. This will be achieved through (a) *in-situ* measurements of particle size distribution and concentration, covering all relevant sizes ranging from the sub-micron scale to the scale of airborne snow particles at various levels within the atmospheric boundary layer and in the free troposphere using a tethered balloon platform. And (b) through chemically fingerprinting the local snow and sea ice source using major ion ratios and sulfur isotopes, and compare these to the chemical composition of aerosol to constrain its contribution to Arctic SSA.

The second objective is to quantify the contribution of SSA above sea ice to cloud forming particles. This will be achieved through (a) measurement of ice nucleating particles (INP) in the air above the sea ice to evaluate their variability associated with SSA concentrations and events (blowing snow, opening of leads). And (b) through testing for the presence of INP in snow on sea ice, brine, frost flowers and link to ambient INP.

The third objective is to determine the climate sensitivity to SSA from the sea ice source (blowing snow, frost flowers, open leads) in the Arctic through numerical modelling based on existing and new MOSAiC observations. This will be achieved through (a) quantification of the direct radiative effect of SSA and (b) quantification of the indirect radiative effect of SSA via its contributions to INP/CCN and their impact on cloud fraction.

Work at sea

Measurements on-board Polarstern and on the sea ice during PS122-3 included particle size and concentration (sub-micron to snow/cloud particle size), online-INP concentrations, and aerosol filter sampling for later offline-analysis of a range of particle chemical properties and INP concentrations. Tethered balloon launches were carried out to gather information on the fate of particles formed near the sea ice surface as they get lofted to heights where clouds may form. Instruments were deployed on the AWI tethered balloon to probe the lower atmosphere up to a height of 1500m (chapter 3.1). During a total of 20 launch days 30 vertical profiles were achieved (chapter 3.1). Sampling of snow on sea ice, brine, frost flowers and blowing snow was carried out up to 3 times per week to constrain the local source of aerosol and INPs. Sample collection on the sea ice was supported by team ICE (chapter 4). An overview of all measurement activities is presented in Table 3.7.1.

Tab. 3.7.1 *Overview of parameters observed during PS122-3*

Instrument	Parameter	Location	Sampling Period
Spectrometer for Ice Nuclei (SPIN)	INP concentration (size range 0.8-20.0 µm); 1-min resolution	TSP inlet - BAS Container	21 days during 01.04.-23.05.
Optical Particle Counter (GRIMM / ALPHASense)	Aerosol size & concentration (size range 0.3-31.0 µm); 1-min resolution	TSP inlet - BAS Container	10.04.-22.05. (GRIMM down since 15.02.)

High volume filter sampler	Offline analysis - aerosol chemical composition, INP, $^{34}S(SO_4^{2-})$, SEM-SPA; 2-7 day resolution	PM2.5 inlet - BAS Container	24.02.-22.05.
Low volume filter sampler	Offline analysis - aerosol chemical composition (major ions, Br^-), INP; 2 day resolution	TSP inlet - BAS Container	24.02.-22.05.; instrument down 19.04.-07.05.
Low volume filter sampler[1)]	Offline analysis – marine sugars; 7 day resolution	BAS Container	24.02.-22.05.
APi-TOF[2)]	H_2SO_4, NH_3 and clusters, naturally charged ions; 1-min resolution	BAS Container	24.02.-22.05.
Cloud Aerosol Spectrometer (CAPS-CAS)	particle size & concentration (size range 0.51-50.0 µm); 1-min resolution	Crows Nest	18.04.-22.05.
Cloud Imaging Probe (CAPS-CIP)	particle size, shape & concentration (size range 12.5-1550.0 µm); 1-min resolution	Crows Nest	18.04.-22.05. (intermittent operation)
Low volume filter sampler	Offline analysis - aerosol chemical composition (major ions, Br^-), INP; 20 launches	AWI tethered balloon	24.02.-22.05.
Optical Particle Counter (ALPHASense)	Aerosol size & concentration (size range 0.4-40.0 µm); 30 launches	AWI tethered balloon	24.02.-22.05.
Optical Particle Counter (CLASP)	Aerosol size, concentration & flux (size range 0.3-12.0 µm); 1-min resolution	MetCity - 12m-flux tower (at 3m)	24.02.-22.05.
Snow Particle Counter (SPC)	Snow particle size & concentration (size range 50-500 µm); 1-min resolution	MetCity - 12m-flux tower (at 0.1m and 10m)	24.02.-22.05.
Snow Sampling (sampler, rocket traps)	Offline analysis - chemical composition, INP, $^{34}S(SO_4^{2-})$ of (blowing) snow, brine, frost flowers, ice; > weekly resolution	MOSAiC ice floe	24.02.-22.05.

[1)]TROPOS project; [2)]EPFL / INAR project (chapter 3.6)

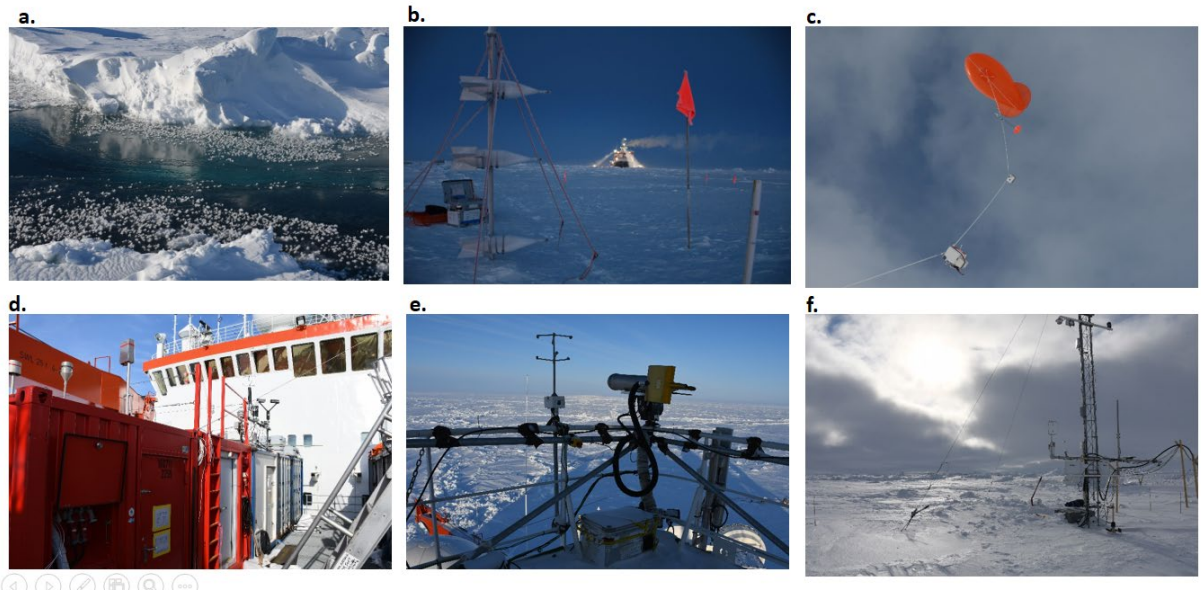

Fig. 3.7.1 *Observational approach to investigate sources, processes and potential impact on clouds of sea salt aerosol above sea ice: a. sampling of the sea ice surface (snow, brine, sea ice) and b. airborne snow, c. vertical profiling of the lower atmosphere up to 1.5km height, continuous measurements of aerosol, snow and cloud particles d. from the ship's bow, e. from the crows nest, and f. in situ on the ice floe from the flux tower at MetCity.*

Preliminary (expected) results

The expected year-round datasets of SSA and INP above sea ice, as well as chemical source signature of snow and sea ice from the Central Arctic Ocean will provide important insights into Arctic sea ice as a particle source. They will lead to improved model parameterisations of

the SSA blowing snow source as a function of sea ice properties, as well as a better understanding of the potential impact on Arctic clouds. And finally, SSA is also a potential sea ice proxy measured in polar ice cores (Abram, et al., 2013) and quantifying the SSA sea ice source will constrain reconstructions of past Arctic sea ice conditions (e.g. Rhodes et al., 2017). The PS122-3 observational period covered a wide range of environmental conditions with the transition from polar night to polar day, the onset of surface melt, and was marked by frequent storms, a very dynamic ice cover with frequent lead openings and ridging, and the influence of both Northerly and Southerly air masses.

Examples of data collected include snow particles above the sea ice: drifting or blowing snow is observed above a drift wind speed threshold, which depends to a first order on temperature (Figure 3.7.1). Blowing snow has been previously observed to be a significant source of sea salt aerosol in winter/ spring above sea ice (e.g. Frey et al., 2019), which needs to be taken into account in the characterisation of the regional aerosol budget.

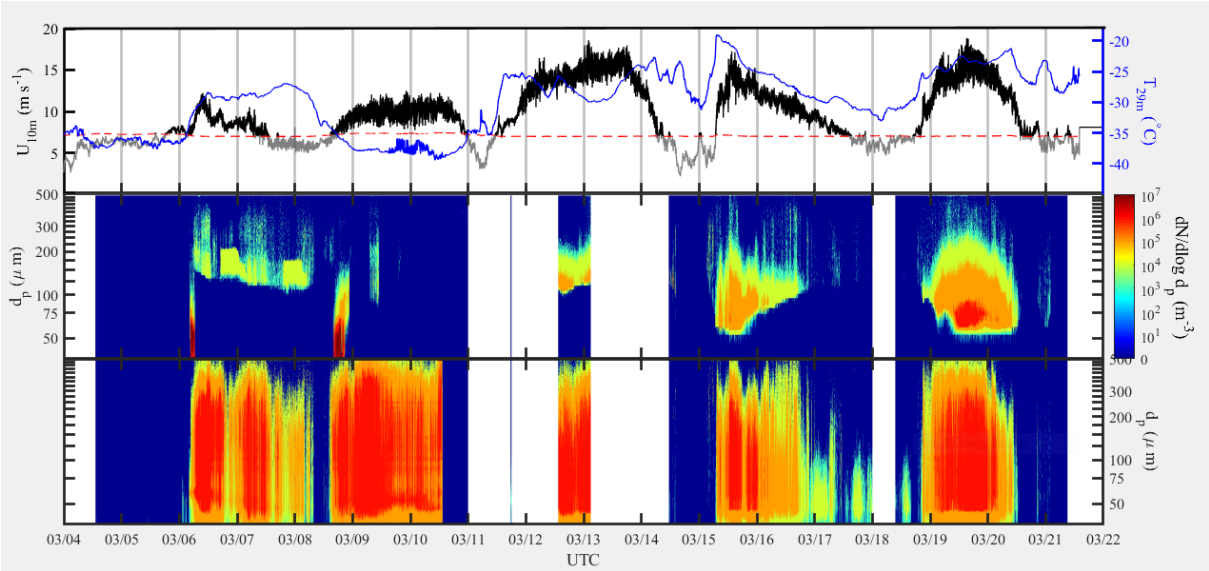

Fig. 3.7.2 *Snow particle concentrations and size distribution observed at MetCity at 0.05m (b) and at 10m (c). Drift onset is observed once the wind speed exceeds the drift threshold (red dashed line in a), which can be estimated to a first order based on temperature.*

Online measurements of INP with the Spectrometer for Ice Nuclei (SPIN, DMT) were carried out for the first time North of 84°N during spring above Arctic sea ice. As an example, observations during the record storm on 13 May indicate that several 10s of particles/cm^3 are present that may activate ice clouds in the -15 to -20°C temperature range at supersaturation above ice of SS_{ice} ~30% (Figure 3.7.2), consistent with the occurrence of low-level mixed phase clouds.

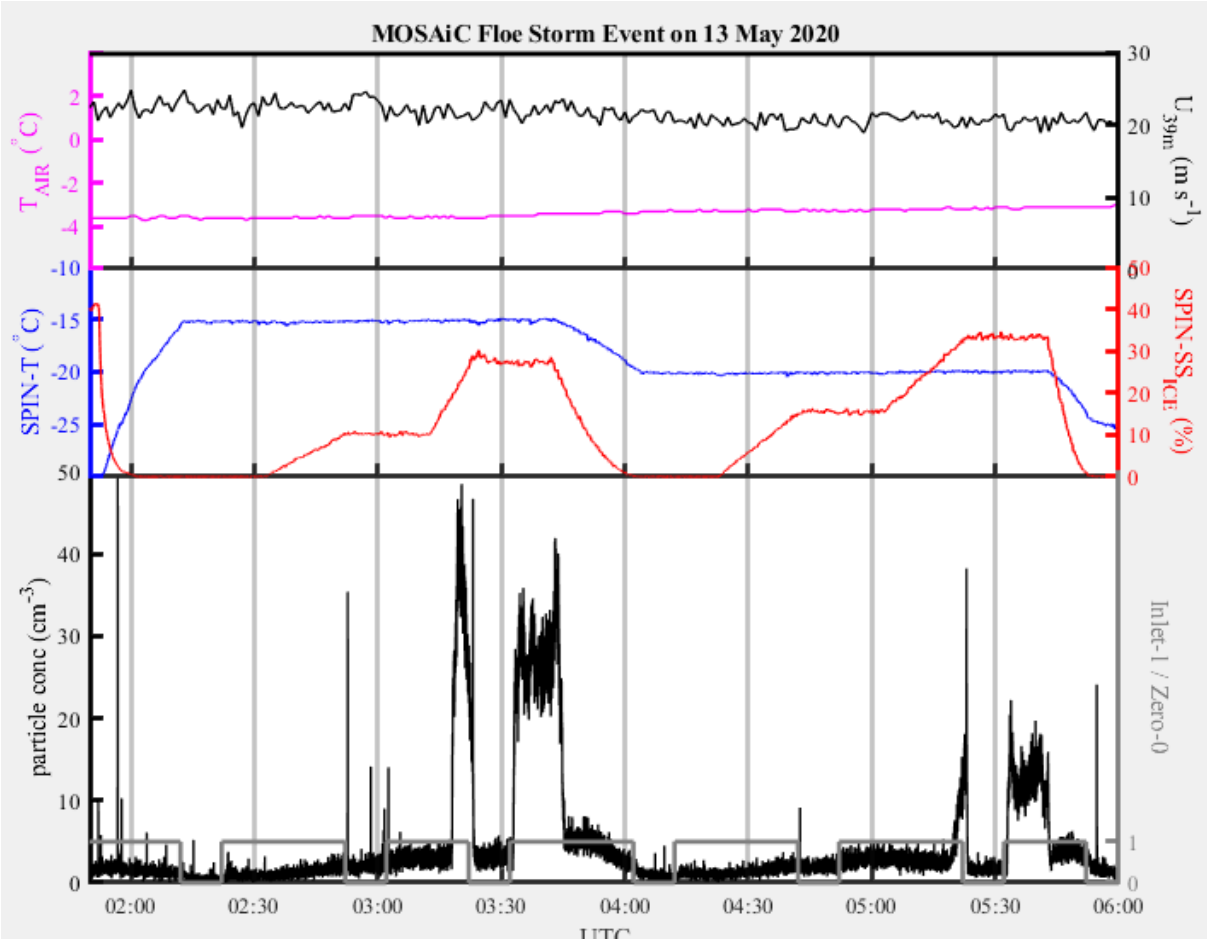

Fig. 3.7.3 *SPIN measurements of potential ice nucleating particles (INP) above the sea ice during a storm on 13 May 2020. Shown are ambient temperature and wind speed (top panel), instrument chamber temperature and super saturation above ice (SS_{ice}) (mid panel), as well as total measured particle concentrations detected during zero and ambient air intervals (bottom panel).*

Data management

All data are handled, documented, archived and published following the MOSAiC data policy (see APPENDIX). Online measurements will be available during or very soon after completion of the MOSAiC cruise in 2020, whereas data from the off-line chemical analysis of aerosol filter, snow and ice samples will become available after completion of lab analysis in the UK by mid 2021. All SSAASI-CLIM data will be archived at the British Polar Data Centre and made available within the MOSAiC data management framework. In particular DOIs will be communicated to PANGAEA for later access via the future MOSAiC Data Portal.

References

Abram, NJ, Wolff, EW, and Curran, MA (2013) A review of sea ice proxy information from polar ice cores, Quaternary Science Reviews, 79, 168 – 183, doi:10.1016/j.quascirev.2013.01.011.

AMAP Assessment 2015, Arctic Monitoring and Assessment Programme, vii + 116 pp..

Browse J, Carslaw KS, Mann GW, Birch CE, Arnold SR, and Leck C (2014) The complex response of Arctic aerosol to sea-ice retreat, Atmospheric Chemistry and Physics, 14, 7543–7557, doi:10.5194/acp-14-7543-2014.

DeMott PJ, Hill TCJ, McCluskey CS, Prather KA, Collins DB, Sullivan RC, Ruppel MJ, Mason RH, Irish VE, Lee T, Hwang CY, Rhee TS, Snider JR, McMeeking GR, Dhaniyala S, Lewis ER, Wentzell JJB, Abbatt J, Lee C, Sultana CM, Ault AP, Axson JL, Diaz Martinez M, Venero I, Santos-Figueroa G, Stokes MD, Deane GB, Mayol-Bracero OL, Grassian VH, Bertram TH, Bertram AK, Moffett BF, and Franc GD (2016) Sea spray aerosol as a unique source of ice nucleating particles, Proceedings of the National Academy of Sciences, 113, 5797–5803, doi:10.1073/pnas.1514034112.

Frey MM, Norris SJ, Brooks IM, Anderson PS, Nishimura K, Yang X, Jones AE, Nerentorp Mastromonaco MG, Jones DH, and Wolff EW (2019) First direct observation of sea salt aerosol production from blowing snow above sea ice, Atmospheric Chemistry and Physics Discussions, doi:10.5194/acp-2019-259.

Huang J and Jaeglé L (2017) Wintertime enhancements of sea salt aerosol in polar regions consistent with a sea ice source from blowing snow, Atmospheric Chemistry and Physics, 17, 3699–3712, doi:acp-17-3699-2017.

Rhodes RH, Yang X, Wolff EW, Mc- Connell JR, and Frey MM (2017) Sea ice as a source of sea salt aerosol to Greenland ice cores: a model-based study, Atmospheric Chemistry and Physics, 17, 9417–9433, doi:10.5194/acp-17-9417-2017.

Yang X, Frey MM, Rhodes RH, Norris SJ, Brooks IM, Anderson PS, Nishimura K, Jones AE, and Wolff EW (2019) Sea salt aerosol production via sublimating wind-blown saline snow particles over sea ice: parameterizations and relevant microphysical mechanisms, Atmospheric Chemistry and Physics, 19, 8407–8424, doi:10.5194/acp-19-8407-2019.

Yang X, Pyle JA., and Cox RA (2008) Sea salt aerosol production and bromine release: Role of snow on sea ice, Geophysical Research Letters, 35, doi:1029/2008GL034536.

3.8 Observations of Arctic Atmospheric Boundary Layer with small unmanned Aerial Vehicles

Gina Jozef[1], John Cassano[1], Julia Schmale[3], Andreas Preußer[4]

(not on board:) Gijs de Boer[1,2], Dale Lawrence[1], Brian Argrow[1], Jonathan Hamilton[1], Radiance Calmer[1], Steven Borenstein[1], Abhiram Doddi[1], Michael Rhodes[1]

[1]US.CU
[2]US.NOAA
[3]CH.EPFL
[4]DE.UTrier

Objectives

Transfer of energy between the Earth's surface and the overlying atmosphere, particularly at high latitudes, remains an area of substantial uncertainty in our understanding of the global climate system. The consequences of this uncertainty are significant, with global climate model projections of present-day sea ice demonstrated to fall short of simulating observed rates of change. The thermodynamic structure of the lower atmosphere plays a central role in regulating processes driving this energy transfer, including cloud structure and radiative influence, and turbulent energy exchange. Significant insight can be gained by measurements focused on the structure of the lower atmosphere, its spatial variability, the intensity of turbulent energy fluxes, and the influence of surface features on this structure, over the central Arctic Ocean ice pack. Of specific interest are the impacts of leads on turbulent fluxes in the boundary layer atmosphere. To provide such measurements, unmanned aircraft-based observations of the lower atmosphere are being made during legs 3 and 4 (March through August) of MOSAiC under funding from the National Science Foundation (award OPP 1805569, de Boer, PI). In conjunction with other MOSAiC datasets, these measurements will provide unprecedented perspectives on lower atmospheric state and its influence on the surface energy budget. Results from this work will be disseminated to various audiences, and measurements will be used to evaluate and improve various modelling tools.

Work on the ice

Data gathered during leg 3 were obtained using the University of Colorado DataHawk2 Unmanned Aircraft System. The Datahawk2 (DH2, developed by co-PI Lawrence) is a low-cost (~$1k) small-Unmanned Aircraft System (sUAS 1.1 m wingspan, 1 kg weight, 40-minute endurance) carrying various meteorological sensors. Instrumentation includes a fine wire sensor providing high frequency (800 Hz) information on temperature and wind speed, multiple sensors for temperature and relative humidity, and up- and downward looking thermopile sensors to provide infrared temperatures of the sky and surface. Measurements of airspeed, attitude, altitude, and ground speed provide high-frequency (10 Hz) 3D wind estimates. Combined, these sensors provide a comprehensive picture of atmospheric thermodynamic and dynamic state and provide context on the surface and sky condition under which these measurements were obtained. Together this sensor suite allows for estimation of turbulent energy exchange between the surface and overlying atmosphere. Data products will provide estimates of sensible heat flux, (bulk and eddy co-variance techniques) and latent heat flux (bulk method).

During leg 3, various flight patterns were followed to collect these boundary layer atmospheric data, depending on the atmospheric conditions or surface features being sampled. These included:

1. Profile – For profiling flights, the DH2 was flown between 30m and 1000m altitude, or up to cloud base (if lower than 1000m). These flights were conducted regularly to measure the atmospheric conditions throughout the lower atmosphere, and its evolution.
2. Loiter – For loiter flights, the DH2 was flown at a constant altitude for several minutes. Loiter altitudes were chosen by looking at the data from a previous profiling flight and determining interesting layers, such as the top of an inversion.

Loiters just below cloud base, when clouds were too thick and moist to fly in, were also conducted.

3. Racetrack – The racetrack pattern was used to sample leads, by flying the plane back and forth from upwind to downwind of a lead, crossing over the lead at incrementally increasing altitudes, starting as low as 15m, and going up to 250m. Then, a full profile up to 250m was flown on either side of the lead.

During leg 3, a total of 47 DH2 science flights were completed, totalling 17 hours of flight time. Of these flights, 33 were pure profiling flights, 6 were profile/loiter flights, and 8 were racetrack/profile flights to sample leads.

Preliminary (expected) results

Figure 3.8.1 shows the temperature profiles from 44 out of the 47 science flights completed in leg 3. Data from 3 flights are missing, due to problems processing the data for these flights. This plot includes profiles up to 1000m, as well as profiles to lower altitudes when the cloud base was below 1000m, or when the flight was dedicated to lead sampling. Observed near-surface temperatures range from around -31.8°C to -6.3°C, with temperatures aloft ranging from -25.0°C to -7.7°C. A variety of boundary layer types have been observed: both strong and weak shallow surface inversions, strong elevated inversions, and well-mixed boundary layers.

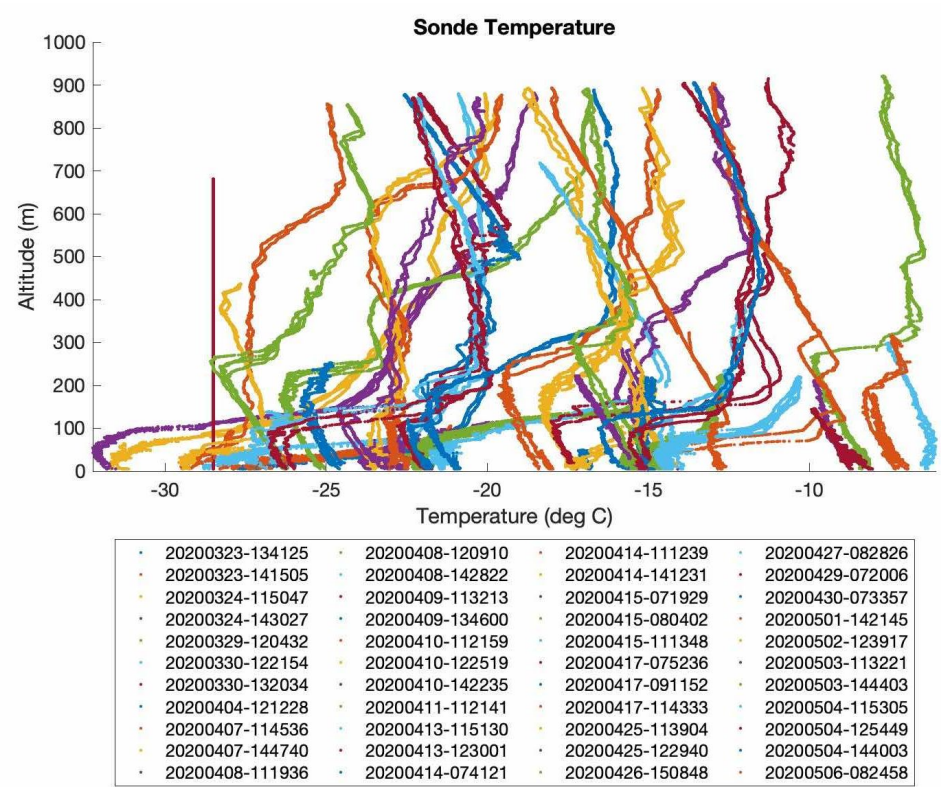

***Fig. 3.8.1**: Temperature profiles collected by Vaisala RSS-421 PTH sensor, from all flights during leg 3. Data from 3 flights are not plotted, due to processing issues.*

Figure 3.8.2 shows the (left) temperature and (right) meridional wind profiles of the same 44 flights, by date. This shows the evolution of warming temperatures both near the surface and aloft throughout the span of leg 3. This warming was associated with both the seasonal progression from winter to spring as well as more frequent southerly winds after mid-April.

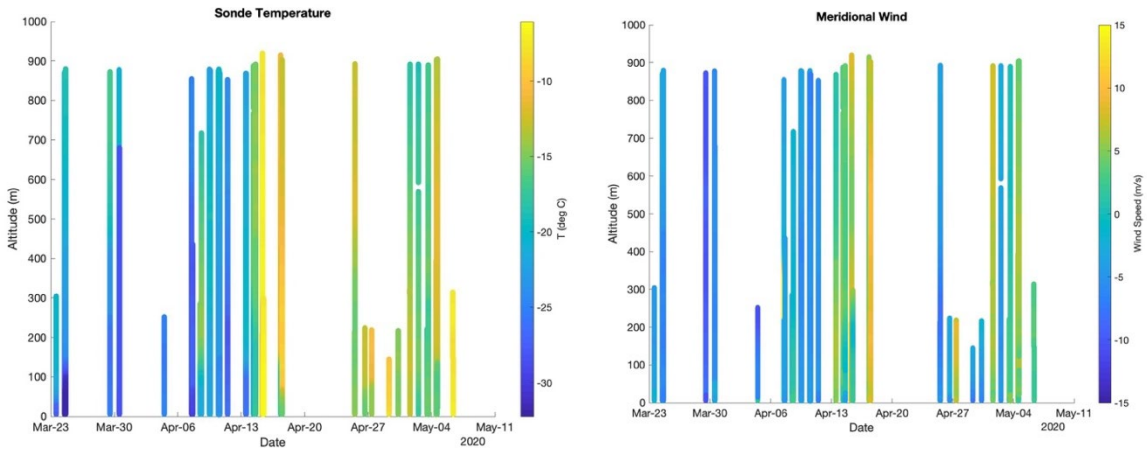

Fig. 3.8.2: *(a) Temperature profiles, by date, collected by Vaisala RSS-421 sensor, from all flights during leg 3. (b) Meridional wind profiles from all flights during leg 3. Data from 3 flights are not plotted, due to processing issues.*

Figure 3.8.3 (left) shows the temperature and total wind speed profiles from 24-Mar at 14:43 UTC. This is an example of a classic wintertime Arctic boundary layer structure, with a shallow well-mixed layer close to the surface, capped by a strong inversion. A pronounced low-level jet is located at the top of the inversion. Figure 3.8.3 (right) shows the temperature and total wind speed profiles from 15-Apr at 08:13 UTC. This is an example of a classic spring or summer Arctic boundary layer structure. In this case the well-mixed boundary layer is deeper, reflecting the reduced stability of the atmosphere at this time of the year.

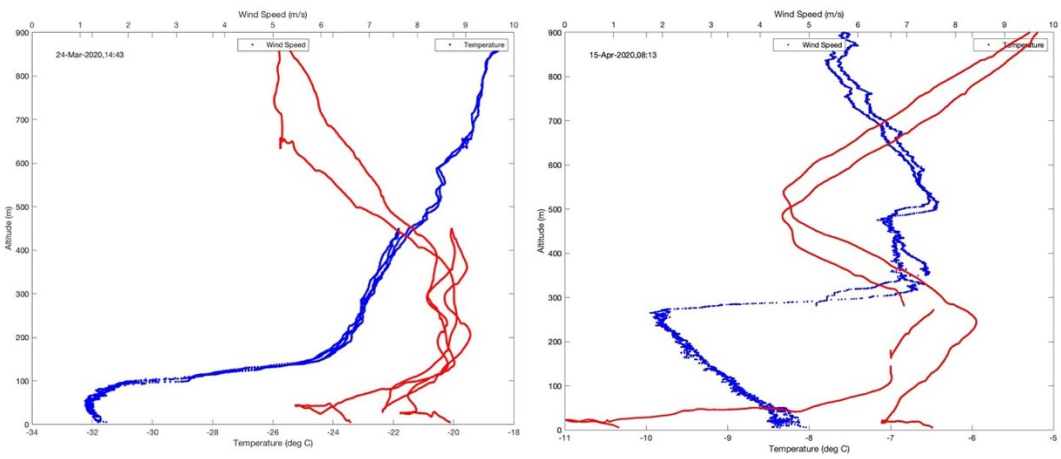

Fig. 3.8.3: *(a) Temperature and wind profiles from 24-Mar, showing a classic wintertime Arctic boundary layer structure. (b) Temperature and wind profiles from 15-Apr, showing a classic spring or summertime Arctic boundary layer structure.*

The data gathered during the lead sampling flights will show how boundary layer state and turbulent fluxes vary upwind and downwind of a lead, as well as above the lead at varying altitudes. Figure 3.8.4 shows surface IR temperature from a lead sampling flight on 29-Apr. The warmer colours show where the aircraft was flying over the lead, and the circles on either side show the location of the upwind and downwind profiles. The location of the circles was shifted throughout the flight to account for ice drift.

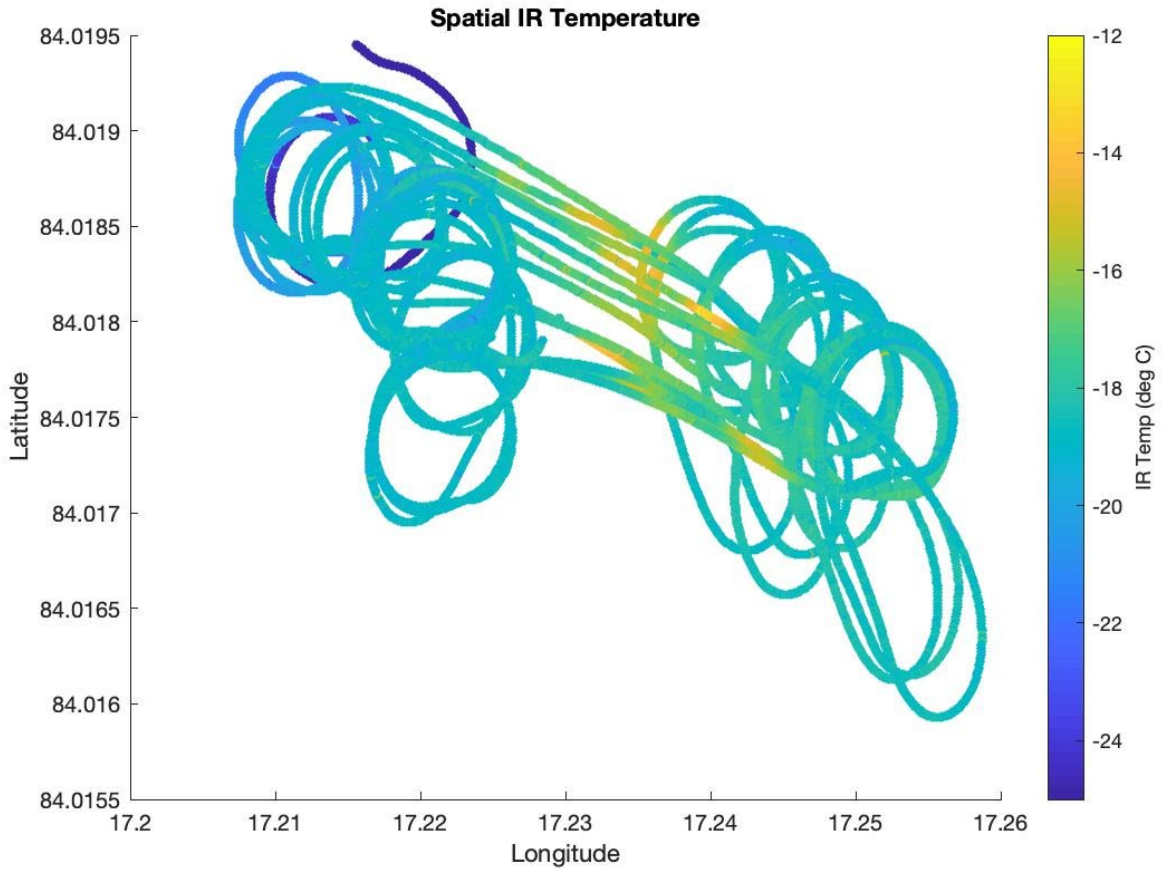

***Fig. 3.8.4**: Surface IR temperature mapped by the DH2 during a lead sampling flight on 29-Apr.*

These observed boundary layer profile structures and turbulent fluxes, over both sea ice and lead environments, will be used to evaluate atmospheric reanalyses and regional weather and climate models. Specifically, much of this work will focus on the Regional Arctic System Model (RASM), which is a limited-area, coupled ice-ocean-atmosphere-land model. Additionally, idealized one- and two- dimensional simulations, with the atmospheric component of RASM, the Weather Research and Forecasting (WRF) model, will be used for sensitivity experiments aimed at improving boundary layer parameterizations in the model.

Data management

All data are handled, documented, archived and published following the MOSAiC data policy (see APPENDIX). Preliminary processed B1 datafiles and quicklooks are available on the MCS. Final data will be stored at the Arctic Data Centre following additional quality control in accordance with the agreement between ADC and the MOSAiC Project lead. DOIs will be communicated to PANGAEA for later access via the future MOSAiC Data Portal. It is expected that data papers will be prepared and submitted to Earth System Science Data documenting these datasets.

References

None

3.9 Wind and Turbulence Structure in the Atmospheric Boundary Layer

Andreas Preußer[1], Ian Brooks[2] [31]DE.UNITRIER
[32]UK.UNI-LEEDS

(not on board) Ryan Neely III[2], Barbara Brooks[2],
Günther Heinemann[1]

Objectives

In order to better understand the new Arctic and its future development, improved numerical models and new verification data are needed particularly for the atmospheric boundary layer (ABL). The measurements will provide wind profiles with high spatial and temporal resolutions. In addition, Doppler wind lidar measurements allow for the determination of the turbulence structure of the ABL. A one-year long data set of wind and turbulence profiles will be generated for the verification of numerical models in the Arctic.

Overarching, the goal is to develop an enhanced understanding of the physical processes governing atmospheric boundary layer structure, turbulent mixing, and the interactions with both the surface and clouds in the central Arctic. This includes the following specific objectives:

- Characterize the turbulent dynamics of the Arctic atmospheric boundary layer and the physical processes controlling it over a full annual cycle. BL mixing directly affects the surface heat flux and both influences cloud properties and is influenced by in-cloud processes, and thus impacts the radiative fluxes and surface energy budget, contributing to ice formation/melt.
- Determine the interactions of Arctic boundary layer structure with the surface turbulent fluxes of momentum and heat. Surface fluxes are a controlling influence on lower BL structure. Elevated sources of turbulence, e.g. wind speed jets and radiative cooling at cloud top, dominate the control of upper BL structure and can impact surface fluxes where surface forcing of turbulence is weak, and thus the surface energy budget and ice evolution.
- Identify and describe the significant processes controlling coupling/decoupling of BL clouds to the surface. Decoupling isolates BL cloud from surface sources of moisture and aerosol; this may affect cloud properties (iii) and thus the surface radiation budget.

Work at sea

The boundary-layer dynamics measurements were obtained via active remote sensing instruments, which included three slightly different Doppler lidars and a phased array Doppler sodar. The University of Trier group supplied a Halo-Photonics Streamline (HPS) scanning wind lidar (Figure 3.9.1), which operates at a wavelength of 1.5 µm and is eye-safe. It was installed on board Polarstern on the lower P-deck in September 2019, alongside with a Galion G4000 wind-profiling lidar from the University of Leeds group. A nearly identical second HPS model was additionally provided by the Leeds group for operation on the pack ice along with their Scintec MFAS Sodar (Figure 3.9.2).

The measurement-principle of the lidars relies on reflected light from particles in the atmosphere (aerosols, cloud droplets, and ice crystals). While the Halo lidars provide measurements of backscatter intensity and along-beam Doppler velocity, the Galion lidar solely provides Doppler velocity as an output. The two Halo lidars can in theory operate with a maximum range of up to 10 km. However, previous campaigns have shown that the range is restricted by the low aerosol concentration in the Arctic and Antarctic, which can partly be compensated by increasing the averaging interval and adjusting the beam focus in order to optimize the signal-to-noise ratio (SNR), as recommended by Hirsikko et al. (2014). All used lidars are programmable scanning devices, which enable vertical scans in all hemispheric directions.

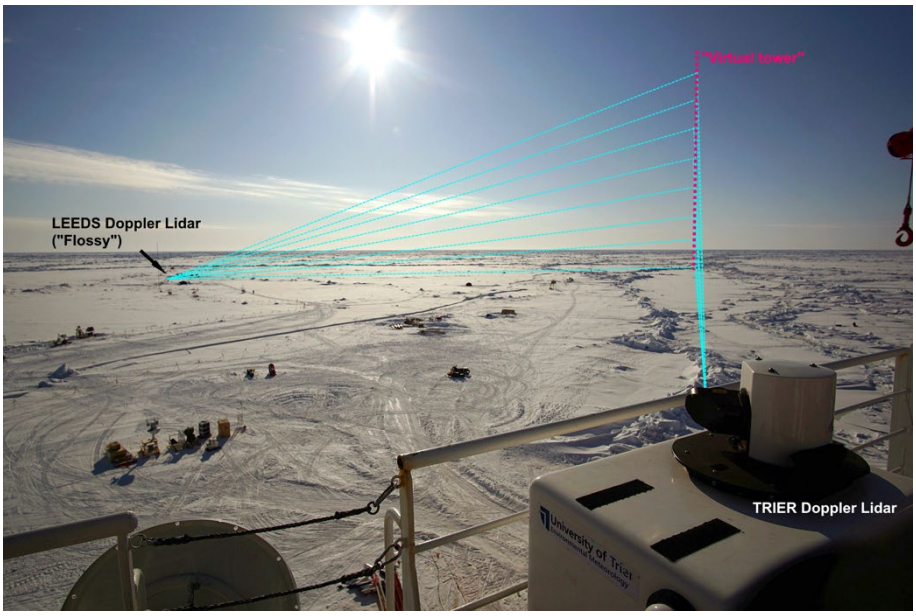

Fig. 3.9.1*: Principle of the Dual-Lidar setup of the Trier and Leeds Halo systems. One of the intersection points was approximately positioned over the lead east of the former ROV city tent (Photo: Andreas Preußer).*

For the Halo lidars, the main scan patterns that were used since Leg 1 include the range-height indicator (RHI), the vertical azimuth display (VAD) and vertical stares. RHI scans were performed with different elevation angles up to 50°. This allows for measurements of cross-sections, but also for vertical profiles of horizontal wind variances (TKE estimation, Banta et al. 2006). Vertical STARE data can be used to compute the vertical wind variance profile (see Päschke et al., 2015). The VAD scans are used for the determination of wind profiles above the lidar with multiple evenly spaced scans at an elevation-angle of 75° (e.g., Zentek et al., 2018). As for the Galion lidar, VAD scans with elevation-angles of 30° and 50° are continuously performed since the start of Leg 1.

For most of Leg 1 and 2 as well as the start of Leg 3, the Halo lidars were configured to operate independent from each other following the above described scan modes. However, despite the quite dynamic ice situation on Leg 3 it was again possible in late April to configure them to a synchronized mode, in which measurements of the same volume of air from two different directions ('virtual-tower'; see Figure 1) could be performed for 12 days in total. This does now allow for the air motion to be resolved in two dimensions at three defined locations across the floe. At the same time, the virtual-tower concept provides two intersecting RHI scans. In order to calculate the scan configurations for each lidar that are required for the synchronized measurements, accurate relative positions and orientations of the two instruments were regularly acquired. Unfortunately, frequent movement of the ice during Leg 3 made it difficult to initialize fixed scan parameters for the synchronized scans. As major improvements in that regard cannot be expected during Spring and Summer, the Halo lidars are now switched back to operate independently for the remaining two Legs, where no one from Leeds or Trier will be on board.

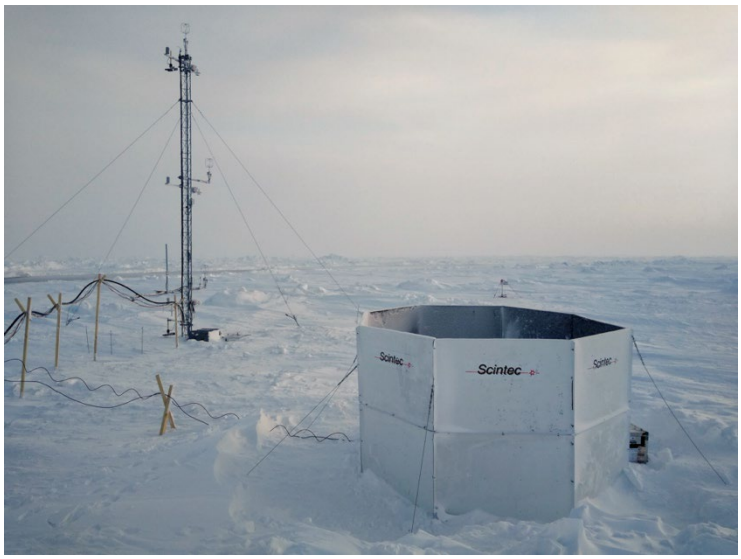

Fig. 3.9.2*: New location of the Scintec MFAS sodar at Met City, after the former location had to be abandoned due to a nearby developing ridge (Photo: Andreas Preußer).*

The sodar uses acoustic backscatter to make its measurement. A sequence of audible acoustic pulses is transmitted. Echoes are returned from density gradients in the atmosphere – these arise primarily at gradients in temperature, either large scale gradients such as temperature inversions, or small-scale gradients resulting from turbulence. The intensity of the acoustic backscatter provides some information on the turbulent and thermodynamic structure of the lower atmosphere. The Doppler shift of the echo provides a measurement of air motion. The acoustic beam can be steered off the vertical, allowing measurements of horizontal wind components to be made giving another measurement of the wind profile. The sodar vertical resolution is 10m, with a range from 40-1000m (though the upper limit is strongly dependent upon conditions and rarely reaches this absolute maximum). Wind profiles are obtained at 10-minute intervals and vertical backscatter profiles every 5 minutes.

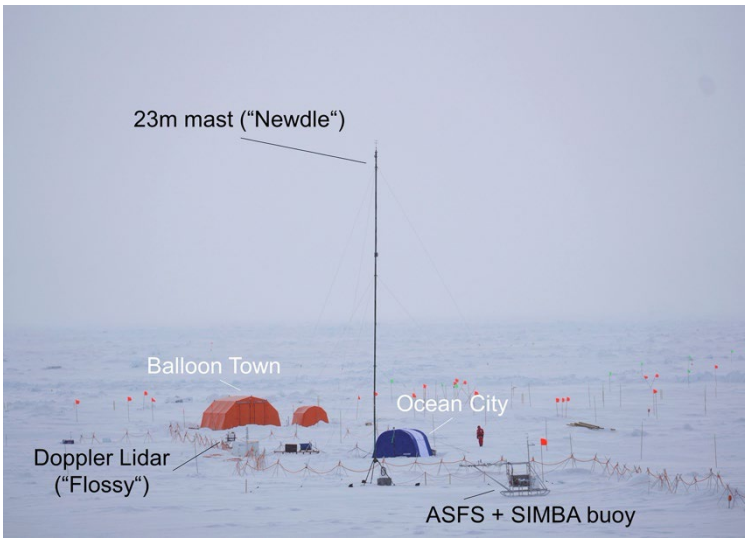

Fig. 3.9.3*: New setup of atmospheric measurements in the Central Observatory, nearby Balloon Town and Ocean City (11 April 2020 - Photo: Andreas Preußer).*

Due to close-by lead openings and subsequent ridging, both the Leeds Halo and the sodar had to be relocated in the course of Leg 3. While the Sodar could be reinstalled quite close to

its former location at *Met City* (no issues with generator-based power supply; compare Figure 2), the Leeds Halo had to be moved to a new location nearby *Ocean City* and *Balloon Town* (steady power line connection; compare Figure 3.9.3). Both operations caused some unfortunate but unavoidable gaps in the March data records. Ultimately, all instruments on the pack ice had to be disassembled and taken on board before departing from the MOSAiC floe with Polarstern on May 16.

Preliminary (expected) results

Figure 3.9.4 shows an exemplary one-week long timeseries of wind speed and direction, calculated from VAD scans (16-22 April 2020) of the Trier Halo lidar installed on board Polarstern (P-Deck, Starboard side). It illustrates several characteristic features for the Leg 3 period, such as the increased frequency of strong wind-events in April, sudden shifts in primary wind-directions (northerlies to southerlies) as well as some clear-sky periods as being the main cause for low vertical coverage. Interestingly, the early morning of April 29 shows a vertically non-uniform wind-direction change, indicating vertical shearing.

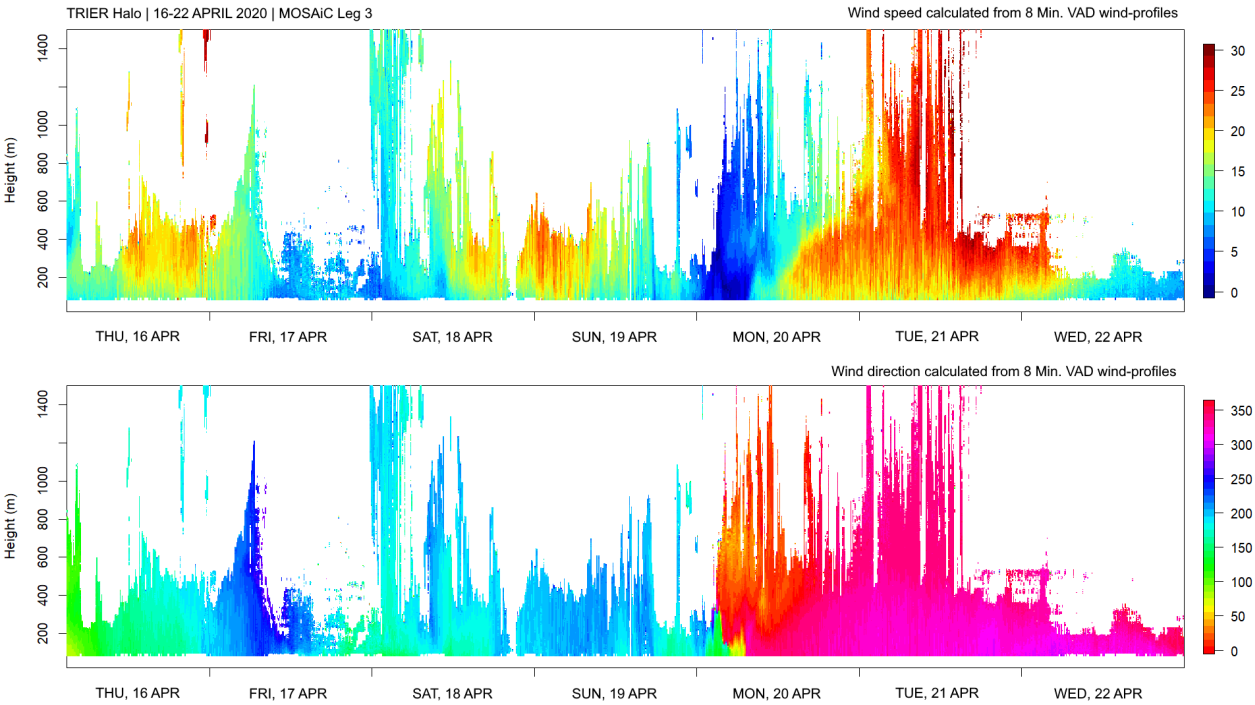

***Fig. 3.9.4**: Timeseries of wind speed and wind direction, as derived from VAD-6 from the Trier Halo between 16-22 April 2020.*

A similar shorter timeseries is shown in Figure 3.9.5, now for the period from 11-14 May 2020. This was the time of a major storm event which caused significant fracturing of the *MOSAiC floe* and inherently the *Central Observatory*. A strong jet exceeding 30 m/s can be seen on the first half of May 13 at approximately 300-600 m height, which is presumably related to a short period of more northerly wind directions and increasingly steep pressure gradients.

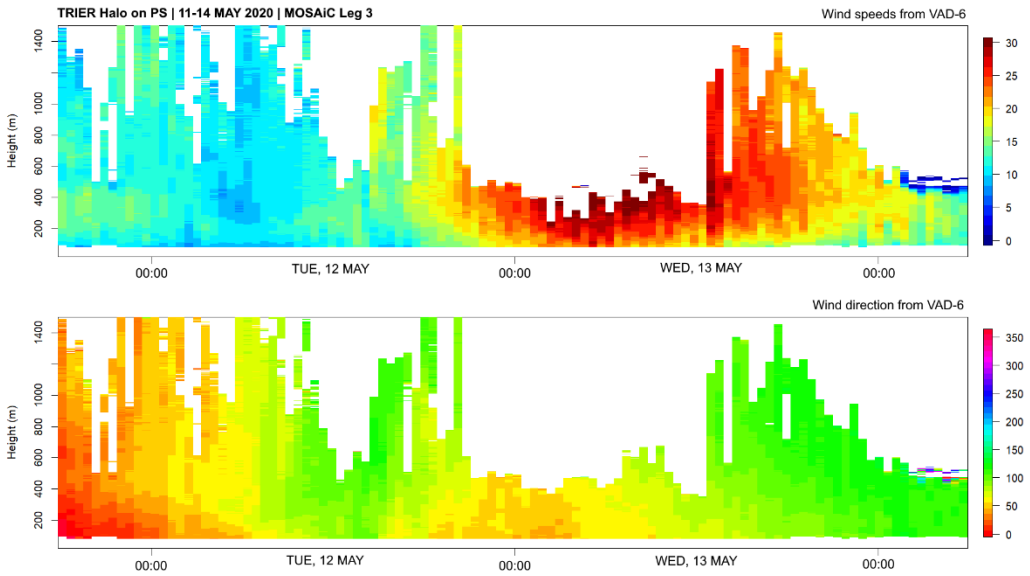

***Fig. 3.9.5**: Timeseries of wind speed and wind direction, as derived from VAD-6 from the Trier Halo between 11-14 May 2020 – the period in which the MOSAiC floe was severely broken in pieces.*

As a first insight into the synchronized RHI scans from both Halo Lidars (on board Polarstern & near *Ocean City*), an example-set from the 05 May 2020 (09:55 UTC) can be seen in Figure 3.9.6 (upper two panels), together with horizontal velocity variances for 20m height-bins (lower panel). The two range-height cross-sections show quite good agreement as the targeted intersection of laser-beams (virtual tower) was located on the line-of-sight axis of both instruments, heading towards *Balloon Town*. Velocity variances agree well at heights exceeding 400m altitude.

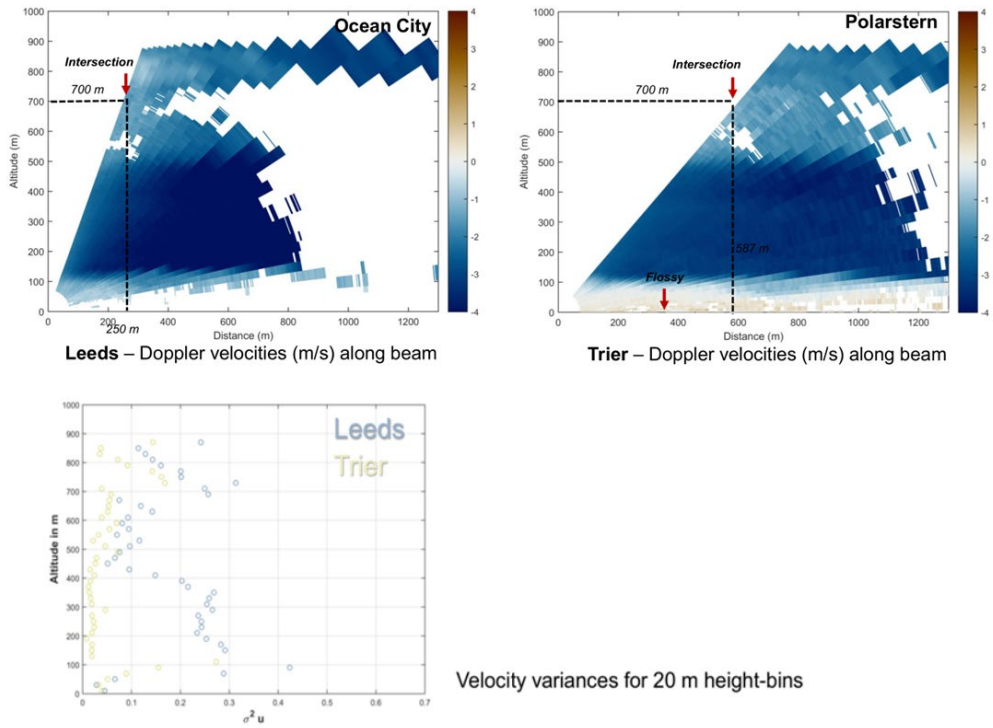

***Fig. 3.9.6**: Upper two panels: Doppler velocities from both Halo systems, scanned in RHI mode towards Balloon Town (05 May 2020, 09:55 UTC). Lower panel: Velocity variances from the former two RHI scans, separated into 20m height-bins.*

Data management

All data are handled, documented, archived and published following the MOSAiC data policy (see APPENDIX). Raw data is archived daily on the MOSAiC central Storage (MCS) system, on a RAID belonging to Leeds and two external hard-drives. All data will be made available through the central MOSAiC archive on the PANGAEA data repository (World Data Center PANGAEA Data Publisher for Earth & Environmental Science www.pangaea.de). Derived data products require post-cruise data processing and will be archived with PANGAEA as soon as they are available.

References

Banta, RM, Pichugina, YL, Brewer, WA. (2006) Turbulent Velocity-Variance Profiles in the Stable Boundary Layer Generated by a Nocturnal Low-Level Jet, Journal of the Atmospheric Sciences, 63, 2700-2719

Hirsikko A, O'Connor E, Komppula M, Korhonen K, Pfuller A, Giannakaki E, Wood CR, Bauer-Pfundstein M, Poikonen A, Karppinen T, Lonka H, Kurri M, Heinonen J, Moisseev D, Asmi E, Aaltonen V, Nordbo A, Rodriguez E, Lihavainen H, Laaksonen A, Lehtinen KEJ, Laurila T, Petäjä T, Kulmala M and Viisanen Y (2014) Observing wind, aerosol particles, clouds and precipitation: Finland's new ground-based remote-sensing network. Atmospheric Measurement Techniques, 7. pp. 1351-1375. ISSN 1867-8548 10.5194/amt-7-1351-2014.

Päschke E, Leinweber R, and Lehmann V (2015) An assessment of the performance of a 1.5 µm Doppler lidar for operational vertical wind profiling based on a 1-year trial, Atmospheric Measurement Techniques, 8, 2251-2266, https://doi.org/10.5194/amt-8-2251-2015.

Zentek R, Kohnemann S, and Heinemann G (2018) Analysis of the performance of a ship-borne scanning wind lidar in the Arctic and Antarctic. Atmospheric Measurement Techniques, 11, 5781-5795, https://doi.org/10.5194/amt-11-5781-2018.